

Relationships between the physical properties of Triassic sandstones in the West Netherlands Basin and short-wave infrared reflectance spectroscopy

Mathijn G.H. Brouwer

Student number: 6034608

Utrecht University, The Netherlands

April 2022

First supervisor:

Dr. Suzanne J.T. Hangx

Second supervisor:

Dr. A.R. Niemeijer

Supervisor TNO:

J.C. Stam

Advisor ITC:

Dr. F.J.A. van Ruitenbeek

Advisor ITC:

Dr. C.A. Hecker



**Utrecht
University**



Abstract

Short-Wave Infrared Reflectance (SWIR) spectroscopy is a powerful and effective tool for identifying phyllosilicates, carbonates and other mineral groups. Hyperspectral imaging allows for quick, consistent and spatially continuous data analysis. This study investigates whether correlations between the hyperspectral data from short-wave infrared spectroscopy and the physical rock parameters, such as porosity, permeability and mineralogical composition, can be established. Hyperspectral image acquisition was performed from two cored intervals of Triassic sandstones in the West Netherlands Basin, the Naaldwijk-Geothermal (NLW-GT-01) and the Barendrecht-Ziedewij (BRTZ-01) borehole. The slabbed cores were specifically chosen due to their similar lithology yet significant difference in porosity and permeability values.

For each pixel (256 μm), the wavelength positions and depths of the three deepest absorption features in specified wavelength intervals were calculated. Calculations were generated with Hyperspectral Python software (HypPy3) and the wavelength mapping technique described by Van Ruitenbeek et al. (2014). These wavelength maps and other hyperspectral parameters that served as proxies were used for spectral algorithms to classify the pixels.

The results provided semi-quantitative mineral abundancy maps, detected compositional variation between equivalent minerals and successfully distinguished phyllosilicates, which other methods would not have been able to. However, non-hydroxylated minerals (e.g. silica, feldspar) are non-responsive within the SWIR region of the electromagnetic spectrum. The results advocate that the cored interval of the NLW-GT-01 was extracted from a higher metamorphic intensity zone and was subjected to more significant amounts of carbonate cementation than the BRTZ-01 core, both being mechanisms for porosity loss. The findings in this research are in accord with other studies that have examined the regional geology and/or these boreholes (e.g. De Hoo 2021; Maniar 2019; Ursem 2018; Koenen et al. 2013). Therefore this research concludes that SWIR spectroscopy is of added value to the current standard of core logging. However, the current methodology could not produce quantifiable parameters that correlate correctly with physical parameters. Future research should 1) produce larger hyperspectral datasets which could be directly linked to known physical properties, 2) investigate using a combination of multiple regions within the electromagnetic spectrum, and 3) the usability of this technique on core cuttings.

Keywords: Short-Wave Infrared Reflectance (SWIR), spectroscopy, hyperspectral imaging, core logging

Contents

1	Introduction	5
1.1	Introduction: Dutch Hydrothermal Systems	6
1.2	Introduction: short-wave infrared spectrometry	7
1.3	Present aim	8
2	Background	10
2.1	Regional Geology	10
2.1.1	Palaeozoic, creation of the Southern Permian Basin	11
2.1.2	Early-Middle Triassic, subsidence and the formation of the West Netherlands Basin	12
2.1.3	Late Jurassic – Early Cretaceous, rifting and subsidence	12
2.1.4	Late Cretaceous – Paleogene, inversion	13
2.2	Theoretical background of SWIR spectroscopy	13
2.2.1	Spectral responses	13
2.2.2	Aluminium phyllosilicates	14
2.2.3	Fe-Mg phyllosilicates	15
2.2.4	Carbonates	15
2.2.5	Silicates	15
2.2.6	Sulphates	15
2.3	Importance of diagenetic processes/mineral assemblages	15
2.3.1	Near-surface diagenesis	15
2.3.2	Low depth burial	16
2.3.3	Intermediate depth burial	17
2.3.4	Deep burial	17
2.4	SWIR spectroscopy versus other methods	18
2.4.1	Petrographic analysis of thin sections	18
2.4.2	X-ray diffraction (XRD)	18
2.4.3	SWIR spectroscopy	18
3	Dataset and methodology	19
3.1	Materials and dataset	20
3.1.1	Samples	20
3.1.2	Available data	21
3.1.3	NLW-GT-01	21
3.1.4	BRTZ-01	22
3.2.1	Instruments	25
3.2.2	Image acquisition	25
3.2.3	Pre-processing	26

3.3	Image processing	27
3.3.1	Spectral analysis.....	27
3.3.2	Wavelength position mapping.....	27
3.3.3	Albedo	28
3.3.4	Ferrous drop.....	29
3.3.5	Illite crystallinity	29
3.3.6	Illite over Kaolinite	30
3.3.7	Position and depth of absorption features.....	30
3.3.8	Mixture ratio	31
3.3.9	Shannon entropy.....	31
3.3.10	Decision trees.....	32
4	Results	33
4.1.1	Wavelength mapping.....	33
4.1.2	Ferrous drop.....	35
4.1.3	Illite crystallinity	37
4.1.4	Illite over kaolinite	38
4.1.5	Position of 2200 nm feature	39
4.1.6	Strength of 1900 nm feature	41
4.1.7	Shannon Entropy.....	42
4.1.7	Hyperspectral parameters – core overview.....	44
4.1.8	Decision trees - mineralogy	44
4.1.9	Decision trees – core overview	48
5	Discussion.....	52
5.1	Data accusation.....	52
5.2	Hyperspectral parameters	52
5.3	Data comparison	54
5.4	Limitations.....	56
5.5	Recommendations	57
6	Conclusion.....	58
	Bibliography	59
	Appendix:	64
1	Sample LIST:	64
2	Subset Script	66
3	Decision trees.....	67
4	Data overview	71

1 Introduction

As the world demands the transition from fossil fuels to more zero-carbon energy sources, the call for sustainable energy increases. Geothermal energy is a sustainable energy source that exploits the thermal energy stored in the Earth's body. In the Netherlands, approximately 20 doublet systems are being used to extract the subsurface heat. The master plan for geothermal energy in the Netherlands states the ambition to realise up to 700 doublets systems before 2050 (Stichting Platform Geothermie 2018). A doublet operates using two wells, the producer well retrieves warm water from the subsurface, and the injector well pumps back the produced water once its heat has been extracted, see Figure 1. These wells may have a distance of up to 1500 meters between them at depth. At the surface, the two wells are linked via a heat exchanger, which captures the geothermal heat from the primary loop and transfers it to a secondary loop (Mijnlieff 2020).

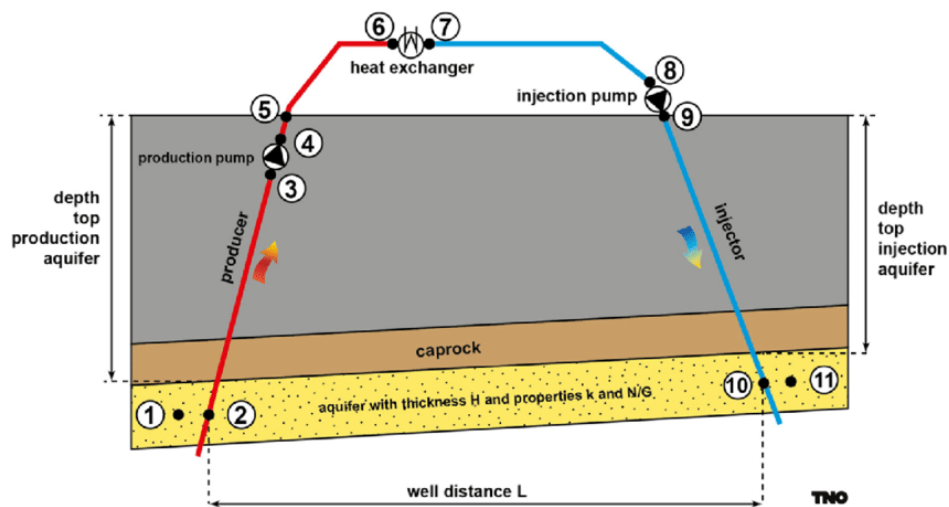


Figure 1: Schematic of a doublet geothermal system (Mijnlieff 2020). 1 and 11. the aquifer and geothermal source; 2. mid-aquifer in the production well; 3. inlet production pump; 4. outlet production pump; 5. top production well; 6. inlet heat exchanger; 7. outlet heat exchanger; 8. inlet injection pump; 9. outlet injection pump; 10. mid-aquifer in the injection well. Abbreviations: H, thickness; k, permeability; N/G, net to gross.

Due to local differences in the geologic characteristics, there is a wide range of geothermal play types (Moeck, 2014). The six types that Moeck categorises are (1) Volcanic, (2) Plutonic, (3) Extensional domain, (4) Intracratonic basin, (5) Organic belt and (6) Basement type. The first three are convection dominated the others are conduction dominated. Countries like Iceland, the United States, and Italy can exploit volcanic and plutonic types of geothermal plays. These are suitable for high-temperature systems for both heat production and electricity generation. The approximately twenty Dutch geothermal systems all have sedimentary rocks as reservoirs. These geothermal types yield lower temperature ranges and are currently used for direct use of the heat, such as heating greenhouses, residential/office buildings and swimming pools. Over the last decade, geothermal energy development has increased significantly and was responsible for cumulative annual energy production of 6.20 PJ (1 PJ = 10^{15} Joule) in 2020. This is equivalent to the average annual energy consumption of 250,000 people in the Netherlands (Ministry of Economic Affairs and Climate Policy 2020).

Kramers et al. (2012) estimated a nationwide Heat In Place (HIP) of 820,000 PJ within the Dutch subsurface. Considering the techno-economic performance evaluations, this suggests a total recoverable heat of 85,000 PJ. As extraction techniques and strategies improve, a geothermal project's economics and total recoverable heat do. Other factors, such as the ambitions to reduce the CO₂ output set by the Paris climate agreement (Delbeke et al. 2019) and hydrocarbons' high and volatile

prices, have provided extra initiatives for geothermal systems. This trend is reflected by the increase in licenses for geothermal energy production and exploration licences, as shown in Figure 2.

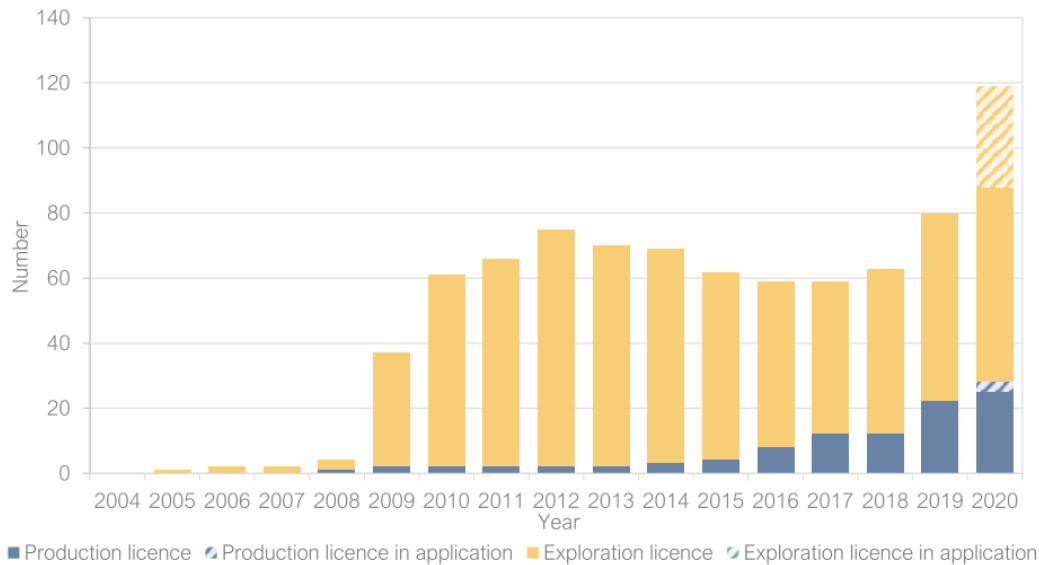


Figure 2: Active number of licenses for geothermal energy per year. For 2020, the number of applications is also presented (Ministry of Economic Affairs and Climate Policy 2020).

1.1 Introduction: Dutch Hydrothermal Systems

To effectively use subsurface heat, the aquifer should meet the following requirements: Firstly, the aquifer should contain a large quantity of water. The volume of water in the aquifer is determined by the thickness and size of the aquifer and its porosity. Secondly, the water must be able to flow through the reservoir. The ease of flow is expressed by its permeability; this is the ability of a material to transmit fluid (or gasses) and is dependent on the interconnectivity of the pores or fractures. Thirdly, the temperature of the aquifer needs to be high enough to extract heat. The Dutch subsurface has an average temperature gradient of 31.3 °C/km (Bonté et al. 2012). However, this varies per region due to the geological setting. Lastly, it is essential to maintain proper flow of fluids over time. Therefore, the number of natural barriers (e.g. faults, impermeable layers) should be low, and the possible effect of producing heat on the surroundings should be known.

Geothermal heat can be distributed by two mechanisms: (1) heat conduction through the rocks and (2) by a moving fluid such as groundwater, known as advection. Fourier’s law can describe conductive heat flow:

$$q = -\lambda \Delta \tag{1}$$

In which the heat flux density [Watt per unit area] is caused by the material’s thermal conductivity (λ) [$\text{J s}^{-1} \text{m}^{-1} \text{K}^{-1}$] and the temperature gradient (ΔT) [K m^{-1}] between parts of a geologic system. Thermal conductivity (λ) represents the ability of a material to transport heat. This varies between different types of rock. Due to alterations and different degrees of compaction, the thermal conductivity can vary within each rock type (Clauser et al. 2013). Other factors such as rock layering, foliation or other structures may also affect the thermal conductivity. This can inhibit thermal heat distribution (Bucher et al. 2021).

The amount of heat stored in a particular rock is expressed by its heat capacity (C). Heat capacity is defined as the sum of the change in the amount of heat (thermal energy) that is expressed as ΔQ [Joules] over a temperature range (ΔT) [Kelvin]:

$$C = \frac{\Delta Q}{\Delta T} \quad (2)$$

The porosity of a rock is the fraction of space between the solid particles; this includes pores, cracks, inter-and intra-crystalline spaces. Porosity is given as a number between 0-1 or a percentage between 0-100% and indicated by the symbol Φ . These voids contain the liquid fluids or gasses that are crucial for the mechanism of advection. Different methods are available for determining the porosity of rocks, of which helium-pycnometry and mercury-porosimetry are the most common. It should be noted that other methods can yield different porosity values and that the porosity does not give any information concerning pores sizes, their distribution or their connectivity.

The permeability of a rock indicates the ability of fluids/gas to flow through the porous media. The SI unit of permeability is m^2 . However, the darcy unit [d] ($1 \text{ darcy} = 9.869233 \cdot 10^{-13} m^2$) is of more practical use. There are three main types of measurements to determine permeability: steady-state flow-through techniques, transient step methods and pressure oscillation methods. These last two are needed when the permeability of a sample is low.

The performance of a hydrothermal doublet system within a sedimentary basin can be estimated through the power that can be extracted by a hydrothermal system and is expressed in Watt [W or JS^{-1}]:

$$E = Q \Delta T C_p \quad (3)$$

The power (E) is dependent on the flow rate (Q) in cubic meters per second, the temperature difference between the production temperature and the injected water temperature (ΔT), and the specific heat (C_p) of the fluid. The flow rate is the most difficult to predict within this estimate, with permeability and reservoir thickness as major uncertainty factors (Mijnlieff 2020).

1.2 Introduction: short-wave infrared spectrometry

Spectroscopy is the study of light as a function of wavelength that has been emitted, reflected or scattered from a solid, liquid or gas (Clark 1999). Light is made out of photons, elementary particles with wave-particle duality. Visible light is part of the electromagnetic spectrum, which is the full range of frequencies of electromagnetic radiation and their respective wavelengths (λ), frequency (Hz) and photon energies (eV). Other well-known classes of electromagnetic radiation are gamma rays, x-rays, ultraviolet, infrared, microwaves and radio waves. The following section will discuss the short-wave infrared spectroscopy of minerals. However, the principles apply to any material.

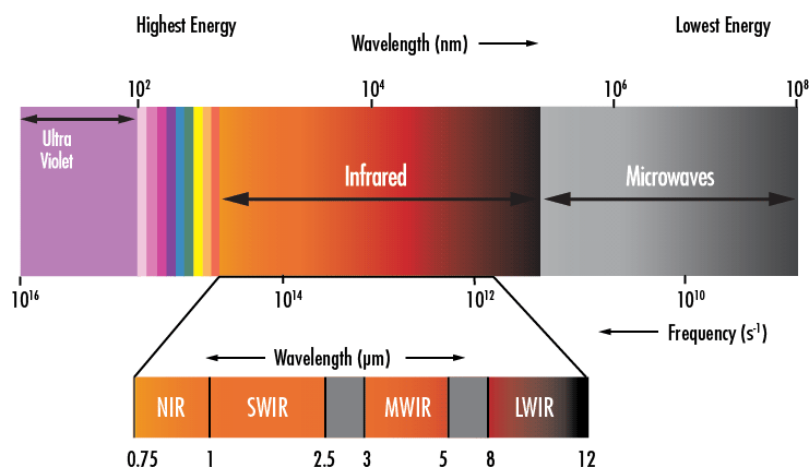


Figure 3: Electromagnetic spectrum illustrating the Ultra Violet, the Visible light, the Infrared and Microwaves wavelength ranges (from (Edmund Optics n.d.).

The infrared spectrum can be subdivided into near-infrared (NIR, 750-1000 nm), the short-wave infrared (SWIR, 1000-2500 nm), the mid-wave infrared (MWIR, 3000-5000 nm) and the long-wave infrared (LWIR, 8000-12000 nm), as illustrated in Figure 3. Within the SWIR electromagnetic spectrum, photons are modulated by molecular vibrations, rotations, bending and stretching of bonds. The detection of spectral responses within the SWIR spectrum is called SWIR reflectance spectroscopy. It is a valuable technique for mineral identification because many minerals have characteristic reflection patterns within this spectral range, see Figure 4. Mineral groups have characteristic spectra with diagnostic absorption features called spectral signatures. This signature varies in wavelength position, depth and/or shape as they are a function of mineral chemistry and structure (Chukanov et al. 2016). Using a specialised sensor and the spectral response of samples is measured in a ‘dark room’ with controlled lighting. Therefore it is possible to retrieve a consistent reflected signature of the samples.

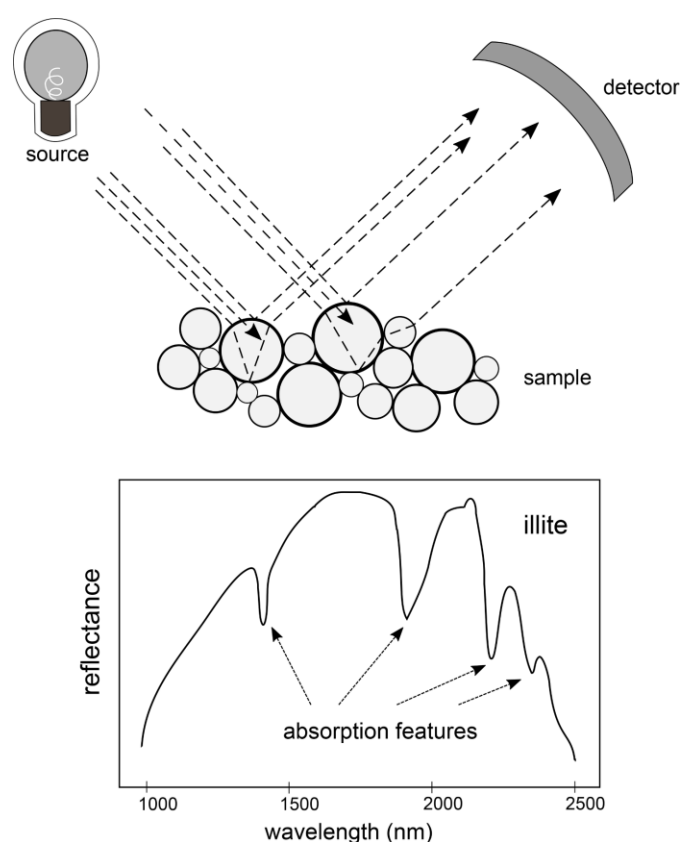


Figure 4: Principle of SWIR spectroscopy (Savitri et al. 2021) The sensor will detect all the reflected radiation. Light is reflected either directly at the sample surface or through multiple scattering. Specific wavelengths are absorbed by the material and form diagnostic absorption features in the infrared spectrum.

1.3 Present aim

TNO - Geological Survey of The Netherlands (TNO-GSN) stores data and physical samples of boreholes in the Netherlands (“NLOG” 2021). However, the physical properties of rocks (porosity, permeability and rock strength parameters) are often complicated, time-consuming and expensive to measure. Hyperspectral core imaging techniques are relatively fast and cheap. Moreover, they are non-destructive and can provide continuous information along with the available core. Hyperspectral core imaging systems like the SisuROCK can be equipped with multiple cameras simultaneously (RGB, VNIR, SWIR, LWIR), providing high spatial and spectral resolution with a scan rate of up to 30 sample crates an hour (Logger, n.d.; Specim 2014).

This MSc project aims to investigate whether correlations between the hyperspectral data from short-wave infrared spectroscopy and the physical rock parameters, such as porosity, permeability and mineralogical composition, can be established. As a case study, the Trias Westland geothermal borehole (NWL-GT-01, used for geothermal exploration) and the Barendrecht Ziedewij (BRTZ-01, an abandoned gas well) will be analysed. These two boreholes were selected because of their similarity in lithostratigraphy yet show marked differences in porosity and permeability. This project will systematically investigate any correlations between the earlier research that has determined physical properties such as porosity and permeability (De Hoo 2021; Maniar 2019; NLOG 2021) and the mineralogical information obtained via hyperspectral scanning of the cores within the SWIR spectral range. This technique can potentially be applied to other available core or cutting samples if a correlation can be established. This would provide valuable spatially continuous information about the properties of the Dutch subsurface that would be of interest to the geothermal industry. In summary, this research will answer the following research question:

Can relationships be determined between the physical properties of a rock and mineralogical data from hyperspectral mineral mapping?

Sub-research questions:

- Which minerals commonly occur in sedimentary drill cores and which can and cannot be identified using SWIR hyperspectral imaging?
- What are relevant proxies for the determination of physical rock properties? Explicit proxies that will be investigated include mineral abundance, clay content, quartz concentration and carbonate content.
- How can SWIR spectroscopy contribute to the current methods of reservoir characterisation.

Suppose strong correlations or proxies can be established between the already determined physical properties and the hyperspectral data. In that case, the standardisation of using hyperspectral core logging for core characterisation should be considered. If this technique provides indications yet no precise results on physical properties, it would still be helpful as a predictive technique to contribute to the current method of core logging.

2 Background

This chapter will present relevant information about (1) the geological features of the region from which the studied cores were obtained, (2) the theoretical background of SWIR spectroscopy, (3) the importance of diagenetic processes, (4) the added value and shortcomings of SWIR spectroscopy in comparison to other mineralogical analyses methods.

2.1 Regional Geology

For this study, cores from the Naaldwijk-Geothermie (NLW-GT-01) and the Barendrecht Ziedewij (BRTZ-01) boreholes will be used. These two boreholes were selected because of their similarity in lithostratigraphy yet show marked differences in porosity and permeability. Both boreholes are located within the mildly or not inverted parts of the West Netherlands Basin (WNB); see Figures 5 and 6.

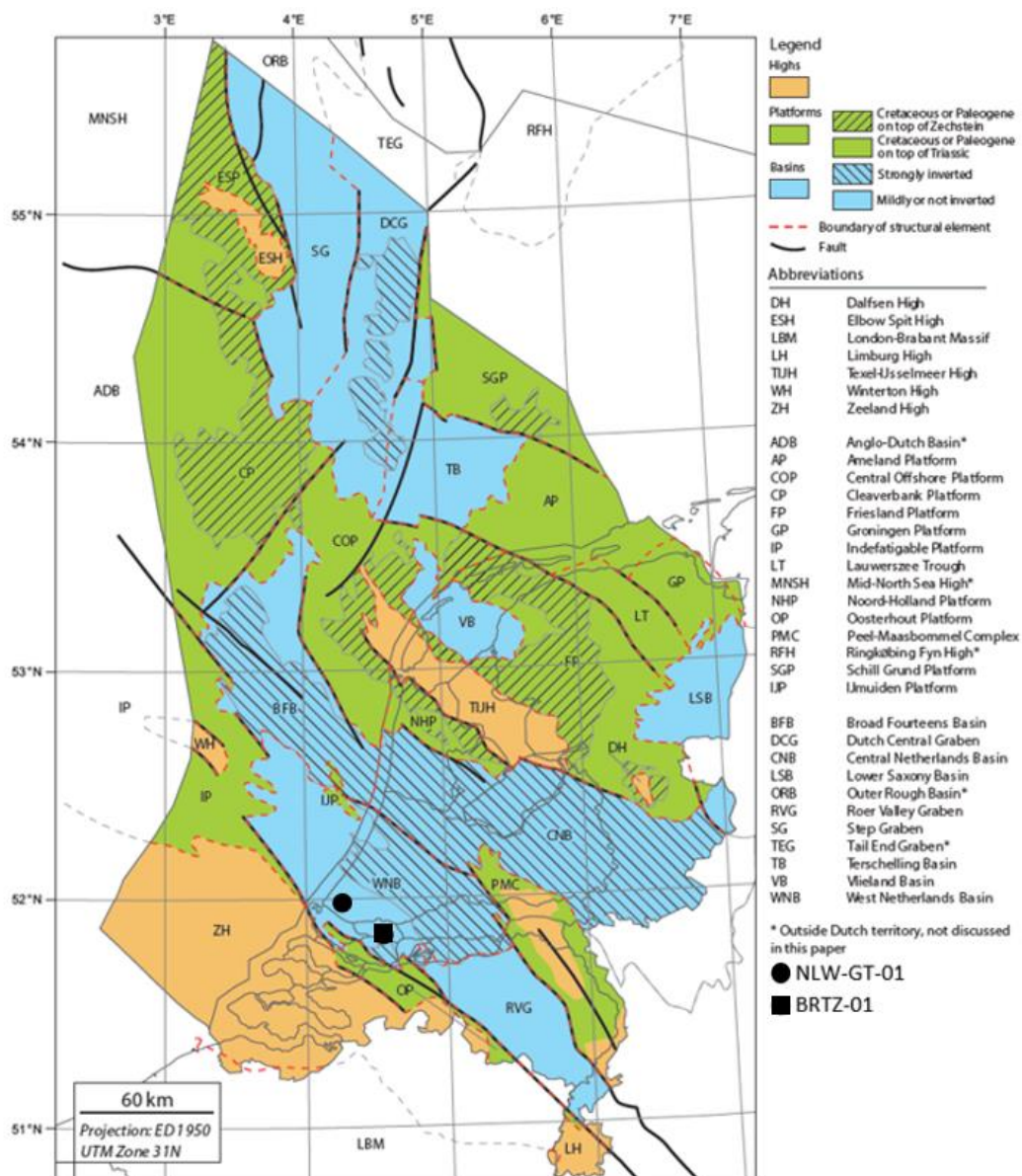


Figure 5: Late Jurassic - Early Cretaceous structural elements of the Netherlands (Kombrink et al. 2012), With the wells located within the mildly inverted parts of the WNB, NLW-GT-01 (left) and BRTZ-01 (right) indicated by the black dot and square.

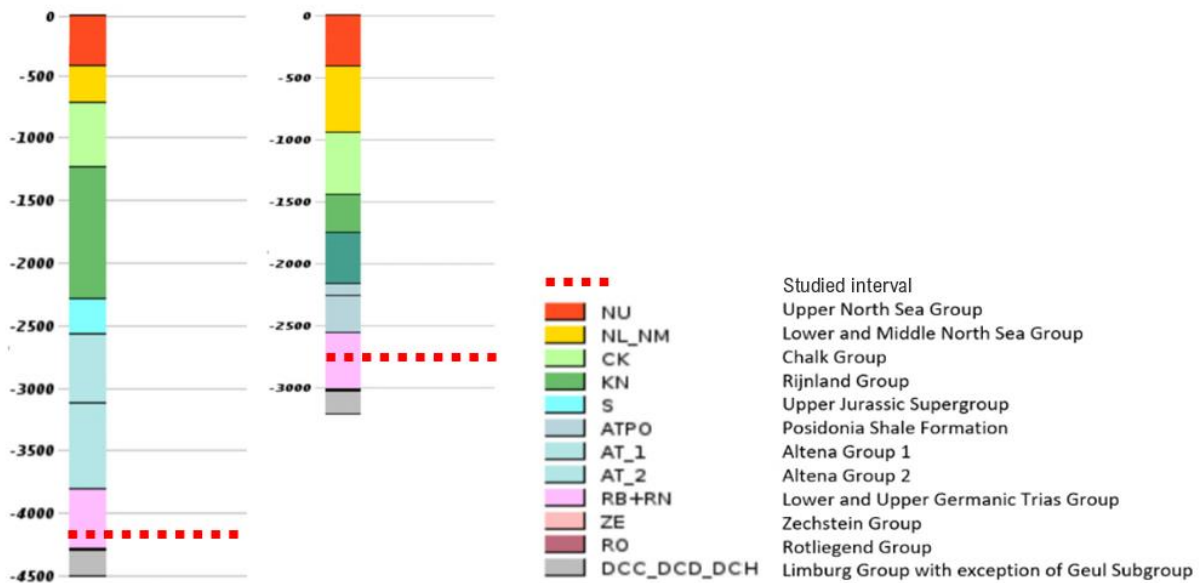


Figure 6: Stratigraphic log of NLW-GT-01 (left) and BRTZ-01 (right), depth profile in meters relative to NAP (TNO-GDN 2019).

The WNB is a northwest-southeast trending basin in the SW of the Netherlands. It extends westwards into the Dutch North Sea. The basin is approximately 130 km in length and 65 km in width; the onshore part is 80 km in length and 65 km in width. The London-Brabant High flanks the basin in the southwest and the Zandvoort Ridge in the northeast. Towards the southeast, the basin merges with the Roer Valley Graben. The cored samples lay within the Main Buntsandstein Subgroup. The northwest European Main Buntsandstein Subgroup is relatively constant in thickness and consists of the Hardegsen Formation, Detfurth Formation and Volpriehausen Formation. Yet, the Main Buntsandstein stratigraphy in the WNB is characterised by proximal sandstone equivalents of the Volpriehausen and Detfurth Claystone Members (Geluk 2005). The WNB underwent the following tectonic phases in chronological order (Van Balen et al. 2000):

1. Palaeozoic creation of the Southern Permian Basin.
2. Early-Middle Triassic subsidence in the Southern Permian Basin, creation of the WNB.
3. Late Jurassic - Early Cretaceous rifting and subsidence
4. Late Cretaceous – Paleogene inversion

2.1.1 Palaeozoic, creation of the Southern Permian Basin

During the Devonian period, the landmasses of Laurussia, Gondwana and several microcontinents were well on their way to assemble the supercontinent known as Pangea. Pangea was taking form during the Late Palaeozoic, and its formation was accompanied by the formation of the Variscan orogeny. From the Late Carboniferous, the northwest and central part of Europe was characterised by two major E-W striking basins, the Northern and Southern Permian Basins. The area now known as the Netherlands would have been part of the Southern Permian Basin, located north of the Variscan mountain belt (Geluk 2005; Van Balen et al. 2000). Part of the foreland basin was the Campine Basin, which now underlays the WNB. The London-Brabant Massif, located between the Variscan belt and the Campine Basin, prevented the transmission of stresses from the belt to the foreland. Therefore, the Permian Basins developed under a relatively calm tectonic regime, showing minor faulting with subsidence patterns until Jurassic times. Because the subsidence patterns of the Southern Permian Basin could not be explained only by crustal loading/cooling, the general concept for Permian to Early Triassic evolution is described by a rifting stage that is succeeded by thermal

subsidence, where the subsidence rates are higher than the sedimentation rates (Duin et al. 2006; Ziegler et al. 2004).

2.1.2 Early-Middle Triassic, subsidence and the formation of the West Netherlands Basin

During Early Triassic times, the Southern Permian Basin continued to subside. The Hardeggen phase, also known as the Kimmerian-I phase, starts the deposition of the Main Buntsandstein Subgroup during extensional tectonics. The Hardeggen phase is subdivided into four phases (1) pre-Volpriehausen, (2) Detfurth, (3) Solling and (4) intra-Solling tectonic pulses. During the Mesozoic breakdown of the supercontinent, partly due to the reactivation of pre-existing fractures, new rifts in the northwest and central Europe started to cut through Variscan elements such as the London-Brabant Massif and Permian Basins. Multiple smaller basins, now referred to as Dutch Triassic basins, were created due to a variance in subsidence rates. These new depressions became focus points for sedimentation (Willems et al. 2020; Duin et al. 2006).

The Volpriehausen, Detfurth and Hardeggen Formation form the Main Buntsandstein Subgroup. The Main Buntsandstein Subgroup consists of repeated alternations of (sub-) arkosic sandstones and clayey siltstones. Each formation contains a large-scale fining upwards sequence onto which smaller fining upwards and coarsening upwards sequences are superimposed. The Main Buntsandstein subgroup as a whole represents a shift from a fluvial-lacustrine dominated (Volpriehausen Formation) to an aeolian-dominated (Hardeggen Formation) system. The succession is about 200 m thick in the Roer Valley Graben, thinning to 100-150 m in the WNB before thickening again to over 300 m in the Broad Fourteens Basin (Geluk 2005). Relative uplift of the Hinterland occurred as a result of the pre-Volpriehausen tectonic pulse; this led to an increase in clastic influx. The increased influx was accommodated by the outwards growth of the fluvial system from the Roer Valley Graben towards the WNB and the Broad Fourteens Basin during the Lower Volpriehausen. The overlying Volpriehausen Claystone Member is of a consistent thickness and reflects the lacustrine environment. In parts of the Southern Permian Basins, the claystone's grade into fluvial/aeolian sandstones of the Upper Volpriehausen Sandstone Member. During the Detfurth and Hardeggen deposition, the influence of aeolian processes became more predominant (Ames et al. 1996).

After deposition, pyritisation and dissolution of feldspar grains occurred. A more dominant process was ferroan dolomitisation at intermediate subsurface temperatures in thickly bedded coarse-grained sandstones, meteoric water enclosed halite and anhydrite. Since the Volpriehausen Formation holds the most significant portion of fluvial sandstone, it was the most dolomitised of the Main Buntsandstein Subgroup (Duin et al. 2006).

2.1.3 Late Jurassic – Early Cretaceous, rifting and subsidence

The Dutch Triassic Basins became part of a stable platform on which the Upper Germanic Trias deposition took place. During Jurassic rifting, the Dutch northwest-southeast striking basins underwent extension due to trans tensional and dextral tectonics. During the Late Cretaceous, the area was tectonically stable but accommodated space due to subsidence. This resulted in the deposition of the Chalk Formation and thus the deep burial of the Main Buntsandstein Subgroup (De Jager et al. 2007).

During or shortly after compaction, anhydritisation took place; this was primarily concentrated in those areas with high porosity and permeability. This process prevented the severe compaction of the Main Buntsandstein Subgroup (Matev 2011). After compaction and during deep burial, non-ferroan dolomitisation occurred (Ursem 2018).

2.1.4 Late Cretaceous – Paleogene, inversion

During the development of the Alpine orogeny, intra-plate and compressional/transpressional tectonics in the northern Alpine forelands resulted in erosion along with the crestal parts of syn-formal structures, and sedimentation once bounded Triassic – Early Cretaceous graben structures. Inversion occurred in four pulses.

The first pulse, the sub-Hercynian pulse, is the only pulse that is observed in the Roer Valley Graben and not in the West Netherlands Basin. Late Cretaceous – Paleogene inversion tectonics thus resulted in tectonic differentiation between the neighbouring systems. Due to thermal contraction, the Roer Valley Graben subsided; meanwhile, the WNB was characterised by continuous inversion and uplift (Wong, Batjes, and De Jager 2007). After tectonically inactive times during the Maastrichtian and Danian, the strongest pulse, the Laramide phase, caused significant erosion. Combined with low sea levels, this resulted in erosion down to the Jurassic strata within the West Netherlands, Central Netherlands and Broad Fourteens Basins (Deckers and van der Voet 2018). The WNB was no longer the major depocenter and under transpressional stress, conditions became a tectonic high (Duin et al. 2006; Matev 2011).

After inversion of the WNB, the second phase of ferroan-dolomitization occurred (Ursem 2018). As erosional processes removed the overburden down to Triassic strata, new 'near-surface' conditions were met. Other important processes are the dissolution of feldspar, anhydrite and quartz grains. This led to an increase in porosity and permeability (Matev 2011).

2.2 Theoretical background of SWIR spectroscopy

Section 1.2 gave a general introduction to the technique of SWIR spectroscopy and its applicability for mineral identification based on characteristic spectral signatures. The following section will provide additional, more in-depth information about SWIR spectroscopy.

2.2.1 Spectral responses

Vibrational processes in certain molecular bonds absorb parts of the electromagnetic spectrum; these absorptions can be detected as spectral responses within the SWIR (1000-2500 nm). The following molecular structures are related to absorption features near the following wavelengths (Pontual et al. 1997):

- Hydroxyl (OH) – 1400 nm (also 1550, 1750 and 1850 nm in some minerals)
- Water (H₂O) – 1400 nm and 1900 nm
- Al-OH – 2160-2220 nm
- Mg-OH – 2230-2295 nm
- Fe-OH – 2300-2360 nm
- Carbonate (CO₃) – 2300-2350 nm (features at 1870, 1990 and 2155 nm are also possible)

Figure 7a illustrates these major spectral absorption features and the ranges of wavelength positions in which they are active (Pontual et al. 1997; Tun et al. 2015). Non-hydroxylated minerals such as silica and feldspar do not give a spectral response within the SWIR range (Pontual et al. 1997).

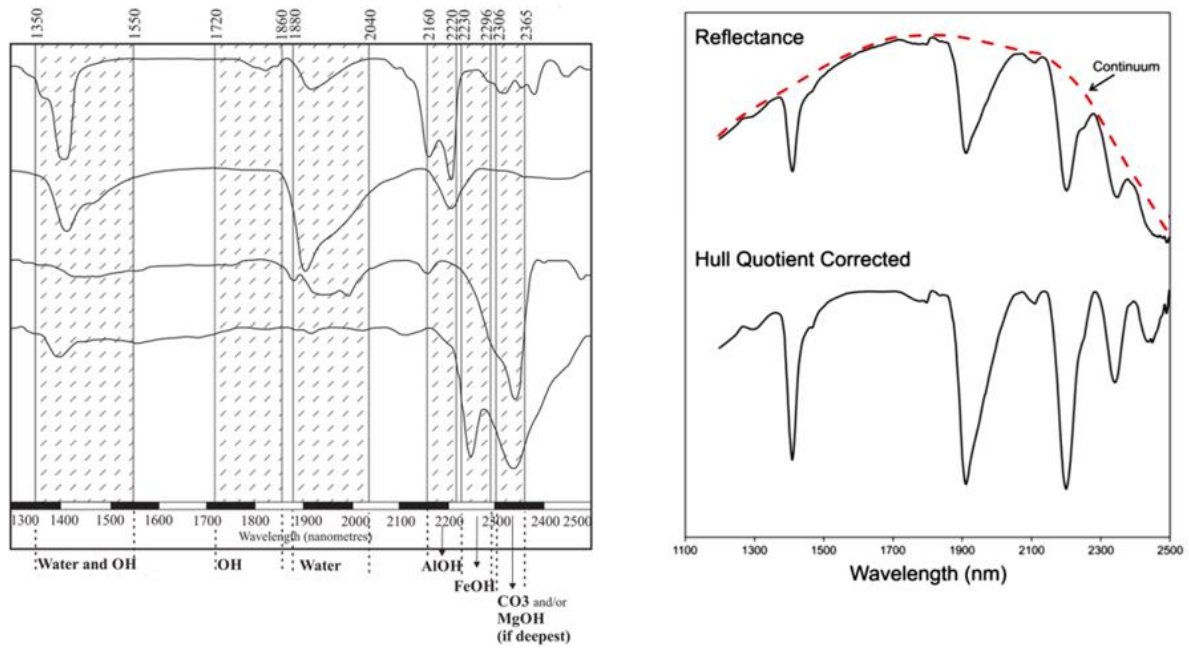


Figure 7: a) (left) Major spectral absorption features within the SWIR range (Pontual et al. 1997). b) (right) Reflectance and hull quotient corrected (continuum removed) spectral profiles for the same sample shown for the SWIR (Simpson and Christie 2016).

To quantify the depth of the absorption features, the overall concave shape of a spectrum should be removed, see Figure 7b. The continuum is a convex hull fit over the top of a spectrum using straight line segments that connect local spectra maxima. This procedure, continuum removal, normalises the data and allows for a better comparison in-between different instruments and/or conditions. After that, the absorption features can be localised using feature finding algorithms, which will be explained in the method section.

The characteristic spectral profiles allow for mineral identification by simple pattern recognition (Clark 1999). Although software is available to do so, the user should make the final interpretation since multiple minerals share similar features. The following sections will provide the needed information to describe the minerals mapped in the SWIR region of the electromagnetic spectrum.

2.2.2 Aluminium phyllosilicates

Aluminium phyllosilicates are also called clays and sheet silicates; these minerals commonly have strong absorption features at 1400, 1900 and 2200 nm, as shown in Figure 7. Montmorillonite, nontronite, illite-smectite, illite, kaolinite and muscovite all have these shared absorption features. To distinguish them from one another, additional spectral characteristics are needed. For example, kaolinite has a characteristic asymmetric doublet at the 2200 nm absorption feature. Illite and muscovite can be distinguished from montmorillonite due to the apparent features at 2350 and 2450 nm. Furthermore, the relative depth of the Al-OH feature at 2200 nm compared to the H₂O feature at 1900 nm can be used to determine 'illite spectral maturity' (ISM) (Calvin and Pace 2016; Mathieu et al. 2017; Doublier, Roache, and Potel 2010). Slight positional variations of the 2200 nm feature are commonly noted. This shift in wavelength position can be linked to the Tschermak substitution ($\text{Si}^{\text{iv}}[\text{Mg}, \text{Fe}^{2+}]^{\text{vi}} = \text{Al}^{\text{iv}}\text{Al}^{\text{vi}}$), which causes compositional variation and results in the transition of muscovite to phengite (Yang et al. 2011).

2.2.3 Fe-Mg phyllosilicates

Chlorite is the most common hydrothermal mineral belonging to the Fe-Mg phyllosilicate group. Spectrally, chlorite is identified using the Fe-OH and Mg-OH features which mainly depend on the ratio of Fe/(Fe + Mg) (Yang et al. 2000). Pontual (1997) uses two diagnostic features between 2235-2259 and 2320-2360 nm. Identifying chlorite is important as its presence has proven to effectively prevent quartz overgrowth, improving reservoir quality (Bjørlykke 2015).

2.2.4 Carbonates

Carbonates (e.g. calcite, dolomite, ankerite, siderite) show several diagnostic absorption features in the SWIR; all features can show considerable changes in location and shape due to the variety in mineralogical composition. The main diagnostic absorption feature is located between 2300 and 2340 nm, with significant left-hand asymmetry, pointing to a more minor secondary feature around 2230-2275 nm. As concentrations of Mg and Fe increase, these features may shift towards shorter wavelengths. It is important to note that the feature above can be mimicked by a mineral mixture comprising phyllosilicates and amphiboles (Laukamp 2011).

In calcite, medium to weak features appear located at 1870 and 1990 nm; these two always appear as pairs. They can be annihilated since they overlap with the OH/H₂O features. However, they might still be helpful if the 2340 nm feature is questionable (Laukamp 2011).

2.2.5 Silicates

Within the studied cores, quartz and feldspar commonly occur. Unfortunately, they do not have absorption features within the SWIR electromagnetic spectrum. However, the H₂O or OH in the mineral structure of some minerals create diagnostic absorption features for some silicates; these are prehnite, opal and zeolites.

2.2.6 Sulphates

The main diagnostic feature of sulphates that are not overlapping with other major groups is the feature near 1740 nm in the case of gypsum and alunite, and around 1850 in the case of jarosite. Absorption features that do overlap are caused by the S-O bonds and do so around 2170, 2220 and 2280 nm (Cloutis et al. 2006). Minerals such as anhydrite and andalusite cannot be observed in the SWIR as they do not have hydroxyl bonds (Savitri et al. 2021).

2.3 Importance of diagenetic processes/mineral assemblages

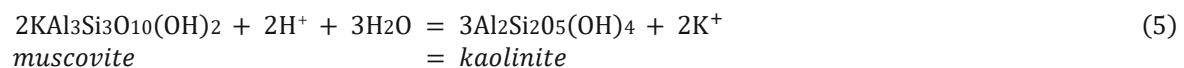
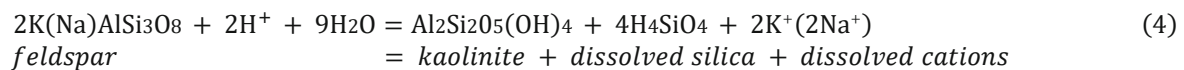
The properties of sandstone reservoirs are functions of the primary composition, which is mainly controlled by its provenance and diagenetic processes. Diagenetic processes alter the original pore type and geometry. This greatly affects porosity, permeability, and physical properties such as seismic velocities and wetting properties (Bjørlykke 2015). The main diagenetic processes are 1) near-surface diagenesis, 2) mechanical compaction, 3) Chemical diagenesis, and 4) Precipitation of cement (Bjørlykke 2015). This section will review important processes that commonly occur within sedimentary basins and sandstone reservoirs and addresses their influence on the reservoir.

2.3.1 Near-surface diagenesis

Early diagenetic properties start as soon as sediments are deposited. At very shallow depths, sediments have the maximum potential to react with the atmosphere and/or meteoric water. The potential to change the bulk composition is therefore thus higher than at greater burial depths. Coatings of iron oxides or clays frequently form; these coatings may slow down or prevent quartz cementation at more considerable depths. In seafloor environments, the redox boundary plays an important role as it represents the equilibrium between the supply of oxygen by diffusion and its consumption by oxidation (Bjørlykke 2015).

The biogenic activity within an area plays an important role. It may improve or reduce porosity and permeability by destroying thin clay laminae, exposing sediment to more oxidation, or mixing clays within clean sand. The complexity of these systems can be illustrated by the effect of the faecal matter of burrowing worms as their faecal matter develops into smectite-rich clays, which in turn develop into chlorite coatings around quartz grains. Which is extremely important due to its role in preserving porosity at greater depths (Bjørlykke 2015). Another example are marine organisms composed of aragonite that dissolve during shallow burial; calcite precipitates as a replacement within the fossils or as cement in pore spaces between the grains, decreasing porosity (Hall et al. 1967; Bjørlykke 2015).

Meteoric water is distilled and therefore undersaturated with respect to all minerals. As it obtains carbon dioxide and sulphur dioxide it becomes slightly acidic. As meteoric water seeps down, it will flow along the most permeable beds into the basin. Here it will dissolve carbonates and unstable minerals such as feldspar and mica. Leaching by meteoric water is generally strong in fluvial and alluvial sediments. The leaching of minerals like feldspar and mica and the precipitation of kaolinite are a function of the flux of water flowing through the amount of rock volume over time; see equations 4 and 5. These reactions indicate that low K^+/H^+ ratios will drive the reactions to the right. The dissolution of feldspar and mica and the precipitation of kaolinite require that the reaction products be constantly removed. Without the thorough flow of water, these reactions do not continue, as the reaction products on the right-hand side of the equations are not removed. The silica released from feldspar dissolution remains in solution due to its inability to precipitate at the low temperatures near the surface. If the silica concentration in the pore water increases too much, kaolinite will no longer be stable, and smectite will precipitate instead (Bjørlykke 2015). As meteoric water travels further into the reservoir, it becomes less undersaturated with respect to minerals and will thus lower its leaching capacity (Bjørlykke 2015).



As meteoric water flushing dissolves feldspar and mica while authigenic clay minerals precipitate. The dissolution produces secondary pore spaces, but the precipitation of clay minerals reduces the porosity, so there is little net gain in pore space. Authigenic kaolinite usually occurs as pore-filling minerals; it does so in clusters and is rarely seen pervasively throughout the entire sandstone. These regions have reduced pore sizes that increase capillary entry pressure, reducing the permeability of the reservoir rock (Bjørlykke 2015). As temperatures exceed 100 °C dickite often replaces some of the kaolinite minerals. Although the similar chemical composition dickite has thicker crystals and is also a precursor mineral for illite (Bjørlykke 2015).

2.3.2 Low depth burial

Mechanical compaction alters the porosity significantly. Experimental data shows that depending on grain strength and size; the porosity may be reduced up to 25-35 % at stresses of 20-30 MPa, corresponding with 2-3 km of burial depth for normally pressurised rocks. Overpressure of the fluid within the rock reduces the effective stress and will thus preserve porosity (Chuhan et al. 2003).

Quartz cementation stabilises the grain framework within sedimentary basins with an average geothermal gradient and prevents further mechanical compaction around 2 km of burial depth (80-100 °C). At more considerable depth compaction becomes more dependent on temperature than effective stress. In sedimentary basins with a low geothermal gradient, quartz cementation may not

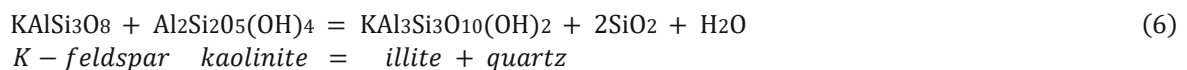
occur before 4-6 km of burial depth. As there is no quartz cement to stabilise the grain framework, further porosity loss will occur by mechanical compaction and grain crushing up to 50 MPa effective stress (Bjørlykke 2015).

2.3.3 Intermediate depth burial

Sedimentary basins that were mainly formed due to subsidence are still relatively loose at depths of 2.0-2.5 km burial depths unless there is a high geothermal gradient or carbonate cement. Prior to quartz or other types of cementation, the reservoir compacts due to sliding, reorientation and fracturing due to the overburden stress. Low percentages of cementation will strengthen the rock at faster rates than the increase in vertical stress from the overburden, preventing further mechanical compaction. High geothermal gradients and slow subsidence rates favour the amount of quartz cement at specific depths (Bjørlykke 2015).

If, in an earlier stage, a coating of minute quartz crystals forms on the surface of clastic quartz grains, the process of quartz cementation can be inhibited. This occurs as amorphous silica dissolves and produces a high supersaturation of silica relative to quartz. This high supersaturation of silica precipitates at low temperature (60-80 °C) and is a good preservative of high porosity at more considerable depths (5 km). At higher temperatures, the porewater will not reach the same levels of silica supersaturation with respect to quartz and will remain insufficient to precipitate quartz onto micro-quartz (Bjørlykke 2015). Smectites dissolve at temperatures near 70-80 °C and are replaced with mixed-layer illite smectite and illite minerals. The formation of illite from smectite occurs within the range of 70-100 °C, and the illitisation of such may slightly improve the reservoir quality as illite has a lower specific surface area than smectite. Sandstone reservoirs containing smectites tend to have poor reservoir quality (Bjørlykke 2015).

The kaolinite, dickite and K-feldspar minerals are the main minerals that form illite in potentially good reservoir rocks. Above 130 °C, K-feldspar and kaolinite are no longer thermodynamically stable and form illite as described in equation 6.



Albitisation is the process in which K-feldspar or plagioclase is replaced by albite. This is often observed within sandstones at burial depths of 3 km. As albite becomes the more stable mineral, partial replacement of K-feldspar and plagioclase grains occurs. This replacement itself does not change reservoir properties significantly. However, the Albitisation of plagioclase will release Ca²⁺ that may precipitate as calcite (Bjørlykke 2015).

2.3.4 Deep burial

Most sedimentary basins show a substantial porosity and permeability reduction in sandstone reservoirs from 3.0-3.5 km to 4.0-4.5 km burial depth, corresponding to temperature ranges of 120-160 °C. This is primarily due to the precipitation of quartz cement and the formation of diagenetic illite. Temperature plays a significant role in these processes, with higher temperatures yielding higher rates of quartz cementation. Contacts between mica or illitic clay and quartz are preferred areas of pressure solution (Bjørkum et al. 1998). The process of quartz cementation can continue as long as the temperature is above 70-80 °C and there is sufficient porosity within the sandstone (Bjørlykke 2015). Quartz grains with coatings of other minerals like chlorite or substances like petroleum or bitumen hinder the quartz overgrowth down to these depths. At 4-5 km burial depth or 40-50 MPa effective stress, this results in pervasive grain crushing, favouring reservoir properties (Chuhan et al. 2003).

2.4 SWIR spectroscopy versus other methods

Every mineralogical analytical method has detection limits, such as chemical composition, grain size and abundance. To obtain a more complete mineral identification, several analytical methods are used. The main analytical methods currently used for reservoir characterisation are binocular microscopy, methylene blue stain testing (MeB), petrography, and X-ray diffractometry (XRD). For more information about chemical compositional data and higher spatial resolution level of analyses, backscatter electron (BSE) imaging combined with energy dispersive spectroscopy (BSE-EDS) and electron microprobe analysis (EMPA) can be added to the routine (Savitri et al. 2021). Since Yang et al. (2000), SWIR spectroscopy has found broader applications within the geothermal industry. The following section will provide the common strengths and limitations of the main analytical methods, after which the same is done for SWIR spectroscopy.

2.4.1 Petrographic analysis of thin sections

Basic petrographic analysis is performed using a polarising microscope. Once samples are prepared, polarising light microscopy provides a non-destructive way to identify solid substances with relatively high spatial resolution.

Once samples have been selected, they will be prepared for thin sectioning. Using a vacuum, the samples will be impregnated with low-viscosity epoxy; it is possible to apply extra pressure to force epoxy into even smaller pores. Staining the epoxy with fluorescent dye might help observations in later stadia. If specific minerals such as calcite, dolomite, ferrous carbonates, K-feldspar and plagioclase are important to the analytical objectives special stains are available (Einhardt et al. 2012).

Petrographic analysis has multiple strengths. The main one is that due to the high spatial resolution, it is possible to investigate the paragenesis of a reservoir. This provides valuable information about the sequence of events and might help understand a reservoir's diagenetic history. However, the high labour intensiveness does not lend well to a spatially continuous dataset. Therefore, thin sections are commonly only made from the same samples as the porosity-permeability plugs are taken from. Another major downside is that clay minerals are not distinguishable (Savitri et al. 2021).

2.4.2 X-ray diffraction (XRD)

When an intense X-ray beam is aimed at a crystalline material, the x-rays are scattered by their ordered internal atomic arrangement. XRD uses a powdered form of the sample to diffract X-rays; by measuring the angles and intensities of these diffracted beams, a three-dimensional picture of the density of electrons within the crystal can be produced. These peaks are characteristic for known minerals and compounds.

XRD analysis produces semi-quantitative bulk mineralogy of the sample and is a widely used method for clay characterisation.

2.4.3 SWIR spectroscopy

The sample preparation needed for SWIR spectroscopy is, contrary to the other methods, negligible since its main concern is that the sample should be clean and dry. In Sweden, the 'drill core scanning project' led by the Swedish Geological Survey can scan more than 2000 meters of drill core within an 8-hour shift (Specim 2015). This method of core scanning produces a continuous data set for the scanned material and is non-destructive.

Mineral abundances measured with SWIR spectroscopy usually are overestimated due to the exclusion of spectrally inactive minerals (e.g., quartz, feldspar). However, keeping that in mind, it is

suitable for a wide variety of minerals, including clay minerals (Savitri et al. 2021). Other research has shown that variations in crystallinity and composition within minerals can be distinguished (Pontual et al. 1997).

3 Dataset and methodology

A schematic overview of chapter 3 is given in Figure 8. It presents the available data for both cores, the steps necessary to obtain the hyperspectral data and the parameters calculated from it. These datasets will be compared and validated to the data obtained by literature reviews and/or other analytical methods.

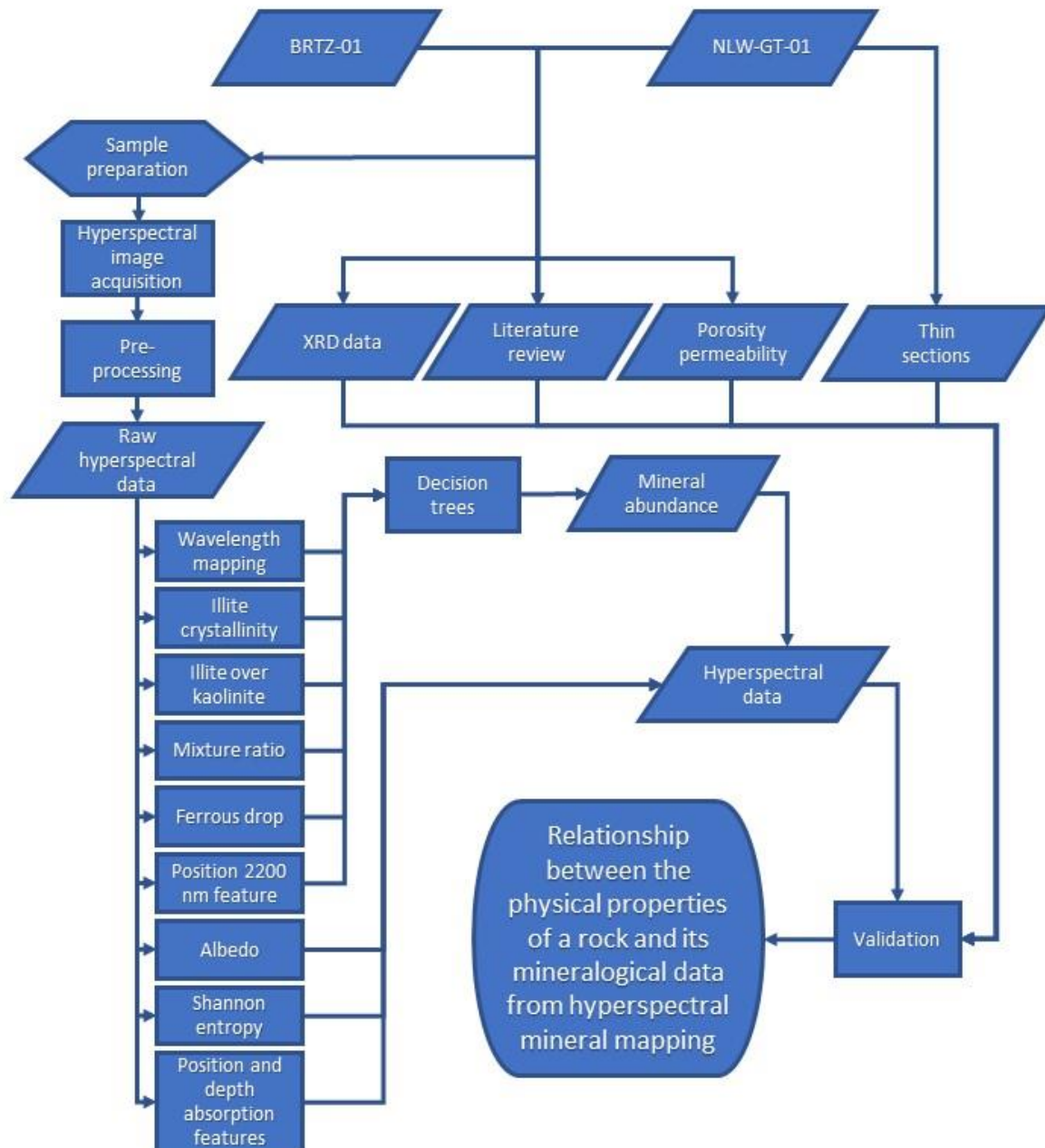


Figure 8: Flow chart of research methodology.

3.1 Materials and dataset

A comparison between datasets will be made to investigate whether correlations between the hyperspectral data and the physical rock parameters can be established. The processed hyperspectral data will be analysed and linked to already existing records and earlier research that has determined the physical properties of the samples, see table 1 (“NLOG” 2021; Maniar 2019; De Hoo 2021; Chang, Zoback, and Khaksar 2006; Van Bergen et al. 2008).

It is important to note that data within this research was obtained via multiple parties and different analytical methods. This might bring other analytical errors to them. For example, the NAM’s porosity measurements for BRTZ-01 were done via the ‘Heptane traditional method’ and mercury porosimetry, and permeability was measured with air. While the porosity measurements for NLW-GT-01 were made by PanTerra using helium expansion in a Boyle’s Law Porosimeter, and permeability was determined with nitrogen.

Regarding porosity, in practice, there is always a small pore volume that is not accessed by the mercury injection method. The small size of helium molecules means that they can penetrate pores too small for mercury injection. Consequently, gas expansion with helium gives higher porosities than mercury injection (Campbell 2011; Anovitz and Cole 2015). The mercury injection method is thus less accurate. However, no complications are expected since the measured differences in porosity lay far beyond the error margins of these methods.

When permeability is calculated using gasses, a gas specific correction is needed, the Klinkenberg correction. Because this correction is integrated within the methodology, there are no expected complications due to the use of nitrogen versus air, especially since air is $\pm 79\%$ nitrogen (Tankikawa et al. 2006).

Table 1: available data for research

	Core	Plugs	Core Plugs			Thin Section	Wireline logs						FMI	XRD
			Porosity	Permeability	Grain Density		Gamma Ray	Calliper	Neutron	Density	Sonic	Resistivity		
NLW-GT-01	✓	✓	✓	✓	✓	✓	✓	✓	✓	✓	✓	✓	✓	✓
BRTZ-01	✓	Not present	✓	✓	✓	X	✓	✓	✓	✓	✓	✓	X	✓

3.1.1 Samples

The two boreholes used for this study are the NLW-GT-01 and BRTZ-01, as mentioned in section 2.1. The boreholes are 25 kilometres apart and are cored at different depths. The NLW-GT-01 well is cored from 4250-4280 meter (measured depth) and consist of the Detfurth (4190-4255 m) and the Upper Volpriehausen (4255-4356 m) sandstone member. The BRTZ-01 well is cored from 2746-2789 meters (measured depth) and consists of the Solling Claystone member (2738-2755 m), Basal Solling Sandstone member (2755-2762 m), Lower Detfurth Sandstone member (2762-2770 m), the Upper Volpriehausen Sandstone member (2770-2845 m) and the Lower Volpriehausen Sandstone member (2845-2899 m) (Maniar 2019; “NLOG” 2021).

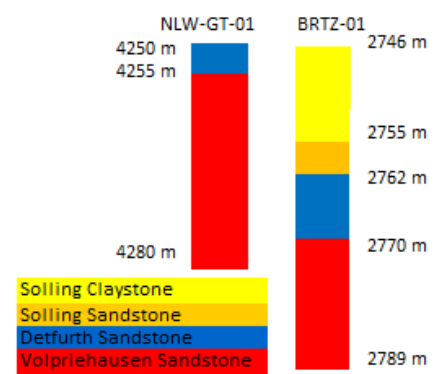


Figure 9: Lithology NLW-GT-01 & BRTZ-01 by measured depth.

All core that is present is so in the form of polymer slabs. Although plugs have been taken and measurements have been taken of both cores, only plugs and hotshots of the NLW-GT-01 were present for scanning. For a complete list of materials used within this MSc thesis, see appendix 1.

Before transporting the samples towards ITC Twente, all polymer slabs were thoroughly cleaned using pressurised air.

3.1.2 Available data

This section will show available data on both cores that will be compared with the hyperspectral data. Figure 10 illustrates the mineral content, porosity and permeability of both cores. A clear distinction between the core's porosity and permeability can be made since the BRTZ-01 core reaches significantly higher values than the NLW-GT-01 core. Overall higher quartz and feldspar content are shown within the BRTZ-01 measurements, while higher carbonate and clay values are shown in the NLW-GT-01 samples.



Figure 10: NLW, mineral content based on (De Hoo 2021), and porosity permeability measurements from ("Geological Report TW OK II PanTerra Project G1363b" 2021). BRTZ, mineral content from XRD measurements from NAM as their porosity permeability values (NAM BV 2000). The yellow line indicates the Lower Detfurth Sandstone Member/Upper Volpriehausen Sandstone Member boundary.

3.1.3 NLW-GT-01

The NLW-GT-01 core was extensively logged by Maniar (2019), who described the following. Within the NLW-GT-01, grain sizes range from very fine to medium-grained sandstone with an occasional coarse-grained sandstone zone at specific intervals. No preferential vertical succession of lithofacies is apparent. The colour of the sandstone ranges from light to medium grey (N7-N5, at the Munsell colour chart). Almost the entire core shows cross-bedding features, with four distinct fractures at depths of 4258.30, 4259.30, 4273.70 and 4273.75 m. These fractures dip against the direction of the cross-beds. Cross-beds between 4271.80 m and 4273.90 m are well preserved, vary in set ranges from 5-20 cm and have well-defined foresets. The foresets have an apparent upward increase in the dip angle from 10 to 20 degrees and a gradual decrease towards the top. These changes in dip angles reflect that the trough cross-stratification was deposited in the form of sigmoidal cross-beds. Around 4271.90 m elongated clay pebbles are aligned along the beds, indicative of the known extensional phase. Near 4270 meters, an apparent change from dip angles occurs from around 2

degrees towards 25 degrees dipping foresets (bottom/top), considering the 39 degrees well deviation. At 4261 meter depth, centimetre scale alternation of fine sands and silts occurs. Lastly, at 4,259 m, flattened sandstone pebbles (<3cm) are present in a finer-grained matrix and a fracture opposite of the cross-bedding is present (Maniar 2019).

As determined by neutron density and neutron-sonic logs, the porosity is less than 5%. However, due to a poor correlation ($R^2=0.2079$) with the porosity as determined from core plugs, this may be due to the limited amount of core plugs. Therefore the data points on porosity stay limited (Figure 10) (Maniar 2019; Felder and Fernandez 2018).

The following section provides the available data from research on thin sections by Felder and Fernandez (2018) and De Hoo (2021). These are obtained from hotshots (HS) 1, 2 and 11 and from horizontal plugs 1, 4, 11, 16, 25 and 29.

HS1 has the highest measured porosity and permeability of all measured hotshots within the NLW-GT-01. However, these pores are poorly interconnected, resulting in low permeability. Most intergranular pore spaces are filled with Fe-dolomite cement. Also present is K-feldspar; these are virtually un-leached but partially deformed due to compaction. Quartz cement locally overgrows detrital quartz grains, especially when dolomite is absent. HS1 is the only thin section in which pore-filling anhydrite cement is found.

HS2 has the highest grain density and extremely poor porosity and permeability values of all measured hotshots. Small rip-up clasts can be seen that are dominantly composed of dolomite. Dolomite cement is common in the sample; it occurs in both Fe-rich and Fe-poor. Strongly deformed clay-rich clasts indicate a high degree of mechanical compaction. Most compaction occurred prior to dolomite cementation.

Of all measured hotshots, HS11 is the most poorly sorted sample of the analysed samples. Grain shapes vary between subangular and subrounded, with grain contacts indicating moderate compaction. The sample is strongly cemented with patches of dolomite and quartz cement. Faint outlines of carbonate grains are visible but are heavily overgrown by dolomite. Macropores are present. Detrital illite grains are present throughout the whole sample; they are squeezed in-between the quartz grains due to mechanical compaction. The compaction of ductile grains has reduced the reservoir quality already prior to the dolomite cementation.

All hotshot thin sections are predominately quartz (63-68%). According to whole rock XRD data, monocrystalline quartz is more common than polycrystalline quartz. K-feldspar grains have a distinct boundary, whereas plagioclase feldspar appears partially leached (microcline 4-6%, albite 5-6%). Both Fe-rich and Fe-poor dolomite is present (14-21%). In HS2 and HS11, calcite cement is preserved as cores in the Fe-rich dolomite; their boundaries are not distinct. Fe-rich dolomite mainly fills the primary macropores but is rarely observed in secondary pores.

Data from the horizontal and vertical plugs is obtained from De Hoo (2021). Using digital imaging De Hoo analysed the Triassic sandstone plugs. Observations made are in agreement with statements made by PanTerra. Mineral identification was made on a select number of samples; however, a total of 57 thin sections are available in plane-polarised light (PPL) and cross polarised light (XPL). These thin sections have a thickness of 35 μm and are made approximately every half a meter.

3.1.4 BRTZ-01

The Barendrecht-Ziedewij reservoir rock was thoroughly studied in CATO-2 and reported by Koenen et al. (2014). Porosity, permeability and average grain density measurements were obtained

by the NAM (2000). Whole-rock XRD data of reservoir samples were provided by GEOCHEM and were obtained from Van Bergen et al. (2008).

The dominant detrital mineral within the cored BRTZ-01 is quartz, as it is in NLW-GT-01. These quartz grains have a rounded or elongated shape. The feldspar found is mostly k-feldspar, albite is rare. Most k-feldspars are partially albitised and show dissolution along cleavage planes and/or show corroded rims. Mica's present are dominantly muscovite and biotite. Detrital micas are squeezed between k-feldspar and quartz grains. Authigenic clay minerals partially replace biotite and some muscovite grains. In the samples, authigenic kaolinite is the most common clay mineral, apart from primary illite in clay clasts. Vermicular type of kaolinite occurs as a product of k-feldspar and mica alteration or within the intergranular pore space. Kaolinite that is present due to k-feldspar dissolution can be seen to fill up secondary pore space. The kaolinite in primary pores is well ordered and can be observed with the booklets structure. Larger booklets are alternating crystals of kaolinite and either illite or biotite/muscovite. These layers are rich in K with a significant amount of Mg and Fe and can be interpreted as mica alteration to kaolinite and illitisation to kaolinite. Kaolinite is either the result of mica alteration or k-feldspar leaching (Koenen, M., Heege, J.H., Peeters 2014).

Zoned dolomites are commonly present with maximally three growth zones. Multiple types of siderite are recognised based on their morphologies and association. As kaolinite replaces biotite, it is often associated with anhedral, granular siderite crystals. Similar siderite is also abundant within clay clasts. The zoned dolomites are often surrounded by small patches of siderite; these patches contain micropores. Large pore filling siderite cement can also be observed and replaces earlier authigenic quartz. Lastly, euhedral siderite grains forming aggregates are observed, which grew adjacent to or replaced quartz overgrowth.

At the top of the reservoir, anhydrite is the most common cement. It formed large patches of blocky poikilitic pore-filling cement. As it encloses intragranular kaolinite within residual k-feldspar, the k-feldspar alteration to kaolinite was prior to the anhydrite cementation; see Koenen et al. (2014) for thin sections.

Table 2: Mineralogical and porosity permeability data from the literature on NLW-GT-01 and BRTZ-01 (De Hoo 2021; Felder and Fernandez 2018; Koenen, M., Heege, J.H., Peeters 2014).

Borehole	Lithology	Sample	Depth (m)	Porosity (%)	Permeability (mD)	Quartz	Feldspar	Anhydrite	Carbonates	Clay	
NLW-GT-01	Detfurth Sandstone	HO 01	4250.03			75	4	1	14	3	
		HS 01	4251.26	3.9	0.04						
		HS 02	4254.25	1.4	<0.01						
	Volpriehausen Sandstone	HO 11	4259.99				60	2		7	30
		HO 16	4265.00				67	4		25	5
		HS 11	4266.62	1.6	0.01						
		HO 25	4273.75				72	5		12	10
		HO 29	4277.76				80	5		10	5
	BRTZ-01	Detfurth Sandstone	NM0193	2763.85	15.8	70.73	82	15		1	2
NM0200			2765.95	18.9	34.32	85	6		6	3	
Volpriehausen Sandstone		NM0238	2779.05	14.7	6.40	82	7			8	3
		NM0243	2780.60	18.6	196.66	76	6			5	13
		NM0256	2784.55	11.1	4.27	67	5	2		17	9
		NM0267	2787.85	13.1	5.44	62	5			24	9

3.2.1 Instruments

The hyperspectral images were obtained using Specim spectral camera equipped with the OLES30 lens (SPECIM 2015; W. Bakker 2018). The camera setup is located in the Geo-Science Laboratory at the University of Twente, Faculty ITC, Enschede, the Netherlands. Table 3 gives the technical specification of the camera in the used setup for this study.

The hyperspectral images are processed and studied using two programs, Hyperspectral Python (HypPy3) and ENVI (W H Bakker 2021; Harris Corporation 2018).

Table 3: Technical Specifications of SWIR camera in ‘lab stage’ setup at ITC Twente.

<i>Lab stage setup at ITC Twente</i>	
<i>Spectral Range (nm)</i>	1000-2500
<i>Distance of the sensor to sample (cm)</i>	30
<i>Pixel size (µm)</i>	256
<i>Image swath (mm)</i>	98
<i>Number of bands</i>	288
<i>Lens focal length (mm) – (OLES30)</i>	30
<i>Spectral Sampling (nm)</i>	5.6
<i>Spectral resolution FWHM (nm)</i>	12
<i>Frame rate (frame/s)</i>	38.9
<i>Scan speed samples (mm/s)</i>	10
<i>Scan speed white reference (mm/s)</i>	15
<i>Exposure time (ms)</i>	2.1

3.2.2 Image acquisition

Samples in the form of plugs or hotshots were placed in order on plastic trays wrapped in a light-absorbing cloth, reducing the background noise of the plastic tray. Samples in the form of polymer slabs were placed using their original container without any covering. The samples were placed on the platform (see Figure 11, E). Each placement was checked and adjusted with scissor rack lifting platforms to ensure that the sampled surface was at the camera’s focal point. If correct, an image with a sample tag was taken by mobile phone for later reference. The room was darkened entirely to remove any variance due to daylight or other factors. Then the hyperspectral image was recorded with appropriate metadata. The platform would move from right to left (Figure 11), starting by scanning the reference plate (C) obtaining a white and dark reference surface for image calibration. A total of 104 scans were made: 33 of NLW-GT-01 slabs, 47 of BRTZ-01 slabs, 2 for the NLW-GT-01 hotshot samples, 1 for the NLW-GT-01 horizontal plugs and 1 for the NLW-GT-01 vertical plugs.

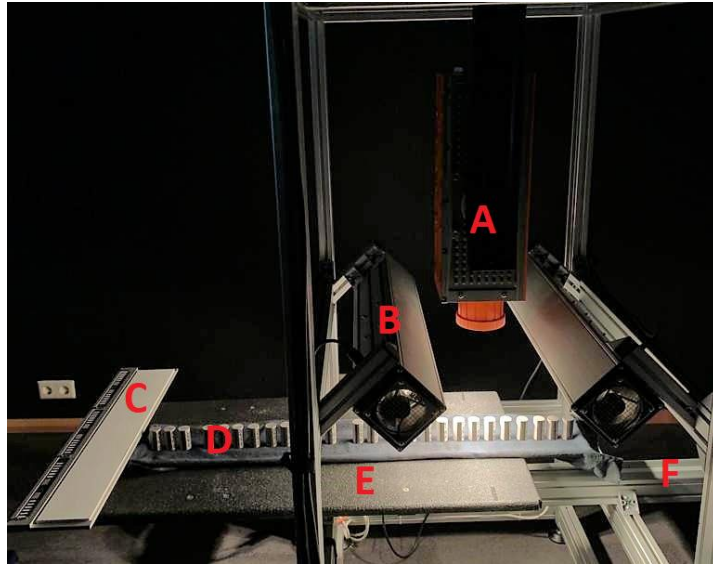


Figure 11: SWIR camera setup at ITC Twente, (A) SWIR camera, (B) Light source, (C) Reference plate, (D) Sample tray with plugs, (E) Platform, (F) Platform track.

3.2.3 Pre-processing

Image pre-processing was done to prepare data for further processing techniques and to remove undesirable pixels. The following pre-processing steps were applied:

- Dark and White Reference (HypPy):

The raw digital number values (DN) were converted into the reflectance image using the dark and white reference tool in the HypPy3 software (Wim H. Bakker 2012).

- Spatial Subset (ENVI):

Unwanted pixels, like the ones containing resin, cloth or other non-rock materials, were subsetted from the image file. This was done by classifying pixels based on spectral profile using region of interest endmember collection and the spectral angle mapper (SAM) technique. SAM is an automated classification method that compares the image spectra against a known spectra or endmember. Both spectra are represented as vectors, and the angle between them is measured. Since the resin's spectra within the trays significantly differ from any rock spectra, this method created the first rough classification. This was manually checked and corrected as high reflectance resin and resin rock combinations were often wrongly classified. Scans of plugs and hotshots were separated into smaller files of singular samples.

In a later stage, a Linux shell script was written to subset slab images into the desired image size, see appendix 2. This was done so image file reports would give specific information about smaller areas of the slabbed core instead of only reporting within the full slab size.

- Spectral Subset (HypPy):

The removal of unwanted bands 1-16 (894-980 nm) and band 288 (2511 nm) as they had bad images. This was done to improve the overall quality of the image.

- De-stripping (HypPy):

To remove dead or bad pixels, a two-step method was used. Firstly, the de-stripping filter within the HypPy3 software was used at a large threshold value of 10. Using the offset image, threshold values were determined. After that, the de-stripping filter was used again at low threshold values, replacing bad pixels.

- Spectral smoothing (HypPy):

Based on the median and mean filter program the images were smoothed using the mean 7 (Fast Mean, 1+5+1) filter. This process smoothens the spectra necessary for later classification techniques.

3.3 Image processing

Multiple techniques were applied to obtain the wanted information from the hyperspectral images. The following section will elaborate on these techniques.

3.3.1 Spectral analysis

The G-MEX (Geologically based spectral analysis guides for Mineral EXploration) of Pontual et al. (1997) was used as a guideline for the spectral identification of minerals. The most important considerations are summarised below:

- Most SWIR active minerals have a characteristic feature between 2050-and 2450 nm.
- Based on absorption features and the wavelength position, minerals can be classified into spectral groups.
- An absorption feature's position, shape and depth relative to that of another feature should be taken into account.
- Reflectance spectra can be influenced by other absorption features, e.g. ferrous iron absorption affects the overall background shape of the spectrum by causing a spectral drop in front of the 1000 nm spectral region.
- As mineral mixing occurs, features such as additional absorption features, additional shoulders, inflexions on the dominant mineral, increase of depth, feature broadening or feature shifting can occur and should be taken into account.

The outcome of this approach will give the first indication of the minerals present in the samples. The obtained spectral signatures were compared with the USGS spectral library in ENVI, absorption features as provided in the G-MEX, Infrared Spectroscopy of Minerals and Related Compounds, and the SWIR Functional Groups of Rock-forming Minerals of The Spectral Geologist (TSG) (Pontual et al. 1997; Chukanov and Chervonnyi 2016; Laukamp 2011).

3.3.2 Wavelength position mapping

As described by Van Ruitenbeek et al. (2014), Wavelength position mapping is a semi-automated method to identify minerals. This method produces the position and depth of the three deepest absorption features with a set range. The wavelength position maps were created in two steps.

The first step determines the wavelength interval that will be examined. Specifying this is important as deep features such as the OH and H₂O feature might otherwise overrule the absorption features of interest. This research set the wavelength intervals at 1300-1600 nm, 1650-1850 nm, 1850-2100 nm, and 2100-2400 nm. These interval ranges provide a wide coverage yet detailed information per interval due to the active spectral absorption features within them. A continuum removal is applied to accentuate spectral absorption features on the specified wavelength ranges. This normalisation of the reflectance spectra is done according to the method of Clark and Roush (1984). The wavelength position of the deepest absorption feature is then determined by a second-order polynomial that is fitted to three consecutive bands, of which the centre band has the lowest reflectance (Rodger et al. 2012; Van Ruitenbeek et al. 2014). However, this process may ignore shallower absorption peaks such as within a doublet, as present in kaolinite. The interpolated wavelength position of the minimum of the resulting parabola will be calculated, as well as the depth

of that absorption feature, see Figure 12. The position of the deepest absorption feature and its depth is calculated by the formula:

$$w(x) = a^2 + bx + c \quad (7)$$

Where $w(x)$ is the interpolated reflectance value at position x , x is the wavelength position in μm , and a , b and c are coefficients of the parabola. Therefore, the minimum of w is given by:

$$w_{min} = -\frac{b}{2a} \quad (8)$$

And thus, the depth of the interpolated absorption feature is calculated with:

$$depth = 1 - f(w_{min}) \quad (9)$$

Within this MSc thesis, the three deepest absorption features for each spectral region were calculated.

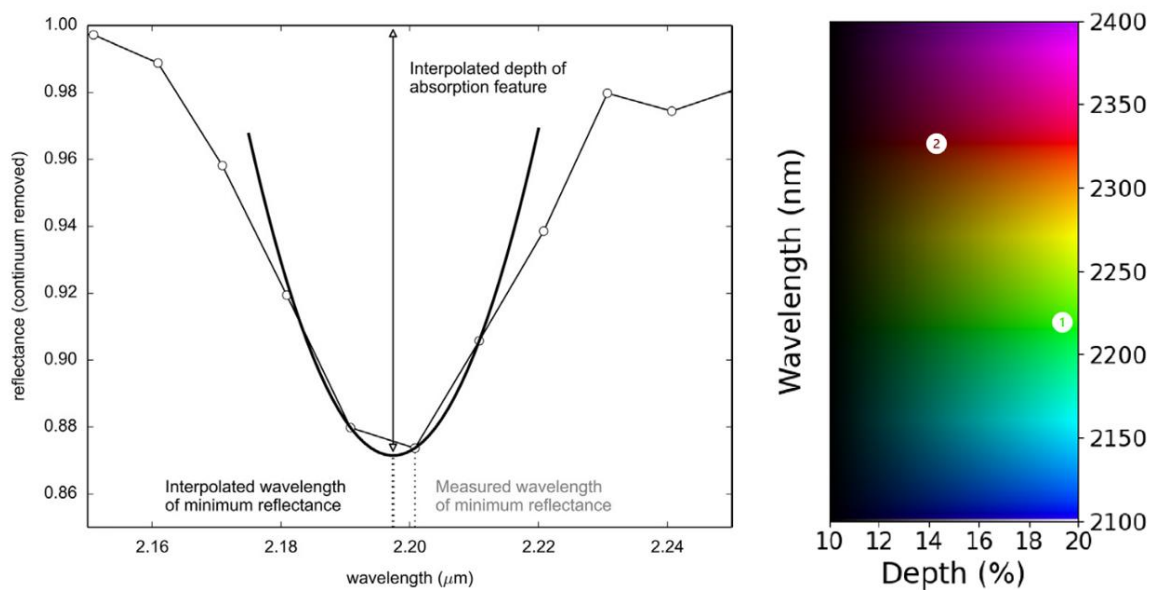


Figure 12: a) (left) interpolation method for determination of the deepest absorption feature by fitting a parabola through three consecutive points (from Van Ruitenbeek et al. 2014). b) (right) Legend of 2100-2400 nm wavelength map, whereas a pixel would colour bright green (location 1) it would have a strong absorption feature in-between 2200 and 2250, whereas if it would colour dull red (location 2), the strongest absorption feature would not be very deep and within the 2300-2350 range.

In the second step, a file is created that contains the three deepest absorption features and their relative depths to the continuum. This file can be seen as an RGB image. The hue (colour) illustrates the wavelength position and the intensity illustrates the depth of the absorption feature. See Figure 12 for illustrative purposes (Van Ruitenbeek et al. 2014).

3.3.3 Albedo

An albedo image of the samples is generated using the 'Log Residuals' tool within HypPy. The log residuals method is a two-step normalisation method in which the spectra of the pixel are normalised first, and then the pixels are divided by the mean spectrum of the whole image (Wim H. Bakker 2012). This results in a greyscale image of the sample in which pixels are divided into dark, medium-dark, medium-light, and light.

This is done for two reasons, 1) the albedo output provides a visual representation of colour alteration within the sample. 2) Areas of low albedo have lower reflectance values than high albedo areas, affecting the relative depth of absorption features.

3.3.4 Ferrous drop

Ferrous iron absorption affects the overall background shape of the spectrum by causing a spectral drop in front of the 1000 nm spectral region. By calculating the slope near this spectral range, it is possible to indicate the iron content of a pixel (Pontual 1997). To do so, the 'ferrous drop' is calculated.

The Ferrous drop represents the ratio between the 1600 nm and 1310 nm band. It is important to note that these calculations are done on spectra that have not seen a hull correction, as this could influence/remove the effect of Fe^{2+} on the spectrum. The calculated ferrous drop is then coloured using a decision tree. High values represented by darker colours are representative of a steep slope and thus a more significant influence of iron-bearing minerals. According to Martynenko et al. (2017) the ferrous drop value correlates well with the amount of Fe^{2+} in the crystal structure of a mineral. This parameter will later be utilised within carbonate classification to distinguish minerals within the carbonates group. There is an increase in ferrous drop towards Fe-rich dolomite and siderite, see Figure 13.

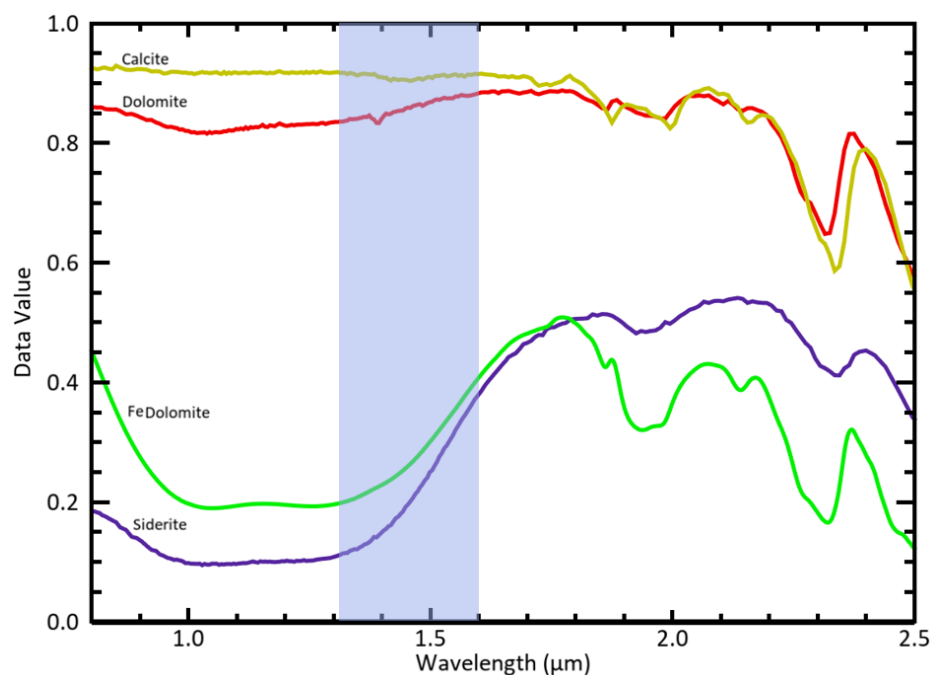


Figure 13: Spectral responses of carbonate minerals (top to bottom: calcite, dolomite, Fe-rich dolomite, siderite), highlighting the steepening within the 1310-1600 nm range, illustrative of the increase in ferrous drop.

3.3.5 Illite crystallinity

Since illite, illite-smectite, and smectite have similar positioned absorption features, we use their difference in intensities at 1400 nm, 1900 nm and 2200nm to distinguish them. By calculating the ratio between the H_2O -feature at 1900 nm divided by the AlOH -feature at 2200 nm, the crystallinity value is determined; as the water absorption feature becomes less intense with a higher degree of crystallinity, the ratio shifts. The Illite crystallinity value represents the ratio between the depth of the deepest feature within the 1850-2100 nm range divided by the depth of the deepest feature within the 2100-2400 nm range. The calculated illite crystallinity is then categorised using a

decision tree. This enables the observation of relative compositional changes in the samples between smectite, smectite-illite mixture, illite and muscovite (Simpson and Rae 2018; Simpson 2015). Low crystallinity values indicate a more smectite rich composition, with high values being an indication of muscovite. To eliminate values comprised of other absorptions than the AIOH-feature, a subdivision is created by removing pixels in which the deepest value of the 2100-2400 nm range does not lay within the 2185-2225 nm.

3.3.6 Illite over Kaolinite

The Illite over kaolinite value represents the ratio between the value of the spectrum at 2164 nm divided by the value of the spectrum at 2180 nm. Since kaolinite has a doublet absorption feature near the 2200 nm feature absent in other aluminium phyllosilicates, an indicative distinction can be made; Figure 14 illustrates these differences.

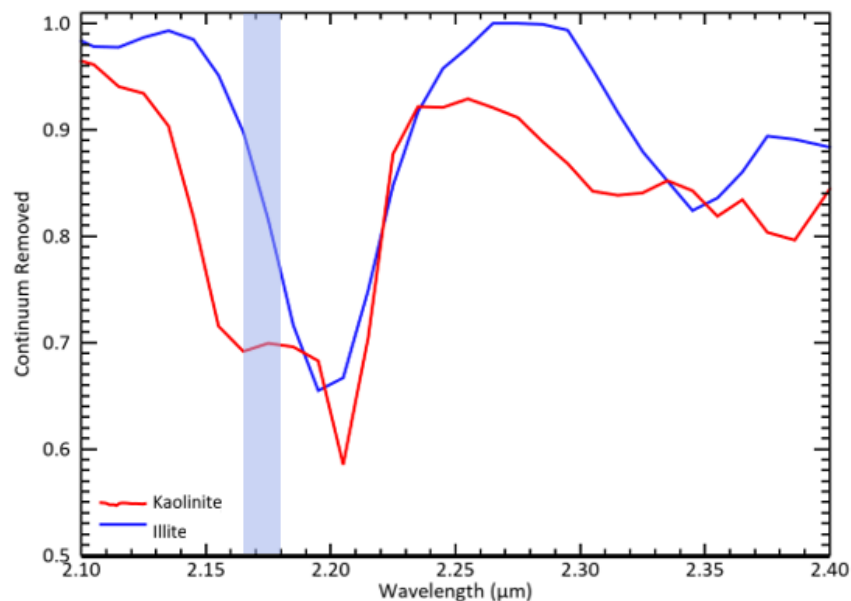


Figure 14: Spectral response of kaolinite within the sample, the spectral library version of kaolinite and illite within the 2100-2400 nm range. The slope within the highlighted area is indicative for the illite over kaolinite calculation.

3.3.7 Position and depth of absorption features

The position and/or depth of many absorption features are measured as separate parameters. For the AIOH feature at 2200, studies have shown that its position is representative of distinct mineral compositions. Others may not have a literature background, however, they may show interesting results.

The position of the 2200 nm feature is determined with a decision tree on the earlier calculated wavelength map of the 2100-2400 nm range. When the observed absorption feature is not within the 2185-2230 nm range, and it is not the first or second largest absorption feature within this range, it is not accounted for. The change in position of the 2200 nm feature is used to evaluate the differences within aluminosilicates (van Ruitenbeek et al. 2006). When the position of the absorption feature is below 2210 nm, it is interpreted as more muscovitic illite, while positions above are more that of phengitic illite (Mg and/or Fe-rich) (Kurt O. Kraal et al. 2021).

The depth of the 1900 nm feature is used as an analogy for relative hydrous clay content. Relative higher hydrous clay content may indicate that fracture networks were more interconnected and/or permeable in the past, supporting hydrothermal fluid flow and water-rock interaction (Kurt O.

Kraal et al. 2021). The strength of the 1900 nm feature is determined with a decision tree on the earlier calculated wavelength map of the 1850-2100 nm range. The observed feature must be stronger than 0.05 and must be between 1880 and 1930 nm; otherwise, it is not accounted for. The strengths are categorised by step sizes of 1 up to a measured depth of 0.30. Then the step size increases to 5 until the category above 0.45 is added. In further reference, the strength of the 1900 nm feature is written with a factor of 10, transforming into a 0-100 scale, with 100 being maximal absorption.

3.3.8 Mixture ratio

Many spectral absorption features are active within the 2100-2400 nm region. Due to the small grain size of the cores, many pixels are constructed by a mixture of spectral profiles. The most important one is illustrated in Figure 15. As spectral mixtures change from phyllosilicate rich to more carbonate-rich, the strength of the 2200 nm feature decreases and the 2340 nm shifts towards lower wavelengths and becomes deeper. The mixture ratio calculates the distance between these two values as a ratio.

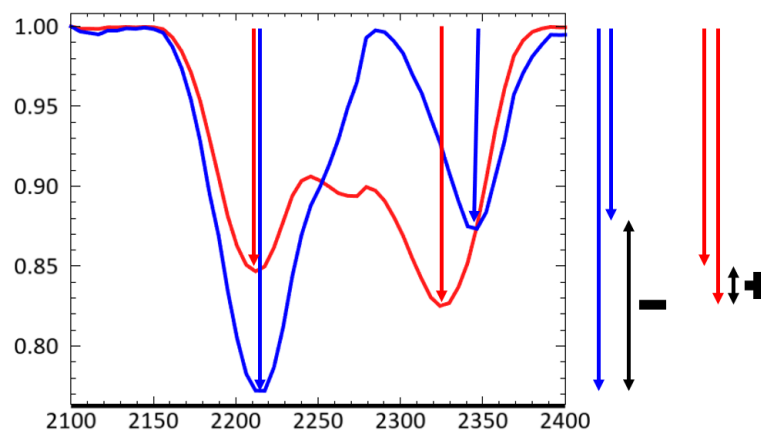


Figure 15: Mean spectral profile of hull corrected samples, blue phyllosilicate rich, red – carbonate-rich. With arrows indicating the strength of absorption features, black arrows illustrate the difference between the two features.

3.3.9 Shannon entropy

Originally, Shannon entropy has been used as a measurement of uncertainty in probability density distributions. In this study, spectral Shannon entropy (H_{spec}), as in the paper of van Ruitenbeek et al. (2020), is used as a measurement of chemical and spectral sorting during hydrothermal alteration of rocks. The Shannon entropy (H) of a probability distribution (P) is defined as:

$$H(p) = - \sum_{i=1}^m p_i * \log_2 p_i \quad (10)$$

With m as the number of possible outcomes and p_i the probability of outcome i .

Since Shannon entropy is a calculation of uncertainty in probability, the maximal value of 'H' would correspond with an equal chance of all probabilities. Minimum uncertainty is reached when the probability of a specific outcome is certain or 1. So a high Shannon entropy resembles high heterogeneity or randomness.

H_{spec} is also calculated with the equation above. However, it is interpreted as the uncertainty in wavelength of absorbed IR radiation. Flat horizontal spectra approach equal probabilities and produce higher entropies. The low spectral Shannon entropy is interpreted as the result of increased sorting of absorption features in the altered rock (van Ruitenbeek et al. 2020).

3.3.10 Decision trees

Multiple project-specific decision tree classifiers were designed using the ENVI software (see appendix 3). A decision tree classifier is a multistage classification method which uses a series of binary decisions to place pixels into classes. Each stage of the classification divides the pixels into two classes based on the response of a yes or no statement (expression). This will represent itself in a hierarchical tree-like structure of Boolean yes or no responses (Joseph 2015). The expressions used within this decision tree may relate to the wavelength position, relative depth of the absorption feature or other calculated ratios. Each expression, also called a parent node, has two daughter nodes; these can either form another parent node or output node. Output nodes are the end of branches and represent a particular classification. For this project, specific decision tree files will be combined within the same tree. Therefore, it will be possible to state expressions about different spectral ranges created during the wavelength position mapping or other spectral ratios. Using a Linux shell script, the needed files will be combined, and the decision tree will be run through the HypPy software.

For this project, a total of four decision trees were created. They use different classification methods, such as step-size and spectral parameters, to distinguish pixels based on their spectral profile. The outcome of these trees will provide information about the level of complexity necessary to obtain a clear image of the samples.

Strongest feature tree

The strongest feature based tree uses a step-wise increase of the strongest feature within the 2100-2400 nm range to determine its mineralogy. In addition, to further identify different mineral groups, the second strongest absorption feature within the 2100-2400 or the strongest feature within the 1300-1600 and that of the 1650-1850 nm are used.

Molecular bond tree

The molecular bond tree groups pixels based on the position of the strongest absorption features within the 2100-2400 nm range. These groups represent a more comprehensive wavelength range that corresponds with the absorption features of molecular bonds such as Al-OH, Fe-OH, Mg-OH and CO₃. As this generates multiple classes, secondary absorption features and parameters as 'Fe-drop' and 'illite over kaolinite' are implemented to further distinguish between pixels. A stepwise increase of the 'mixture ratio' was applied to accommodate for spectral mixtures within pixels.

Carbonate tree

The carbonate tree selects pixels of which the strongest or second strongest absorption feature lays within the 2310-2350 nm range. To eliminate phyllosilicate dominated pixels the 'mixture ratio' parameter was used. To further specify the carbonate minerals present in the samples the 'Fe-drop' and position of the feature at 2310-2350 nm were evaluated.

Multiple aspect tree

The multiple aspect tree is the most intensive tree of the four. It first subdivides the pixels on the strongest and second strongest absorption feature position within the 2100-2400 nm range. Categorises into three groups, carbonates, phyllosilicates or a mixture of the two. Then it uses the same strategy as the carbonates tree to evaluate them. For the phyllosilicates, it uses the 'illite over kaolinite', 'illite crystallinity' and 2200 nm position to categorise this group. The pixels determined to be a clear mixture of multiple signatures are categorised by 'mixture ratio', 'Fe-drop' and 'illite crystallinity'.

In summary, the acquisition of hyperspectral data will lead to multiple results. These datasets will be compared and validated to the data obtained by literature reviews and/or other analytical methods.

4 Results

This chapter will present the results obtained from the multitude of methods described in chapter 3.

4.1.1 Wavelength mapping

Wavelength map intervals were set at 1300-1600 nm, 1650-1850 nm, 1850-2100 nm, and 2100-2400 nm. Each interval calculated the three deepest absorption features for each pixel within those set ranges, providing information about the depth and position of a total of possible twelve absorption features. The following figures present the position (colour) and depth of the deepest feature (brightness) within each pixel. The samples are shown left to right according to depth, with background colour indicating stratigraphy.

NLW-GT-01

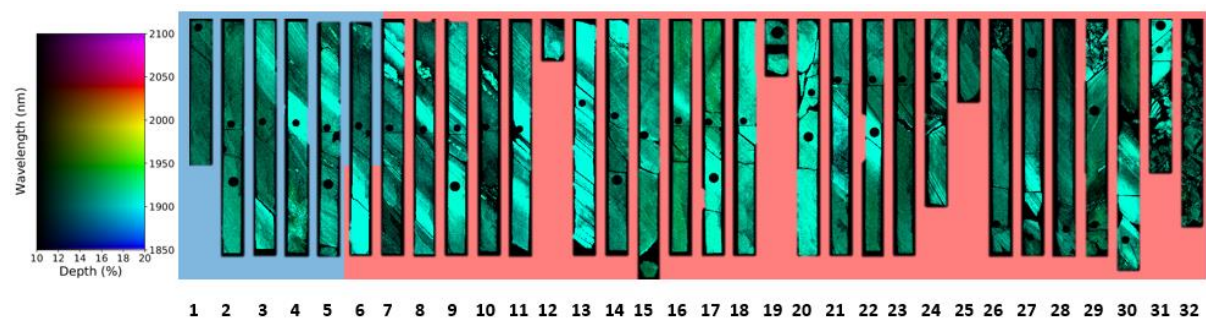


Figure 16: Wavelength map NLW-GT-01, 1850-2100 nm range. Background colours indicate; blue = Detfurth Sandstone, red = Volpriehausen Sandstone.

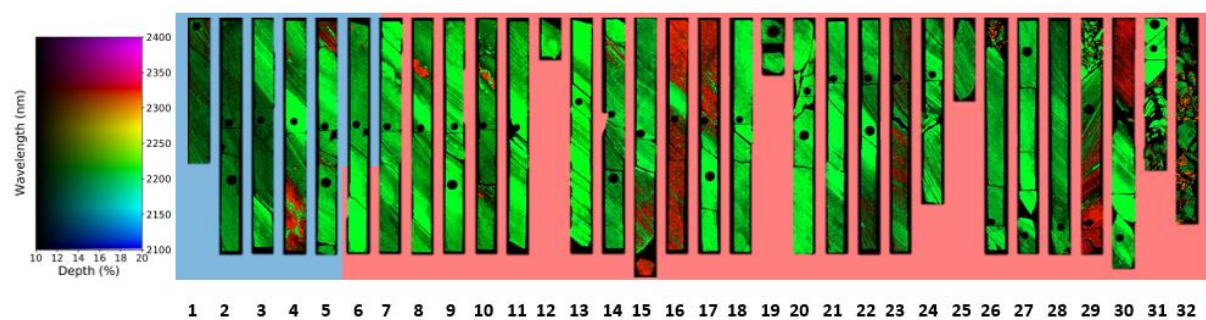


Figure 17: Wavelength map NLW-GT-01, 2100-2400 nm range. Background colours indicate; blue = Detfurth Sandstone, red = Volpriehausen Sandstone.

Within the 1300-1600 as well as the 1650-1850 nm range most parts of the NLW-GT-01 core lacks strongly present absorption features. However, at the 1400 nm range clear high intensity areas are detectable. They are of banded structure or as elongated tear shapes within the matrix. These high-intensity bands tend to occur at parts of the core with visible cracks. Within the 1850-2100 range a distinction can be made within absorption features, those that are sharply positioned near 1900 nm and those that are of a bit longer wavelength towards 1950. Depths at which a stronger 1400 nm feature was detected also indicate a very strong 1900 nm feature. At 4264 m and 4277 m (Figure 16, slabs 16/17 and 29/30) the position of the 1900 nm feature shifts towards 1920 nm; however surfaces

that showed intense 1400 nm features do not shift towards a longer wavelength and spike near 1900 nm.

Figure 17 illustrates the wavelength position of the deepest absorption feature within the 2100-2400 nm range of the electromagnetic spectrum. The main absorption features are observed near 2200 nm and 2340 nm. Within this figure four major distinctive groups can be recognised: (1) low intensity 2200 nm features (slab 2), (2) high intensity 2200 nm features (slab 13), (3) 2340 nm feature as elongated circular chapes surrounded by 2200 nm (slab 7) and (4) 2340 nm as whole rock matrix (slab 16). Within this colour difference, strong patterns of linear features at different angles can be noticed. An important distinction to make is that these elongated circular shapes do not have their strongest absorption feature at 1920 but 1900, in contrary to the matrix shown in slabs 16/17 and 29/30. Areas that showed a strong 1400 nm feature also indicate the presence of a strong 2200 nm feature.

BRTZ-01

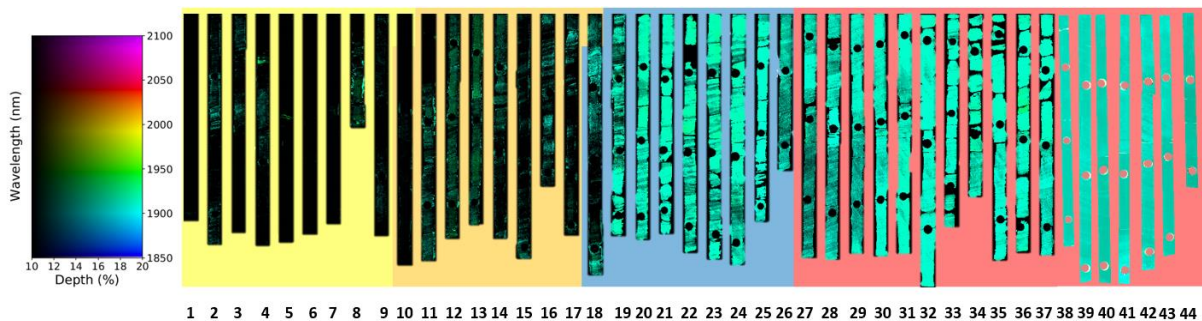


Figure 18: Wavelength map BRTZ-01, 1850-2100 nm range. Background colours indicate; yellow = Solling Claystone, orange = Solling Sandstone, blue = Detfurth Sandstone, red = Volpriehausen Sandstone.

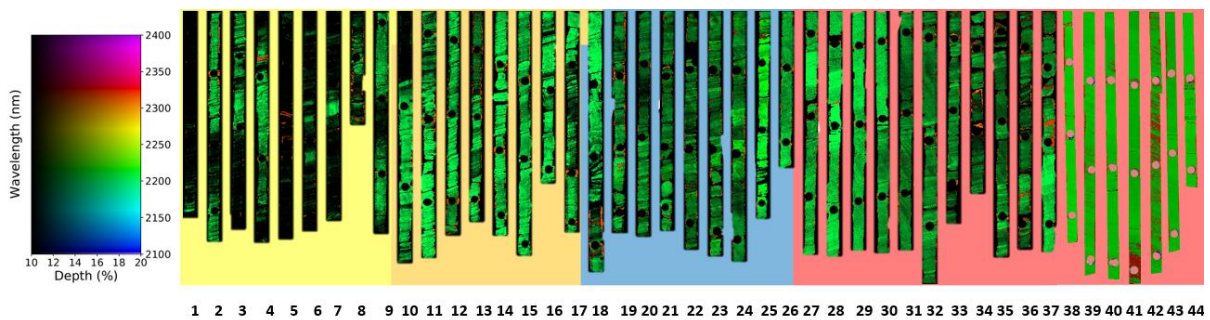


Figure 19: Wavelength map BRTZ-01, 2100-2400 nm range. Background colours indicate; yellow = Solling Claystone, orange = Solling Sandstone, blue = Detfurth Sandstone, red = Volpriehausen Sandstone.

As with the NLW-GT-01 core, the BRTZ-01 core has few strong absorption features within the 1300-1600 and the 1650-1850 nm range. One area has a 1400 nm feature that is considerably higher than all others, near 2774 m, surrounding the NAM 222 plug (slab 28). A distinct separation can be made within the 1850-2100 nm range, a distinct separation can be made. Slabs until 2761.85 m (Figure 18, slab 17), shows little to no strong absorption features. Beyond this point, the surface of the slabs shows stronger 1920 nm features. This shift aligns with the shift in lithology from the Solling Sandstone to the Detfurth Sandstone member. A second shift can be observed between the Detfurth Sandstone and the Volpriehausen Sandstone member. Within the Detfurth Sandstone the 1900 nm feature peaks near 1920 nm, while within the Volpriehausen Sandstone member this peak shifts to a lower wavelength.

Within the 2100-2400 nm range (Figure 19) there is a multitude of differences that can be observed. Slabs 1, 5, 6 and 7 show large surfaces without strong absorption features within this range. Slabs 4, 5, 25, 28 and 37 show small bands of which the strongest feature is positioned between 2300 nm and 2350 nm. A noticeable change in degree of the bands is observed in slab 18 (2762.5 m) underneath NAM plug 88.

4.1.2 Ferrous drop

The Ferrous drop represents the ratio between the 1600 nm and 1310 nm band. The calculated ferrous drop is then colourised using a decision tree. High values are represented by darker colours and thus representative of a more significant influence of Fe²⁺ bearing minerals.

Table 4: Ferrous drop mean and standard deviation, categorised on stratigraphy. The mean values are represented as a value between 1.0 and 1.5. Mean value; 1.0-1.1 = low, 1.1-1.2 = medium low, 1.2-1.3 = medium, 1.3-1.4 = medium high, 1.4-1.5 =high, >1.5 = very high.

Stratigraphy	NLW-GT-01		BRTZ-01	
	Mean	Std.	Mean	Std.
Solling Claystone			1.081	0.035
Solling Sandstone			1.133	0.052
Delfurth Sandstone	1.180	0.027	1.181	0.046
Volpriehausen Sandstone	1.185	0.049	1.169	0.026

NLW-GT-01

The overall mean value of the ferrous drop value for the NLW-GT-01 categorises as medium low. The standard deviation indicates that most pixels tend to stay close to the mean. However, exceptions are there, around 4275.3 meters (slab 29) the mean ferrous drop values spike up to 1.413, classified as 'ferrous high'. The very high values occur primarily in two forms. Firstly, that of very high ferrous speckled patterns within a medium to medium-low matrix. Secondly, bigger areas that seem to follow the dip angle of sand body deposition. Low ferrous drop values tend to occur as band-like structures also parallel to the dip angle of the bedding, see Figure 20. Inspection of the spectral profiles of these areas is illustrated in Figure 21. The low ferrous drop value shows the distinct profile of illite. While both high ferrous drop values show signs of absorption features at 1400, 1900, and 2200 nm a clear distinction is seen within 2330 nm hinting at the presence of carbonated, most likely dolomite.

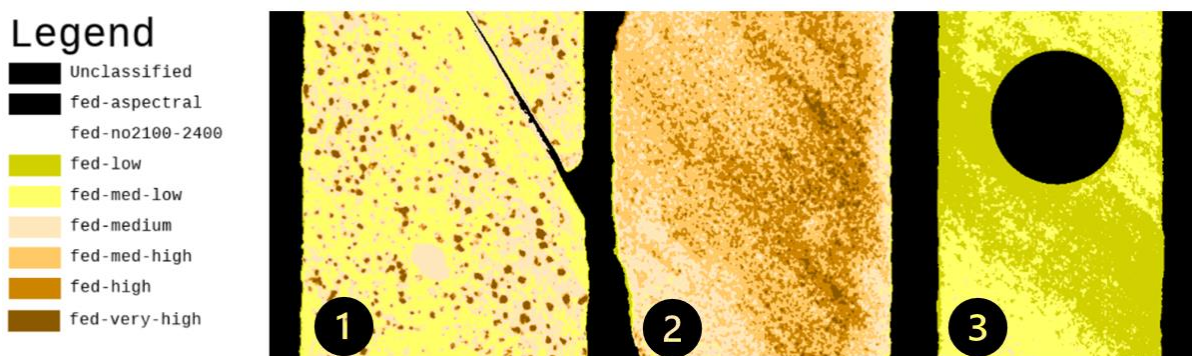


Figure 20: Ferrous drop, fed-low (<, 1.1], fed-med-low (1.1, 1.2], fed-medium (1.2, 1.3], fed-med-high (1.3, 1.4], fed-high (1.4, 1.5], fed-very-high (1.5, >). (1) speckled dots of very high ferrous drop values at 4253 m, (2) Bigger areas of high to very high ferrous drop values at 4277 m. (3) Area of low ferrous drop values as they are commonly seen throughout the core - 4265 m.

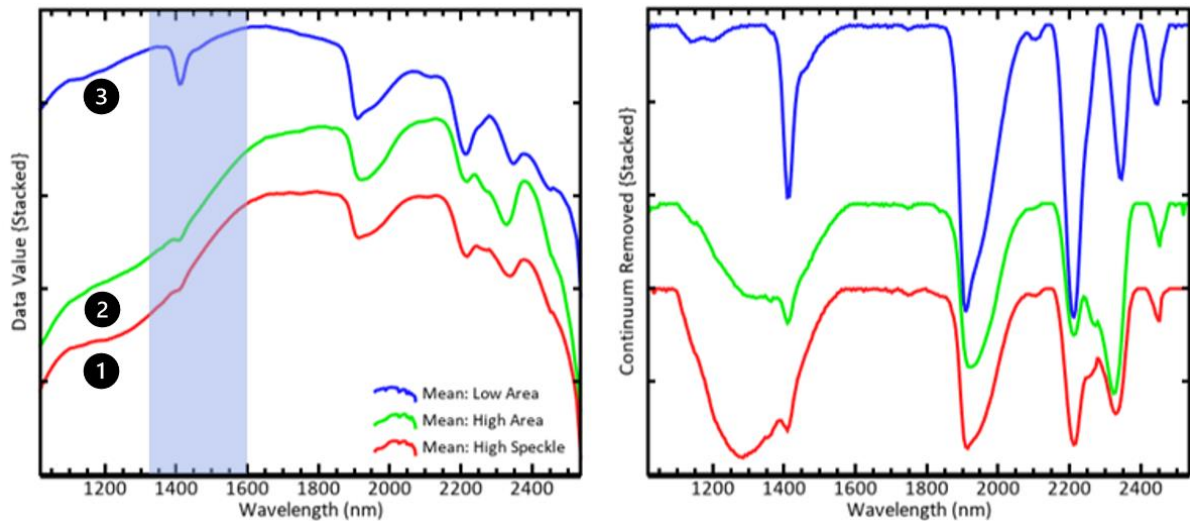


Figure 21: (A) Stacked spectral profile; the blue area indicates spectral region on which the Ferrous drop is calculated. (B) Stacked continuum removed spectral profile. Graphs are the mean value of ROIs originating from same areas as figure 20.

BRTZ-01

The overall mean value of the ferrous drop value for the BRTZ-01 is 1.148, categorising it as medium low. The standard deviation of 0.052 indicates that most pixels tend to stay close to the mean. Within the Solling Claystone and Sandstone member ferrous drop values are overall lower than within the Lower Detfurth Sandstone and Volpriehausen Sandstone Member. Until the top Delfurth Sandstone boundary at 2762 m, big areas of low ferrous drop values are highly continuous. Similar to the NLW-GT-01 core spotted patterns are visible. The bigger areas are less common, however banded structures of high value ferrous drop values are present. Very clear strong bands are present in the middle of the Detfurth Sandstone at 2765 meter, see Figure 22. Inspection of the spectral profiles of these areas is illustrated in figure 23. The low ferrous drop value shows the distinct profile of illite. However the blue lines also indicate to be illite yet with a higher influence of Fe^{2+} . Both profiles with high ferrous drop values show signs of absorption features at 1400, 1900, and 2200 nm. A clear distinction is seen within 2330 nm hinting at the presence of carbonated, most likely dolomite.

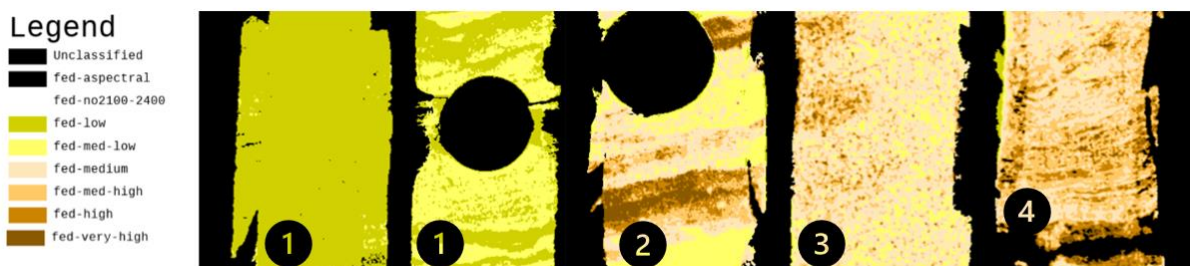


Figure 22: Ferrous drop BRTZ-01, fed-low (<, 1.1), fed-med-low (1.1, 1.2), fed-medium (1.2, 1.3), fed-med-high (1.3, 1.4), fed-high (1.4, 1.5), fed-very-high (1.5, >). (1) Uninterrupted areas of low ferrous drop values that can extend over multiple meters, 2751 m. (1) Banded structures of low ferrous drop values that flow the structure of the rock, NAM 231 – 2776.85 m. (2) Very strong ferrous drop bands, 2765 m. (3) spotted pattern of high ferrous drop values, 2769 m. (4) Banded structures of high ferrous drop values, 2768.5 m.

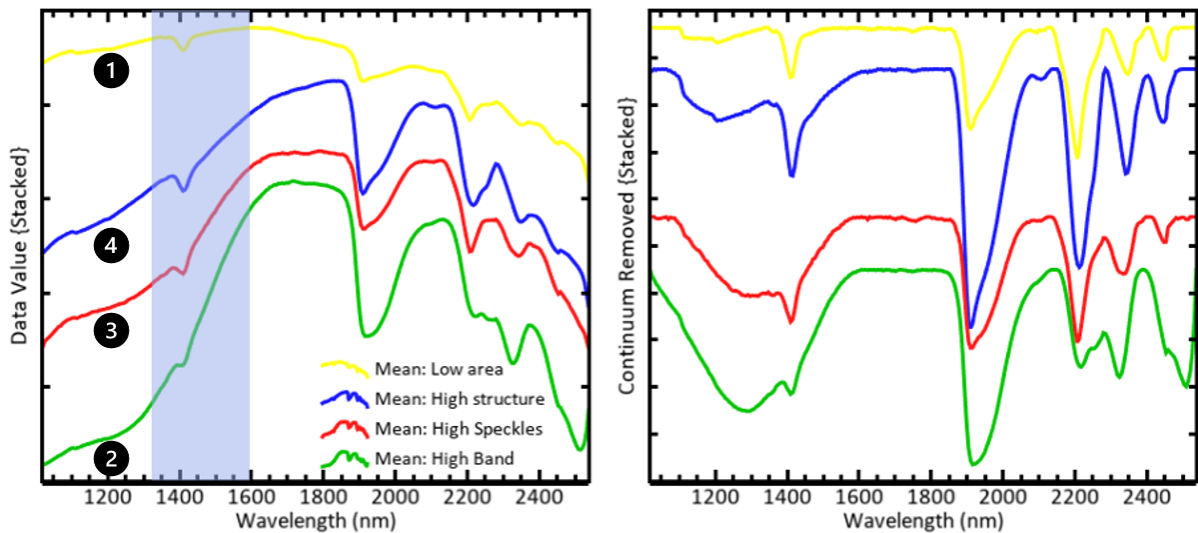


Figure 23: Stacked spectral profile, the blue area indicates spectral region on which the Ferrous drop is calculated. (B) Stacked continuum removed spectral profile. Graphs are the mean value of ROIs originating from same areas as figure 22.

4.1.3 Illite crystallinity

The Illite crystallinity value represents the ratio between the depth of the deepest feature within the 1850-2100 nm range divided by the depth of the deepest feature within the 2100-2400 nm range. The calculated illite crystallinity is then categorised using a decision tree. Four categories come forward within the samples from this classification: (1) no Al-OH bond, (2) smectite-illite, (3) illite-smectite, (4) illite. Their distribution is shown in Figure 24.

NLW-GT-01

The NLW-GT-01 slab is illite-smectite dominated (69.90 %). The Detfurth Sandstone is more smectite-illite dominated, and the Volpriehausen Sandstone is more Illite-smectite dominated. Areas with less to no AIOH bonds are present at depths of 4253, 4265, 4271 and 4277 meter.

BRTZ-01

The illite category is represented within the Solling Clay -and Sandstone Member. The Detfurth and Volpriehausen Sandstone are mainly smectite illite dominated. The boundary between the latter shows an alternating pattern at 2775 meters. The sloped edges of the slabs are categorised as no AIOH; this seems to be an artefact since these regions all have the same thing in common. They are inclined surfaces and thus not an even

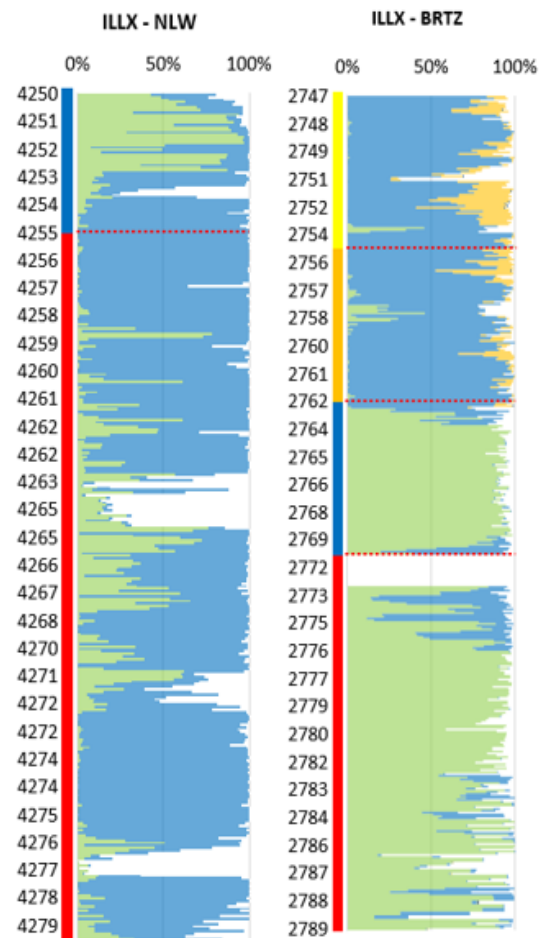


Figure 24: Stacked illite crystallinity of NLW-GT-01 and BRTZ-01 with depth and stratigraphy. The distribution is based on all spectral responsive pixels with a 9.6 cm interval. Green = smectite illite, blue = illite-smectite, yellow = illite, white or not filled indicates the absence of the AIOH bond. Sidebar colours indicate; yellow = Solling Claystone, orange = Solling Sandstone, blue = Detfurth Sandstone, red = Volpriehausen Sandstone.

surface perpendicular towards the camera's sensor. Therefore it may be responsible for a small increase compared to the actual value.

4.1.4 Illite over kaolinite

The Illite over kaolinite value represents the ratio between the value of the spectrum at 2164 nm divided by the value of the spectrum at 2180 nm. The calculated illite over kaolinite is then coloured using a decision tree. The 'absent AIOH' category indicates that the deepest feature within the 2100-2400 nm range is not present within the 2185-2225 nm range. If illite or kaolinite is present within the pixel, a high value would indicate a steep spectral slope that is indicative for illite, a low value would indicate the possible presence of kaolinite.

NLW-GT-01

The overall mean value of the illite over kaolinite value for the NLW-GT-01 is representative of a steep slope within the spectral signature. A clear indication of the absence of kaolinite. Most slabs show continued domination of this steep spectral slope. However, around the depths of 4251 m, 4259 m, 4269 m and 4277 m some the slope is less intense. The 'absent AIOH' bond present category is similar to the illite crystallinity. At the depth of 4276.7 m (Figure 25), an apparent change in dip angle and an increase in illite near a rock fracture can be observed.

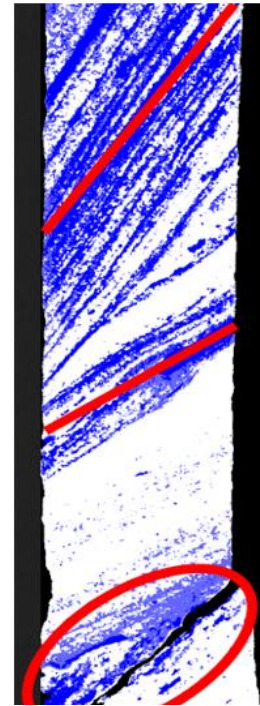


Figure 25: NLW-GT-01 (4276.7 m) blue indicates the steep slope associated with illite, white areas show the absence of a strong AIOH bond.

BRTZ-01

The overall mean value of the illite over kaolinite value for the BRTZ-01 is representative of a steep slope within the spectral signature. A clear indication of the absence of kaolinite. When comparing the mean values of each stratigraphy, this increase in value with depth is observed. Within the Volpriehausen Sandstone Member, sudden drops are measured at 2786.1 and 2788.7 meters. This region also shows more alteration and areas in which the no AIOH bond is present, see Figure 26. Inspection of pixels that indicate the presence of kaolinite illustrates the doublet profile at 2167 and 2206 nm, Figure 27.

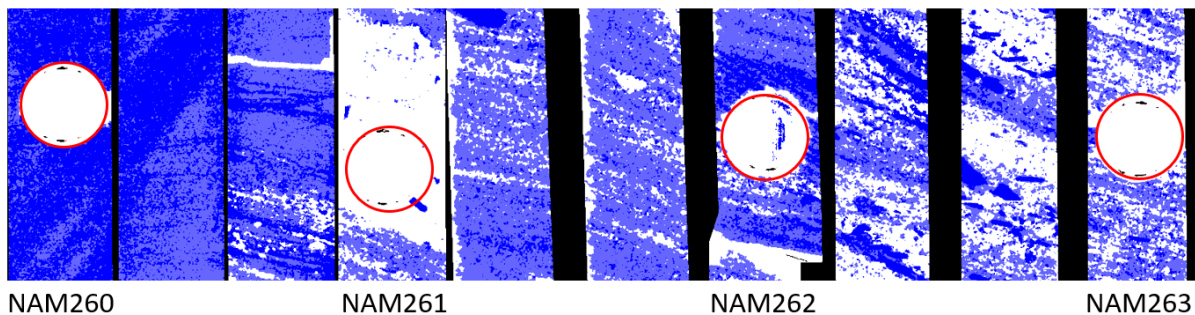


Figure 26: Illite over kaolinite, red circles indicate location NAM-plugs, NAM260 (2785.75 m) - NAM 263 (2786.64 m), images can be stacked for complete overview according to depth.

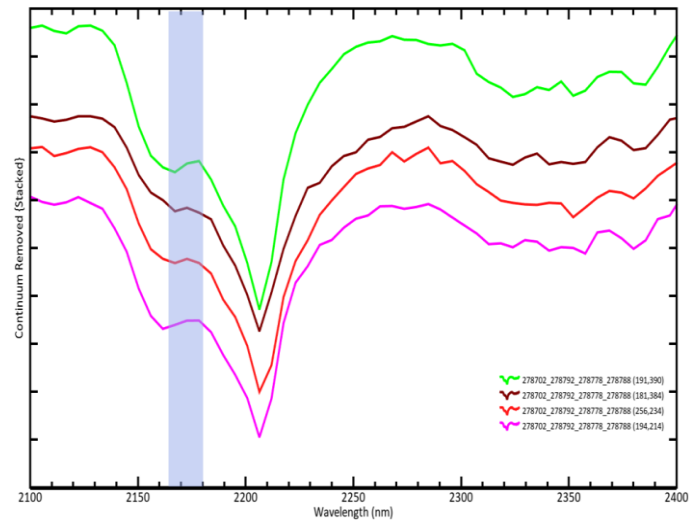


Figure 27: Stacked continuum removed spectral profile of pixels that indicate the presence of kaolinite based on the illite over kaolinite parameter at 2787.8 meter depth.

4.1.5 Position of 2200 nm feature

The change in position of the 2200 nm feature is used to evaluate the compositional changes within aluminosilicates (van Ruitenbeek et al. 2006). When the position of the absorption feature is below 2210 nm, it is interpreted as more muscovitic illite, while positions above are more that of phengitic illite (Kurt O. Kraal et al. 2021).

Table 5: Position of the 2200 nm feature mean and standard deviation, categorised on stratigraphy. The mean values are represented as a value between 2185 and 2225. Values below 2210 are muscovitic, and values above 2210 are phengitic.

Stratigraphy	NLW-GT-01		BRTZ-01	
	Mean	Std.	Mean	Std.
Solling Claystone			2206	0.710
Solling Sandstone			2206	0.096
Delfurth Sandstone	2212	0.901	2209	2.631
Volpriehausen Sandstone	2213	1.534	2208	1.103

NLW-GT-01

The overall mean position of the 2200 nm feature lies at 2212.6 nm for the NLW-GT-01 core, with the minimum and maximum values being 2210.4 and 2216.7 nm, thus always indicating more phengitic compositions.

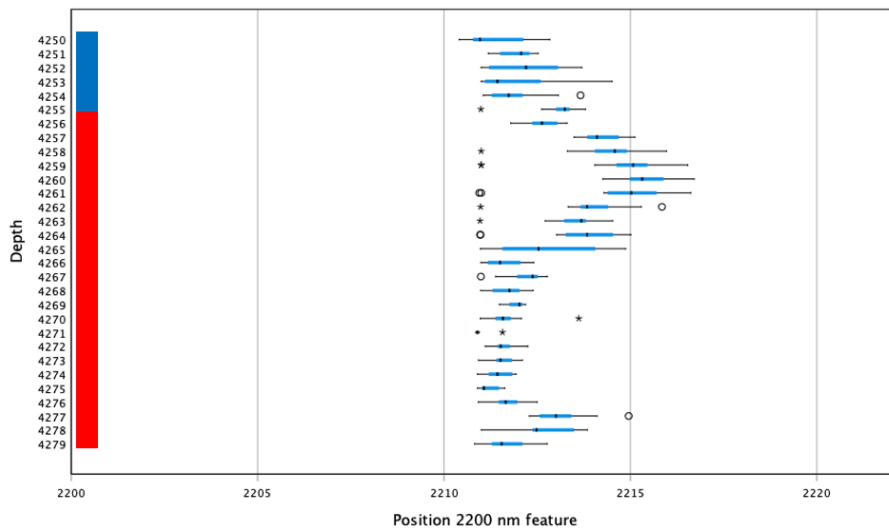


Figure 28: Boxplot of NLW-GT-01 illustrating the position of the 2200 nm feature with depth; mild outliers are marked by a circle (o), and far outliers are marked with an asterisk (*). This boxplot was generated based on the mean values of 9,6 cm intervals and presented with a 1-meter depth scale distribution. Sidebar colours indicate; blue = Detfurth Sandstone, red = Volpriehausen Sandstone.

As Figure 28 illustrates, an apparent increase of the 2200 nm feature starts at 4255 m, at the boundary between the Detfurth and Volpriehausen Sandstone members. At 4260 m the white mica is more most phengitic. It is during the interval of becoming more and less phengitic most outliers are seen. Another yet smaller increase and decrease is measured at 4277-4279 meters. At 4265 m, the first and third quartile and the whiskers are more widespread inferring a more widespread range of measurements. From 4269 m until 4275 m, the first and third quartile are close together, meaning the values are clustered more.

BRTZ-01

The overall mean position of the 2200 nm feature lies at 2207.5 nm for the NLW-GT-01 core, with the minimum and maximum values being 2205.0 and 2216.0 nm, thus indicating more muscovitic compositions throughout the core.

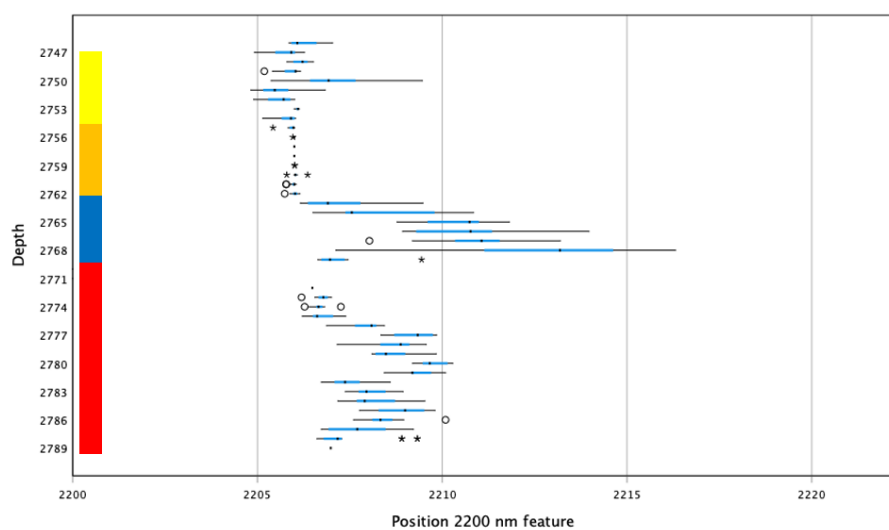


Figure 29: Boxplot of BRTZ-01 illustrating the position of the 2200 nm feature with depth; mild outliers are marked by a circle (o), and far outliers are marked with an asterisk (*). This boxplot was generated based on the mean values of 9,6 cm intervals and presented with a 1-meter depth scale distribution. Sidebar colours indicate; yellow = Solling Claystone, orange = Solling Sandstone, blue = Detfurth Sandstone, red = Volpriehausen Sandstone.

The BRTZ-01 core starts being relatively muscovitic within the Solling Clay -and Sandstone member, in which the Solling Sandstone member is very homogeneous. A shift towards more phengitic values occurs within the Detfurth part of the core, Figure 29. This shift abruptly ends at 2769 m. Within this region, the first and third quartile and the whiskers become more widespread and reach a mean value of 2212 nm. Between the depths of 2771-2780 m and 2783-2789 m, the position of the 2200 nm feature slowly rises in wavelength position, indicating a less muscovitic composition. However, it quickly resides back to more muscovitic composition at the end of the given intervals in both cases.

4.1.6 Strength of 1900 nm feature

The depth of the 1900 nm feature is used as an analogy for relative hydrous clay content. Relative higher hydrous clay content may indicate that fracture networks were more interconnected and/or permeable in the past, supporting hydrothermal fluid flow and water-rock interaction (Kurt O. Kraal et al. 2021).

Table 6: Depth of the 1900 nm feature mean and standard deviation, categorised on stratigraphy.

Stratigraphy	NLW-GT-01		BRTZ-01	
	Mean	Std.	Mean	Std.
Solling Claystone			7.4	2.053
Solling Sandstone			10.7	1.752
Delfurth Sandstone	14.5	2.145	19.1	4.378
Volpriehausen Sandstone	15.6	3.082	19.7	2.268

NLW-GT-01

The overall mean value of the 1900 nm feature is 15.37 for the NLW-GT-01 core, with the minimum and maximum values being 9.9 and 27.4.

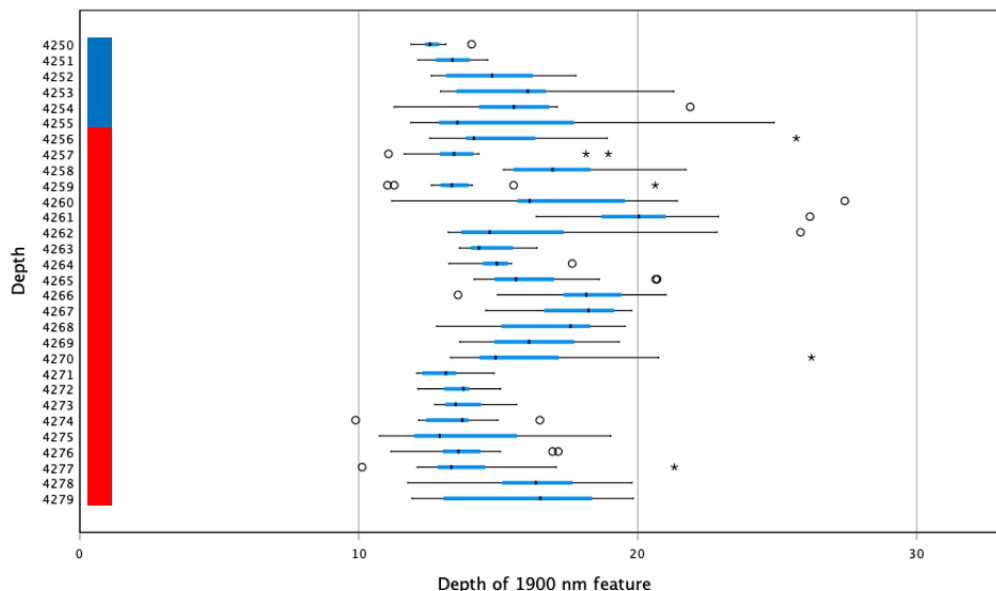


Figure 30: Boxplot of NLW-GT-01 illustrating the value of the 1900 nm feature with depth; mild outliers are marked by a circle (o), and far outliers are marked with an asterisk (*). This boxplot was generated based on the mean values of 9,6 cm intervals and presented with 1-meter depth scale distribution. Sidebar colours indicate; blue = Detfurth Sandstone, red = Volpriehausen Sandstone.

The strength of the 1900 nm feature sits primarily in between 10 and 20, with some whiskers and outliers expressing strengths above 20, Figure 30. Wide-spread boxplots are common, illustrative of the standard deviation of 2.97. While only considering the mean values of the box plots, an increase in strength of the 1900 nm feature is measured in the Detfurth Sandstone member. A sudden drop occurs at 4255 m, the vastly extended whisker indicates the sudden change from high values to lower values. A high volatile strength value is apparent from 4256-4262 meters, and ends with the highest mean value of 20.2 at 4261 m. A steep rise and shallow descent follow until 4271 meters. The far outlier can be linked to hotshot 7.

BRTZ-01

The overall mean value of the 1900 nm feature is 15.58 for the BRTZ-01 core, with the minimum and maximum values being 5.2 and 30.1.

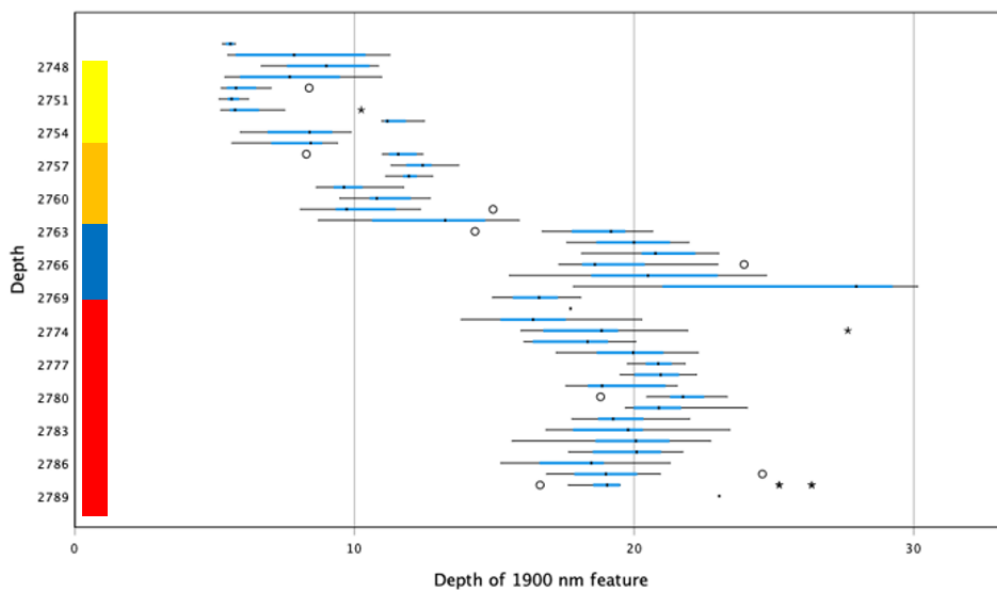


Figure 31: Boxplot of BRTZ-01 illustrating the value of the 1900 nm feature with depth; mild outliers are marked by a circle (o), and far outliers are marked with an asterisk (*). This boxplot was generated based on the mean values of 9,6 cm intervals and presented with a 1-meter depth scale distribution. Sidebar colours indicate; yellow = Solling Claystone, orange = Solling Sandstone, blue = Detfurth Sandstone, red = Volpriehausen Sandstone.

All the values below 10 are obtained in the Solling Clay -and Sandstone member, Figure 31. Within this range, two peaks occur at 2753 and 2758 m, closer inspection shows that the 2753 meter spike is an artefact of the inclined edges of the slab. The 2758 m spike might be exaggerated by the inclined edges; however, it is also seen on flat slab surfaces. At a depth of 2762 m, the boundary towards the top of the Detfurth Sandstone member the all-over strength of the 1900 nm feature increases severely and is followed by a steady incline for the following meters. This incline peaks at 2769 m after that the strength of the 1900 nm feature drops severely near the Detfurth Volpriehausen boundary. Within the Volpriehausen sandstone member, a pattern of rise and descent peaks at 2782m is seen from 2770 to 2789 m. The mean strength of the 1900 nm feature within the BRTZ-01 core is approximately 30 % stronger than those in the same stratigraphy of the NLW-GT-01 core. This is also observed in the higher colour intensity in Figure 18.

4.1.7 Shannon Entropy

The Spectral Shannon Entropy (H_{spec}) value expresses the amount of uncertainty within a probability distribution. Maximum uncertainty occurs when all possible outcomes have equal

probabilities. As the number of absorption features increases or the absorption features' strength becomes higher, the H_{spec} value will decrease. H_{spec} data is not available for BRTZ-01 from 2782.5-2789.0 m due to a processing error.

NLW-GT-01

Within the first 5 meters of the core, the level of entropy stays relatively uniform. A relative higher entropy value is measured at fractures as seen in Figure 32-A. However, surrounding areas of the fracture are seen to have lower values. The highest entropy values are measured between 4255-4261 m, the first 6 meters of the Volpriehausen Sandstone member (Figure 32-B). After that, Entropy values radically drop (Figure 32-C&D). In the following meters mid-level values are common, with some intervals of high values that continue over 10-20 cm. The spectral profile of categorised regions does not show a clear correlation between Shannon Entropy values and mineralogical composition (Figure 33).

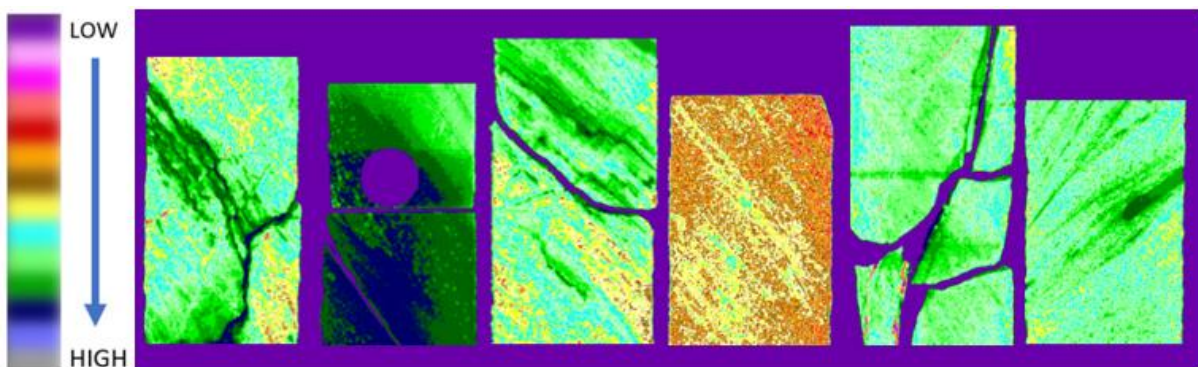


Figure 32: Shannon Entropy NLW-GT-01, close up from areas of interest, left to right: (A) 4253.5,(B) 4257.0 ,(C) 4261.6, (D) 4263.6,(E) 4266.8 and (F) 4276.7 meter.

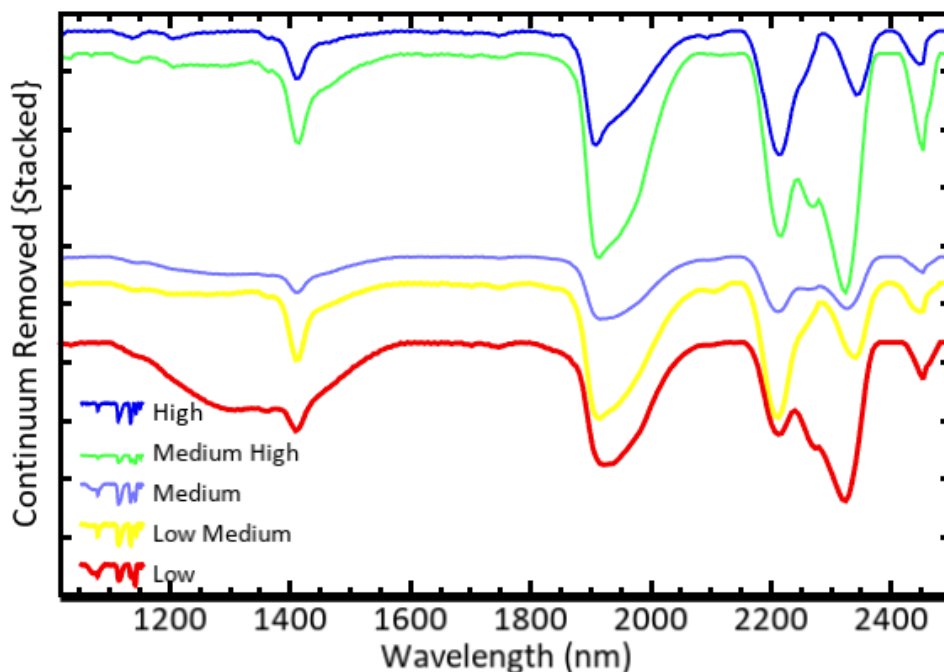


Figure 33: Stacked Continuum removed spectral profile of multiple Shannon Entropy zones taken from NLW-GT-01 core. Stacked in order from high (top) to low (bottom) Shannon Entropy values. Similar spectral profiles, such as 'High' / 'Low Medium' and 'Medium High' / 'Low' differ significantly in entropy values.

BRTZ-01

The Solling Claystone Member has high H_{spec} Values (Figure 34-A&B). Throughout the Solling Sandstone member, a steep decline and rise of the Entropy value are observed (Figure 34-B, C, D, E). Within this area, clear centimetre scale alteration can be distinguished. The Solling Sandstone and Detfurth Sandstone member boundary is characterised by a steep descent of the Entropy value. Throughout the Detfurth and Volpriehausen Sandstone members, the Entropy values stay low with some banded structures that reach medium level values (Figure 34-F).

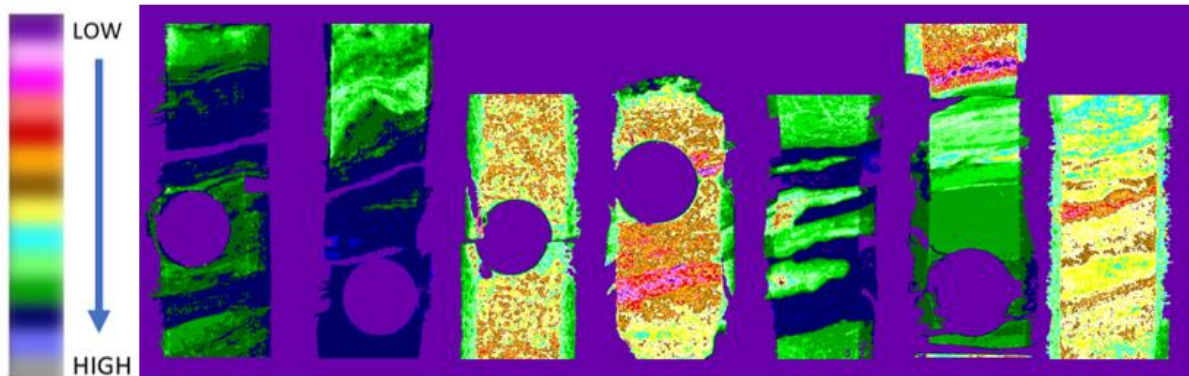


Figure 34: Shannon Entropy BRTZ-01, close up from areas of interest, left to right: (A) 2749.6 (NAM 149), (B) 2750.9 (NAM 153), (C) 2757.7 (NAM 173), (D) 2764.7 (NAM 196), (E) 2768.8, (F) 2773.6 (NAM 220), (G) 2781.5 meter.

4.1.7 Hyperspectral parameters – core overview

Appendix 4 illustrates the outcome of the above hyperspectral parameters throughout the entire core. Displaying the information in such a manner removes some of the details but provides a clear overview of the whole core.

4.1.8 Decision trees - mineralogy

The following section will provide summarised results of the project-specific decision trees compared to known mineralogy retrieved from literature, XRD values for BRTZ samples (NAM BV 2000) and microscopic thin section analyses for NLW samples (De Hoo 2021). These samples vary from 62 to 97 percent non-hydroxylated minerals such as quartz, feldspar and anhydrite. However, the decision trees outcome will provide a 100 percent surface coverage of spectral active minerals, e.g. phyllosilicates and carbonates. Therefore, the samples' mineral abundance of spectral active minerals will be normalised to be 100%. As a replacement for the absent BRTZ plugs the 9.6 cm subset of the slab from which the plug originated was used.

Table 7: Hyperspectral mineralogy per decision tree compared to actual and normalised mineralogy (De Hoo 2021; NAM BV 2000).

Borehole	Lithology	Sample	Depth (m)	Carb. Phyll.	Actual %	Normalised %	Deepest feature tree %	Molecular bond tree %	Carbonate tree %	Multiple aspect tree %
NLW-GT-01	Detfurth Sandstone	HO 01	4250.0	Carb.	14	75	19	80	80	72
				Phyll.	3	17	81	20	20	28
	Volpriehausen Sandstone	HO 11	4259.9	Carb.	7	18	0	0	0	0
				Phyll.	30	81	100	100	100	100
		HO 16	4265.0	Carb.	26	83	81	95	98	94
				Phyll.	5	16	19	5	2	6
		HO 25	4273.7	Carb.	12	55	0	25	20	22
				Phyll.	10	44	100	75	80	78
	HO 29	4277.7	Carb.	10	66	0	3	1	2	
			Phyll.	5	33	100	97	99	98	
BRTZ-01	Detfurth Sandstone	NM0193	2763.8	Carb.	1	33	8	36	15	33
				Phyll.	2	66	92	64	85	67
		NM0200	2765.9	Carb.	6	66	9	33	17	32
				Phyll.	3	33	91	66	83	68
	Volpriehausen Sandstone	NM0238	2779.0	Carb.	8	72	12	64	57	59
				Phyll.	3	27	88	35	43	41
		NM0243	2780.6	Carb.	5	27	9	29	18	32
				Phyll.	13	72	91	70	82	68
	NM0256	2784.5	Carb.	17	60	2	28	19	28	
			Phyll.	9	32	98	71	81	72	
	NM0267	2787.8	Carb.	24	72	0	20	12	18	
			Phyll.	9	27	100	79	88	82	

Deepest feature tree (DFT)

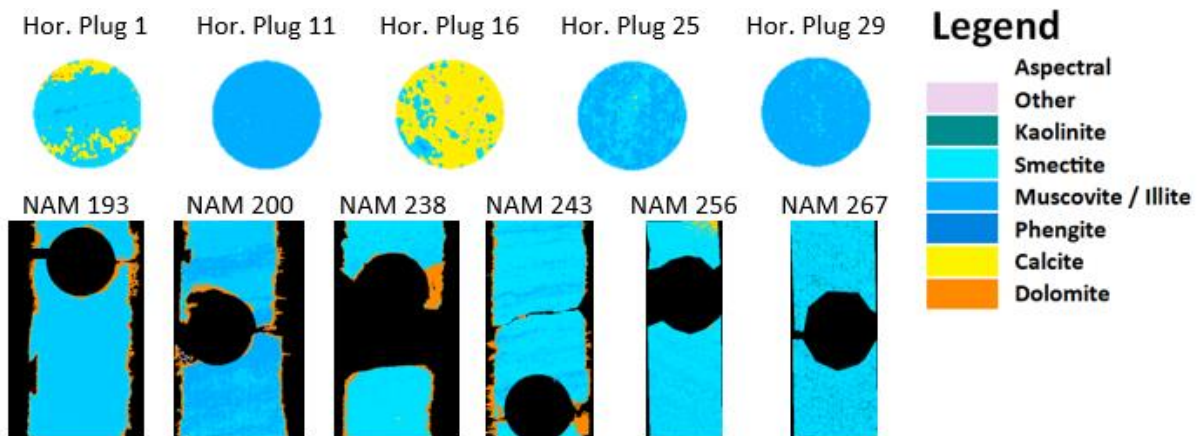


Figure 35: Mineral maps of indicated samples (table 7), produced by the Deepest feature tree.

The strongest feature based decision tree has identified the following minerals: kaolinite, smectite, muscovite/illite, phengite, calcite and dolomite. Within the BRTZ samples, carbonates are represented by dolomite. However closer inspection of the pixels near the edge that are presented to be dolomite indicates that very small proportions of resin is still present. As the resin creates a strong absorption feature near 2320 nm, this is falsely identified as dolomite.

As mentioned is the 2200 nm dominant over the 2330 nm feature within a mixture of both clays and carbonates. Since the strongest feature based decision tree does not account for the ratio, the outcome is strongly clay dominated. Plugs from NLW with a relatively high carbonate content indicate calcite's presence, as in those pixels the strongest feature lies at 2325 nm.

A well-defined difference between the two cores is that the pixels from the NLW plugs categorised as smectite and muscovite/illite are done within the 2210-2220 nm range, and the BRTZ samples within the 2200-2210 nm range. Although the 2200 nm position parameter is not represented in the decision tree, we do observe a more phengitic illite in the NLW plugs than in the BRTZ samples.

Molecular bond tree (MBT)

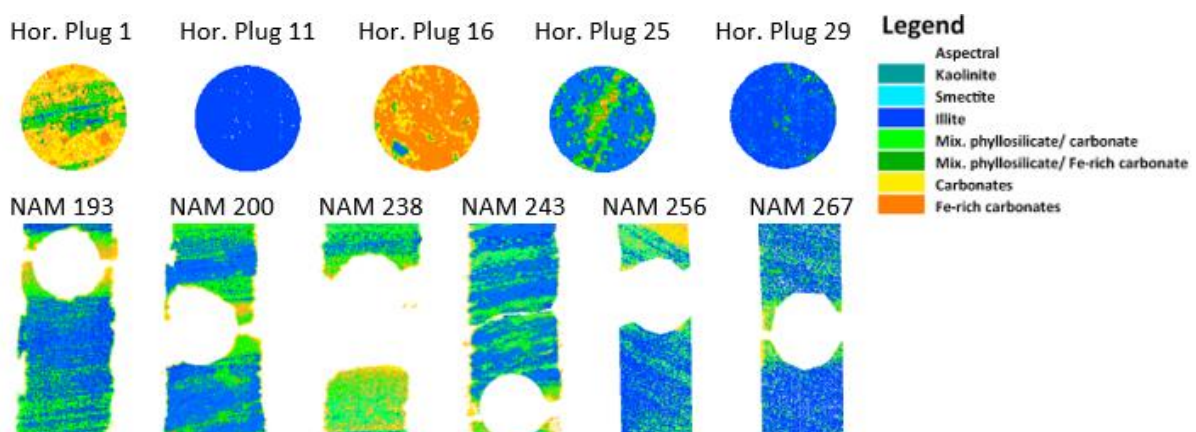


Figure 36: Mineral maps of indicated samples (table 7), produced by the Molecular bond tree.

The molecular bond based decision tree has identified the following minerals: kaolinite, smectite, illite, carbonates, Fe-rich carbonates, and mixtures of phyllosilicates with carbonates. These

mixtures are distributed as part carbonate part phyllosilicates dependent on their value within the mixture ratio parameter.

The spectrally identified carbonate content is higher than in the strongest feature decision tree. The by resin compromised pixels are properly discarded. Within the NLW plug samples a clear transition phase of the mix pixel signatures is seen between 'pure illite' and 'pure carbonate' pixels. Also it seems that Fe-rich carbonates tend to cluster within a matrix of carbonates.

Carbonate only tree (COT)

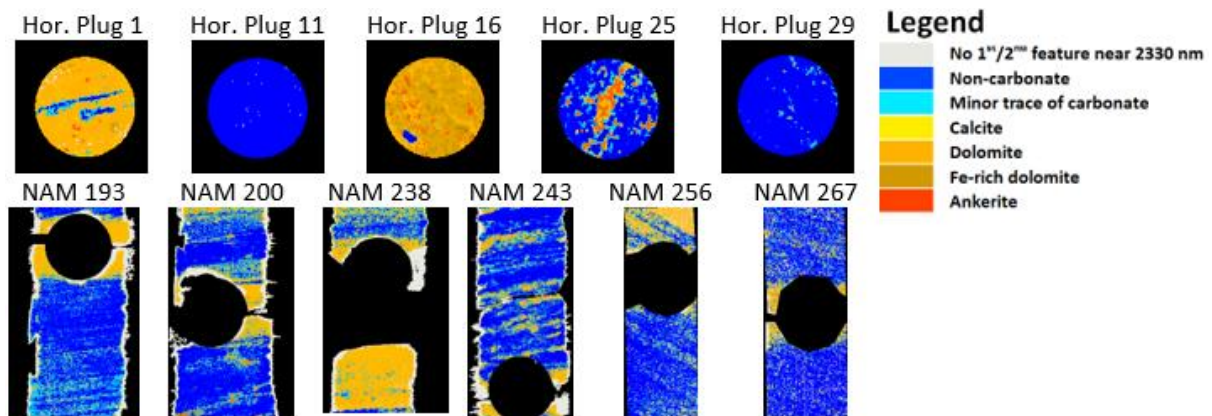


Figure 37: Mineral maps of indicated samples (table 7), produced by the Carbonate only tree.

The carbonate decision tree has identified the following minerals: non-carbonates, pixels with a neglectable amount of carbonates, Dolomite, Fe-rich dolomite and ankerite. Calcite was not observed within these samples.

NLW plug 16 and 25 have a composition in which Fe-rich carbonates are dominant over other carbonates. Within plug 16 this is mainly identified as Fe-rich dolomite while in plug 25 this is identified as of ankerite.

Multiple aspect tree (MAT)

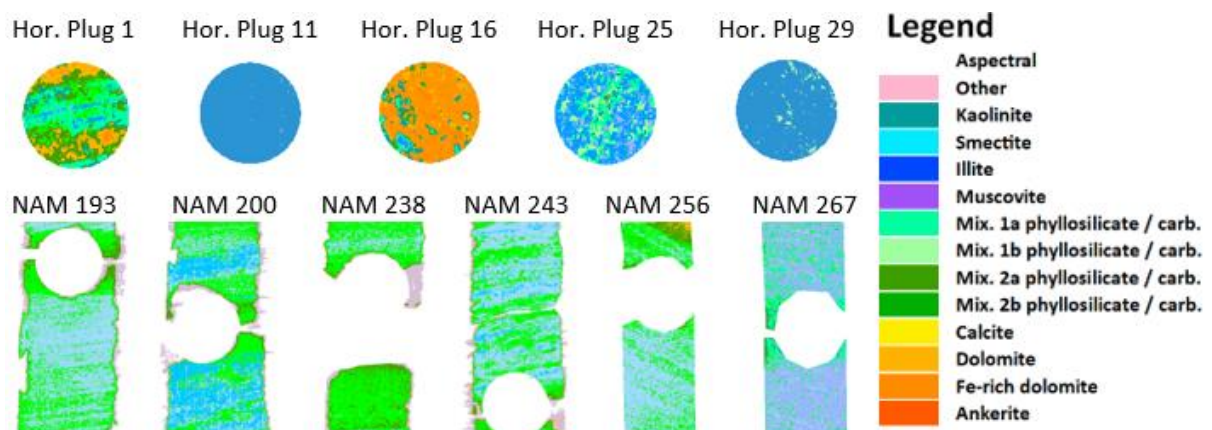


Figure 38: Mineral maps of indicated samples (table 7), produced by the Multiple aspect tree.

The multiple aspect decision tree has identified the following minerals: kaolinite, illite, dolomite, Fe-rich dolomite and mixtures, it also has made a distinction based on the position of the 2200 nm feature as well as illite crystallinity.

The carbonate content seems less noticeable as more pixels are identified as mixtures due to the strong absorption features at 1400, 1900, and 2200 nm. However the dark green colours of mixture 2 a/b represent strongly carbonate dominated pixels. The main mixture present in the BRTZ samples represents smectic illite with a low ferrous drop. While the mixtures in the NLW plugs are mainly of phengitic illite with a low ferrous drop, plug 25 is an exception as its mixture is mainly of phengitic illite with a high ferrous drop.

4.1.9 Decision trees – core overview

The previous section compared the outcome of the decision trees with known mineralogical data. It illustrated that different decision trees yield different results. The following section will provide the outcome of those similar decision trees over the entire cored interval, see Figure 40.

Deepest feature tree (DFT)

DFT presents the outcome of the DFT for both cores against depth and the corresponding porosity and permeability. NLW-GT-01 shows an alternating pattern between smectite and illite/muscovite dominated mineralogy with five depth intervals of high calcite content. At the bottom of the core, the presence of dolomite is indicated. However, this interval consists of many broken pieces of core. A review of the hyperspectral data of this interval shows that resin is present within these pixels providing a falls classification of dolomite as it alters the spectral profile.

The BRTZ-01 core shows fluctuations in the relative smectite content throughout the entire depth range of the core. Delfurth Sandstone member is characterised as mostly illite/muscovite dominated, while the Volpriehausen Sandstone member is strongly smectite dominated. Throughout the whole core, a small percentage of dolomite is detected, but inspection indicates that this is due to the resin rock interaction at the sloped edges of the slab. Areas, where actual dolomite is detected, are easily distinguishable as dolomite values are significantly higher, see Figure 39.

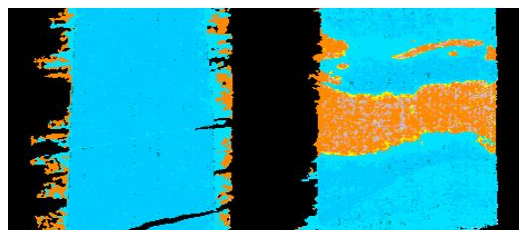


Figure 39: Source of Dolomite (orange) throughout the BRTZ-01 core.

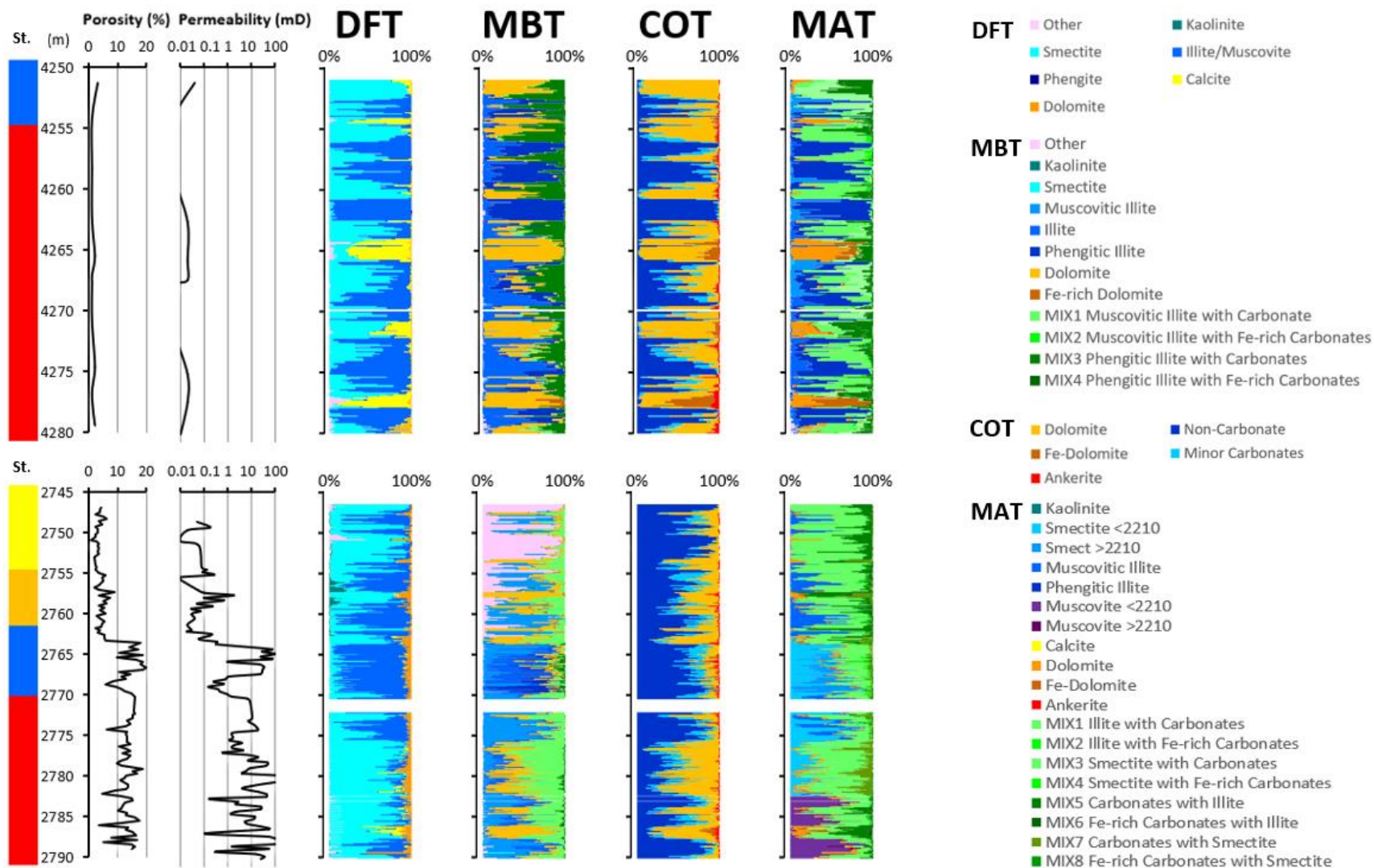


Figure 40: Porosity, permeability and output of the decision trees as a function of depth for the two cores, NLW-GT-01 (top) and BRTZ-01 (bottom). Stratigraphy (St.) colours indicate; yellow = Solling Claystone, orange = Solling Sandstone, blue = Detfurth Sandstone, red = Volpriehausen Sandstone. Abbreviations; DFT = Deepest feature tree, MBT = Molecular bond tree, COT = Carbonates only tree, MAT = Multiple aspect tree.

Molecular bond tree (MBT)

Figure 40 – MBT displays both cores as categorised by the MBT. According to this decision tree, NLW-GT-01 consists of four major components, 1) illite, 2) phengitic illite, 3) dolomite, and 4) a Fe-poor carbonate dominated mixture with phengitic illite. The boundary between the two lithologies at 4255 m is not directly visible to the naked eye. However, the classified image clearly shows the contact of the Delfurth Sandstone with the Volpriehausen Sandstone Member, see Figure 41.

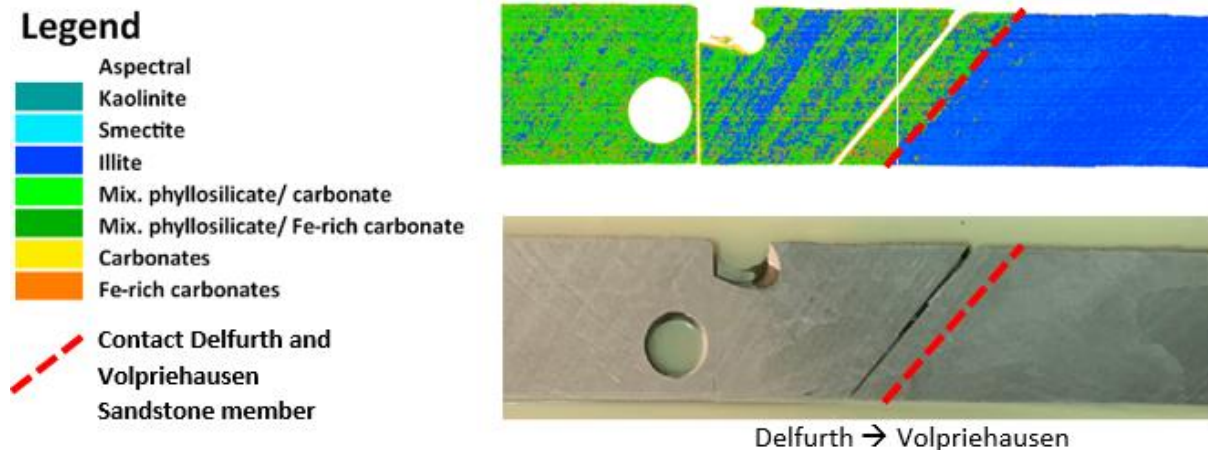


Figure 41: Contact boundary between Delfurth Sandstone Member and the Volpriehausen Sandstone Member at 4255 m. The bottom image is a true colour image, top image is the same interval classified by the molecular bond decision tree.

According to the mineral classification based on the molecular bond decision tree The BRTZ-01 core consists of seven major components: 1) those categorised as other, 2) kaolinite, 3) muscovitic illite, 4) illite, 5) phengitic illite, 6) dolomite and 7) muscovitic illite mixture with carbonate. The 'other' category mainly manifests itself within the Solling Claystone Member and is most likely illite tending towards phengite. However, it is not categorised since this area does not allow for strong absorption features to form. Within the Delfurth interval, the illite composition becomes more phengitic. Within the first meters of the Volpriehausen Sandstone this becomes more muscovitic illite again. Based on the 'mixture ratio' parameter we can conclude that mixtures in the BRTZ-01 core are not as carbonate dominated as in the NLW-GT-01 core.

Carbonate only tree (COT)

Figure 40 – COT provides a clear understanding of the length of carbonate intervals and their composition. The NLW-GT-01 core has intervals up to 2 meters long without carbonates. Comparisons between the mineralogical data and the 'mixture ratio' parameter have shown that it is possible at lower carbonate contents that the spectral profile is completely suppressed by that of phyllosilicates. Inspection of the non-carbonate intervals shows little to no interference at other wavelengths than the characteristic absorption features for illite, Figure 42. These intervals correlate with the 2100-2400 nm wavelength map bright green areas. The spectral profile of dolomite obtained from the sample does show influences of the illite spectrum.

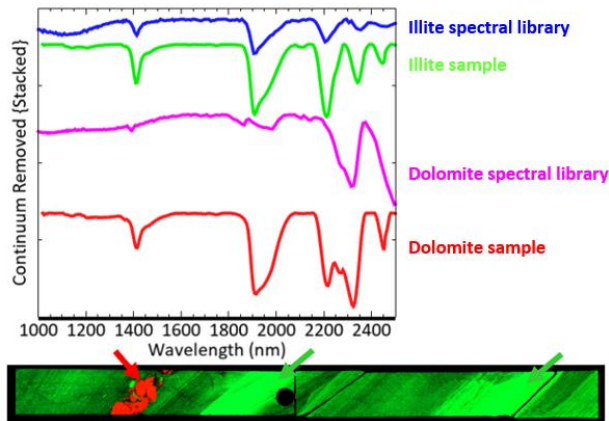


Figure 42: Spectral profiles of illite and dolomite obtained from indicated locations at the slab (NLW-GT-01, 4257 m) and the spectral library (Kokaly et al. 2017). Illustration of the slab is in the form of the 2100-2400 nm wavelength map; green indicates the deepest absorption feature is at 2210 nm and red indicates the deepest absorption feature near 2330 nm. The spectral profile of illite (green) resembles that of the spectral library (blue). The dolomite spectral profile (red) clearly shows overprinting of the illite spectrum in its profile.

The BRTZ-01 core also shows fluctuations in carbonate content. However, according to the decision trees, it does not seem to have considerable intervals that are completely carbonate free. At the same time, there are almost no examples of the relative carbonate contents exceeding 80%, whereas the NLW-GT-01 core has multiple samples of >95% carbonates. The primary carbonate source is non-ferrous dolomite with a small amount of Fe-rich carbonates. The Volpriehausen Sandstone Member has a higher carbonate content than the Detfurth Sandstone Member. Within the BRTZ-01 core, there seems to be a trend that the permeability is relatively low if carbonate content is high.

Multiple aspect tree (MAT)

Figure 40 – MAT, according to this decision tree, the NLW-GT-01 core mainly consists of the following categories: 1) smectite, 2) phengitic Illite, 3) dolomite, 4) Fe-rich dolomite, 5) a smectite dominated mix with carbonate, 6) a carbonate dominated mix with illite and last 7) a carbonate dominated mix with smectite. Throughout the core, phengitic illite is the most dominant mineral. At 4265 and 4278 m, dolomite becomes the more dominant mineral.

The BRTZ-01 core mainly consists of the following categories: 1) smectite, 2) multiple forms of illite, 3) muscovite, 4) dolomite, 5) an illite and smectite dominant mixture with carbonate, 6) a carbonate dominated mixture with illite, and 7) some traces of kaolinite. Kaolinite and muscovite are only observed towards the bottom of the core; kaolinite detection in this area agrees with the XRD values (Felder and Fernandez 2018). The transition of the Solling Sandstone Member towards the Detfurth Sandstone member is emphasised by the transition of muscovitic illite towards smectite.

5 Discussion

This study aimed to investigate whether correlations between the hyperspectral data from short-wave infrared spectroscopy and the physical rock parameters such as porosity, permeability and mineralogical composition can be established. A case study was completed on cored intervals of the NLW-GT-01 and BRTZ-01 drilling cores. This chapter will provide a complete overview of the obtained data and emphasise important trends that can be observed and what cannot be observed. Afterwards, the findings will be put in a broader context of the literature and suggestions for future research.

5.1 Data accusation

SWIR spectroscopy has proven to be a very fast method of obtaining data from cored rocks. Unprocessed hyperspectral images were obtained at a rate of approximately one meter per five minutes. Improvements could easily be implemented to increase scanning rates if such a workflow is desired. When considering this method, one must also consider the data infrastructure in place, as this study produced over 1 terabyte of data.

Decision trees

For this study, four project-specific decision trees were created. The deepest feature decision tree could not correctly determine the amount of carbonates within the samples due to the high absorption coefficients of phyllosilicates. Implementing the 'mixture ratio' within the other decision trees provided better representation within mixed spectral profiles. Of all the decision trees, the multiple aspect tree provided the most data within a pixel. However, simplified trees could be helpful as they are easier to interpret and need less computational power.

5.2. Hyperspectral parameters

This section will provide a summarised overview of the hyperspectral parameters measured within this research. To avoid circular reasoning, some parameters (e.g. Illite crystallinity, ferrous drop) will not be directly compared with the outcome of the decision trees as they are part of the decision-making system.

Position absorption features

The primary identification tool within this research is the position of hyperspectral absorption features. As absorption features tend to shift due to compositional/chemical changes. The 2200 nm feature has been described in the literature to differentiate between muscovite illite and phengitic illite compositions (Garcia 2013). This study has found that the NLW-GT-01 core shows some variation but always stays above 2210 nm, indicating a phengitic illite composition. The wavelength position of the BRTZ-01 core exceeds this boundary within the Detfurth Sandstone Member and has values below 2210 nm throughout the Volpriehausen Sandstone Member. However, the chemical compositions of illite can be influenced by many factors, as described by Meunier (2004).

The position of the 1900 nm feature in kaolin, illite-muscovite and smectites groups all have a relatively sharp 1900 nm feature, usually around 1910 nm (Laukamp 2011; Pontual et al. 1997). Absorption features measured towards a higher wavelength position were less sharp and primarily identified as carbonate-rich intervals.

Illite crystallinity

Normally illite crystallinity is defined by the Kübler Index obtained through XRD measurements (Kübler et al. 2001). The spectral illite crystallinity is a proxy as it is not a measurement of crystallite sizes but instead describes other processes during the evolutionary sequence (Doublier, Roache, and

Potel 2010). As Doublier et al. (2010) has indicated a significant quantitative relationship exists between the spectral illite crystallinity measured within this research and the illite crystallinity normally obtained from XRD. Thus providing a valuable method for measuring changes in metamorphic grade. Higher illite crystallinity values within this MSc thesis were detected in the NLW-GT-01 lithologies than in similar lithologies of the BRTZ-01 core. These findings correspond with expected reasoning as the NLW intervals lay at greater depths and have a higher average temperature than the BRTZ core (Mijnlieff 2020). Throughout the NLW core a high illite crystallinity value is maintained except for some lower dips; these dips can be linked to areas of high carbonate content. This is logical considering the mixture ratio, where it was observed that regions of mixtures with high carbonate content express less deep 2200 nm features. The low illite crystallinity values of the BRTZ core correspond to high permeability intervals.

Illite over kaolinite

The illite over kaolinite parameter successfully detected 66 % of the cases in which kaolinite was known to be present due to earlier XRD measurements. The sample in which this parameter failed to indicate the presence of kaolinite was sample NAM243 (2780.6 m). This sample had an illite concentration of 12 % and a kaolinite percentage of 1 %; other samples both had 3 % kaolinite and 6 % illite (Van Bergen et al. 2008). Kaolinite can thus be detected when it is present in low abundances; however, high concentrations of illite can overprint the doublet feature of kaolinite.

Ferrous drop

The ferrous drop used in this research can be seen as a hyperspectral proxy. It is not the absorption feature measured but the influence the Fe^{2+} imposes at higher wavelength positions. It proved helpful in distinguishing (non) iron-bearing minerals from their equivalents. High peaks of ferrous drop values were observed within the NLW-GT-01 core. Inspection of the hyperspectral profiles indicated these were caused by ferrous-rich dolomites. This corresponds with the known ferroan dolomitisation described by multiple studies (e.g. Ursem 2018; De Hoo 2021; Maniar 2019).

Detection of carbonates

According to De Hoo (2021) NLW sample 'horizontal plug 11' (4260 m) contains 60.3 % quartz, 30.2 % clays and 6.7 % carbonates. However, all decision trees indicate a 100% non-carbonate composition. The region interval near-horizontal plug 11 (4258-4261 m) shows fluctuations in carbonate content and the smallest measured average grain size throughout the NLW core (46 μm , De Hoo 2021). Inspection of the hyperspectral data of this interval and the available thin sections (Figure 43) indicate the following; in regions of high clay concentration that have grain sizes significantly lower than the pixel size (256 μm), carbonates percentages below 7% are not detected. Although it was known for clay to dominate a spectral profile, these findings show that critical diagenetic processes, such as carbonate cementation, may go unnoticed in specific cases. Increasing the resolution by lowering the pixel size to 26 μm might solve this problem. However, this would exponentially increase the data produced during hyperspectral imaging. Besides that, the amount of samples suitable for scanning would significantly drop as they would not spatially fit under the high-resolution camera set-up.

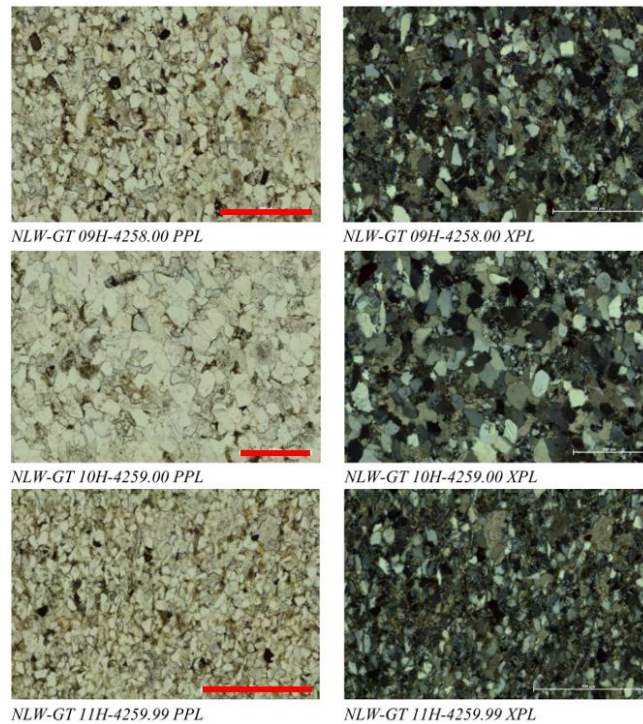


Figure 43: Thin sections of the NLW-GT-01 core at 4258 (09H), 4259 (10H) and 4260 and (11H) meters depth, the red line indicates 500 μm (scalebar as used by De Hoo, 2021). Thin sections 09H and 11H both have a high clay content and a proportionally smaller grain size than 10H.

Effect of albedo on Shannon entropy

The albedo value of an object is important while measuring the amount of reflected light. As the surface of an object has a high albedo value, high amounts of light are reflected from its surface. Therefore as specific wavelengths get absorbed the value of its absorption feature has a high contrast to nearby wavelength positions. Consequently, the depth profile of the 1400 nm feature is similar to that of the 1900 nm feature. However, since the albedo value affects both features, relative values should still be suitable for different practices.

The albedo value also has a noticeable effect on the Shannon entropy calculations. Appendix 4 Entropy (8) and Albedo (9) show a clear mirrored pattern. As albedo values are low, the Shannon entropy value is relatively high. Since high entropy values occur when all values have the same probability, or in other words, when there are no apparent absorption features, as albedo values rise, absorbed wavelength regions can create relatively deeper absorption features, therefore changing the probability of each value to be equal, lowering the Shannon entropy.

5.3 Data comparison

The ultimate goal of this research was to investigate whether correlations between the hyperspectral data and physical rock parameters could be established. This section will provide an interpretation of the reviewed data and will compare that to descriptions given by other research.

Mineralogical

Similar minerals were generally observed in XRD, petrographic microscope, and hyperspectral imaging. The inability to detect minerals that do not have a spectral response within the SWIR-spectrum (e.g. quartz, feldspar and anhydrite), left this research unable to estimate the actual volume percent of all mineral constituents within the sample, which XRD and thin sectional research were

able to do. However, with the methods described, this research was able to generate relative mineral abundance information. Although we speak of non-quantitative results, they are still helpful in interpreting mineralogical changes. Also, it was possible to detect changes in spectral profiles or proxies that provide an enhanced understanding of mineral chemistry. Furthermore, this method distinguished clay minerals that would not be distinguishable with petrography.

Textural

Another advantage of this method is the spatially continuous dataset it produces. This allows for mineralogical investigation with more considerable spatial coverage than usually applied with other methods. The study of Maniar (2019) has described the NLW-GT-01 core extensively and provided a sedimentological log with interpreted lithofacies. She described four main lithofacies associations within the NLW-GT-01 core, a mud dominated facies and three types of sand dominated facies. Although the hyperspectral data could not distinguish grain sizes, the facies associations could be easily recognised using the categorised hyperspectral images in which features such as changes in dip angle, truncation crossbedding and clasts were highlighted. The application of this method would thus be a helpful tool during core logging. It should be said that some hyperspectral images were better suited for this than others. As decision trees that are simplistic in their classification, some details could be lost, see Figure 44.

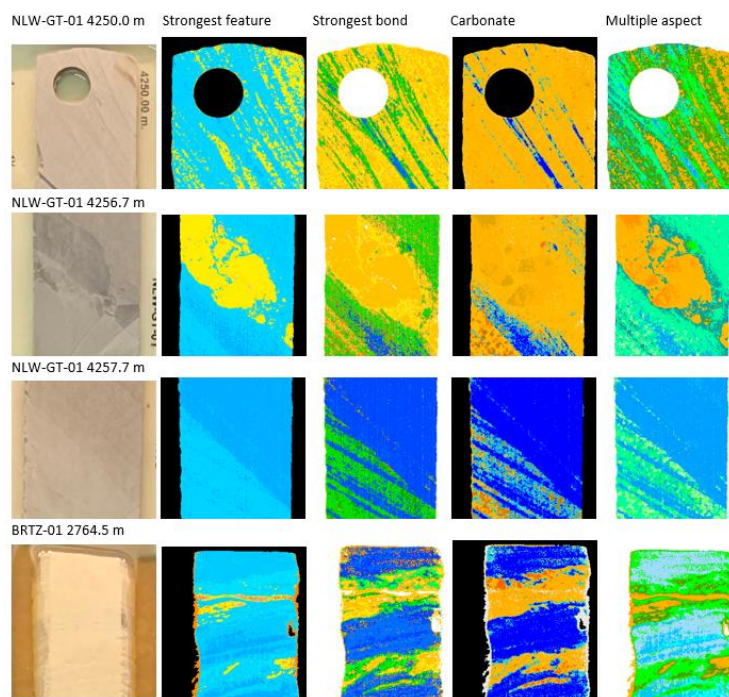


Figure 44: Comparison of hyperspectral images generated by project-specific decision trees and textural features.

Porosity and permeability

As explained in chapter 2.3 the most important properties for reservoir quality are porosity and permeability. However, reservoir quality prediction is not as straightforward since many factors influence it.

With the current methodology and dataset, the hyperspectral data could not provide a quantification to indicate porosity and/or permeability. However, the main driving mechanisms for porosity loss in the NLW-GT-01 core described by De Hoo (2021), mechanical compaction due to

burial, intergranular pressure solution, and carbonate cementation can partly be described supported by the hyperspectral data.

The relative mineral content of carbonates is frequently higher within the NLW-GT-01 core than in the BRTZ-01 core. Only counting the Delfurth and Volpriehausen Sandstone members, we observe that over 9,6 cm intervals, the NLW core (total length = 30 meters) have a total of 91 intervals with a carbonate content of > 75 %, of which 40 are above 95 %. While the BRTZ-01 core (total length = 28 meters) only has 14 cases >75 %, of which 0 are above 95 %. This advocates that the NLW core is more heavily cemented due to carbonate cementation than the BRTZ core. Which is a pore filling process that contributes significantly to porosity loss, according to De Hoo (2021).

The process of porosity loss from mechanical compaction due to burial is more difficult to correlate with the hyperspectral data directly. However, the reported illite crystallinity values indicated that the phyllosilicates within the NLW core are more mature than those in the BRTZ core. Secondly, the observation of kaolinite in the BRTZ core and its absence in the NLW core; as kaolinite becomes unstable at relatively low temperatures, it might reflect overall temperatures differences within this region. Both observations support the idea that the NLW-GT-01 core has a higher metamorphic zone than the BRTZ-01 core (Bjørlykke 2015; Meunier et al. 2004; Simpson 2018). In addition, it is essential to mention that the abundance of clay and its ductility may be another factor for porosity loss. As burial increased and rigid grains underwent diagenetic processes, the ductile clays could have been squeezed between the rotating grains, filling up pore space. This effect might have been of more significant influence within the NLW-GT-01 core as more compaction occurred.

As quartz is a non-hydroxylated mineral, it is not detected using SWIR spectroscopy. Therefore, a clear assessment of the intergranular pressure solution is also impossible.

5.4. Limitations

The use of SWIR-spectroscopy has its limitations, like all mineralogical analytical methods. The most significant limitation is the inability to detect spectrally inactive minerals (e.g. quartz, feldspar, anhydrite) within the wavelengths that SWIR-spectroscopy operates. This inability leads to mineral overestimation as the mineral behind the spectrally inactive mineral do provide a spectral absorption feature that will be detected, Figure 45-D.

In spectral mixtures, it can be challenging to unmix the spectra. Minerals with high absorption coefficients (e.g. clays) can be dominant over minerals with low absorption coefficients (e.g. carbonates). This may lead to underestimating certain minerals within a sample, Figure 45-B. An excellent example of this is the absence of carbonate within all decision trees for NLW-GT-01 horizontal plug 11, while earlier research indicated a 6.7% carbonate content within this sample.

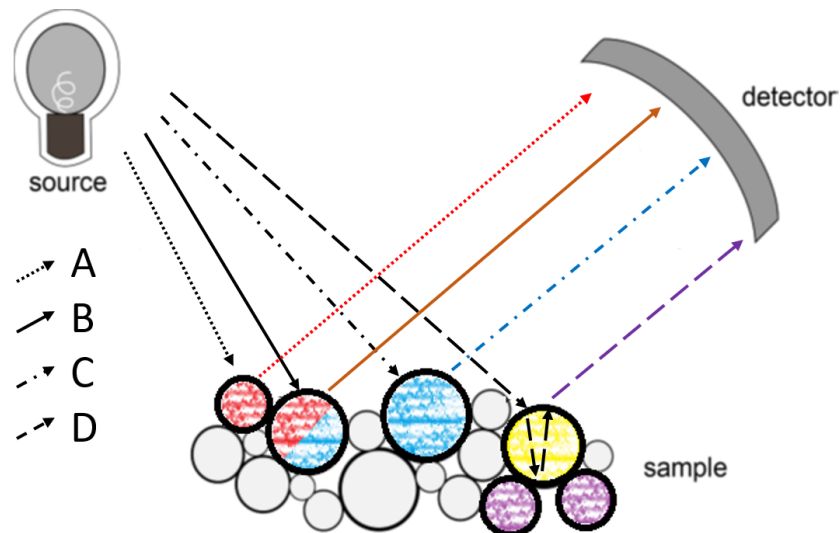


Figure 45: Illustration of mineral detection and mineral overestimation; the circle's colour indicates mineral x , where red has a higher absorption coefficient than 'blue' and yellow is spectrally inactive. A) Detection of the spectral profile of the 'red' mineral, B) Detection of a spectral mixture; due to the higher absorption coefficient of the 'red' mineral, the light that reaches the detector mainly consists of a spectral profile matching to that of the 'red' mineral, signals of the 'blue' mineral may be present, C) detection of the 'blue' mineral, D) Detection of the 'purple' mineral since the 'yellow' mineral is spectrally inactive.

Another important note should be placed on the technical aspect of parabola fitting used to produce the wavelength maps. This method only recognises absorption features at their vertex; when an absorption feature is affected by a stronger absorption feature nearby, it might not be able to form a complete vertex (e.g. the doublet feature of kaolinite in a mixed profile with illite). In such cases, the method of parabola fitting will not detect the absorption feature, while its presence may still be detected in the spectral profile. Another problem arises when a double vertex is observed within the spectral signature due to the spectral band distribution. In such cases, one absorption feature is registered as two features. This might result in false mineral identification when using decision trees. However, spectral inspection easily detects such mistakes.

5.5. Recommendations

The results obtained from this study lead to the following recommendations for future research:

- Sandstone reservoir rocks in the Dutch subsurface are quartz-rich. Therefore the method of SWIR spectroscopy disregards a large volumetric part of these samples. The integration Long-Wave Infrared Reflectance spectroscopy would possibly provide important information as minerals groups such as silica and feldspar have spectral responses within these wavelengths. Such research might provide better mineral abundancies while still producing a spatially continuous dataset.
- This study has not compared the hyperspectral data with other spatially continuous datasets such as wireline logs. Other research (Kraal et al. 2021) has made such comparisons; however, no examples have been found where it was performed on similar sedimentary basins like that of the West Netherlands Basin.
- The number of samples of which the physical properties were already examined with other analytical methods was relatively low for the amount of sample surface that was scanned. A similar methodology with samples in which the mineralogy and/or physical properties such as

porosity and permeability are known might provide more detailed insight into how these properties relate to the hyperspectral data. Hopefully, generating a dataset large enough from which quantifiable parameters can be established.

- The technique of SWIR spectroscopy would be of extra value when applicable on core cuttings, As it could eliminate the necessity of coring samples in a borehole. The study of Kraal et al. (2019) has already confirmed that using cuttings is suitable for spectroscopy. However, they stated a tendency for certain minerals to be lost in the process from the bottom of the borehole, to being washed clean of drilling mud, before finally being analysed. Further research is required to evaluate the effectiveness of this method when applied to sedimentary reservoir rocks that are rich in carbonates and clays.

6 Conclusion

Using SWIR spectroscopy has proven to be of added value for the identification and characterisation of physical properties of Triassic sandstones in the West Netherlands Basin. Acquisition of hyperspectral images using a SWIR camera and the wavelength mapping technique described by Van Ruitenbeek et al. (2014) combined with spectral algorithms allowed for: spatially continuous, consistent and quick identification of spectrally active minerals within the SWIR electromagnetic spectrum. This technique has successfully distinguished phyllosilicates, which other methods would not have been able to and detected compositional variation between equivalent minerals.

This research produced spatially continuous datasets of Naaldwijk-Geothermie (NLW-GT-01) and the Barendrecht Ziedewij (BRTZ-01) boreholes with neglectable amounts of sample preparation while being non-destructive. This data shows that the NLW-GT-01 core was extracted from a higher metamorphic intensity area and was subject to higher amounts of carbonate cementation than the BRTZ-01 core, both being mechanisms for porosity loss. The findings in this research are in accord with other studies that have examined the regional geology and/or these boreholes and explain the difference in porosity and permeability of both cores (e.g. De Hoo 2021; Maniar 2019; Ursem 2018; Koenen et al. 2013).

This method cannot detect non-hydroxylated mineral groups such as silica and feldspar, abundant in sandstone reservoirs in the Dutch subsurface. However, 1) the lack of sample preparation, 2) speed of analyses, 3) consistency, 4) spatial continuity, and 5) the obtainable mineralogical data make the acquisition of hyperspectral images within the SWIR of added value for the current standard of core logging.

With the current methodology and available datasets we will not yet be able to produce quantifiable parameters that would correctly correlate with physical parameters such as mineral abundance, porosity and permeability. Future work must produce a larger hyperspectral dataset that could directly be linked to known physical properties. Furthermore, it should explore the possibilities of combining multiple regions of the electromagnetic spectrum to enlarge the number of detectable minerals possibly and register their relative abundance more precisely. Exploratory research would benefit significantly from the recommendations as mentioned earlier and/or when this technique turns out to be effective on core cuttings. It would enable excessive data collection, lower exploration costs and eventually change the current standard of evaluating the subsurface.

Acknowledgements

I want to thank my supervisors Dr. André Niemeijer and Dr. Suzanne Hangx, for their supervision during this research project. Furthermore, I'm especially thankful for Jelte Stam, the discussions, guidance, and support have helped me tremendously. The unbelievable help and efforts from Frank van Ruitenbeek and Chris Hecker at ITC. And of course, the rest of the TNO staff for the atmosphere at the office and help with all my questions.

Bibliography

- Ames, R, and P P Farfan. 1996. "Formation in the P and Q Quadrants , Offshore the Netherlands." *Geology of Gas and Oil under the Netherlands*, 167–78.
- Anovitz, Lawrence M., and David R. Cole. 2015. "Characterization and Analysis of Porosity and Pore Structures." *Pore Scale Geochemical Processes* 80: 61–164.
<https://doi.org/10.2138/rmg.2015.80.04>.
- Bakker, W H. 2021. "HypPy (Hyperspectral Python)." 2021. <https://blog.utwente.nl/bakker/hyppy/>.
- Bakker, Wim. 2018. "Operating Instructions for SPECIM – Hyperspectral Cameras," no. September: 1–13.
- Bakker, Wim H. 2012. "HypPy User Manual." *ITC - University of Twente*.
<http://www.itc.nl/personal/bakker/hyppy.html>.
- Balen, R. T. Van, F. Van Bergen, C. De Leeuw, H. Pagnier, H. Simmelink, J. D. Van Wees, and J. M. Verweij. 2000. "Modelling the Hydrocarbon Generation and Migration in the West Netherlands Basin, the Netherlands." *Geologie En Mijnbouw/Netherlands Journal of Geosciences* 79 (1): 29–44. <https://doi.org/10.1017/S0016774600021557>.
- Bergen, Frank Van, Tim Tambach, Cor Hofstee, and Petra David. 2008. "Geochemical Consequences of CO2 Injection in the Barendrecht and Barendrecht-Ziedewij Gas Fields," 77.
- Bjørkum, Per Arne, Eric H. Oelkers, Paul H. Nadeau, Olav Walderhaug, and William M. Murphy. 1998. "Porosity Prediction in Quartzose Sandstones as a Function of Time, Temperature, Depth, Stylolite Frequency, and Hydrocarbon Saturation." *AAPG Bulletin* 82 (4): 637–47.
<https://doi.org/10.1306/1d9bc5cf-172d-11d7-8645000102c1865d>.
- Bjørlykke, Knut. 2015. *Petroleum Geoscience: From Sedimentary Environments to Rock Physics, Second Edition*. *Petroleum Geoscience: From Sedimentary Environments to Rock Physics, Second Edition*. Springer Berlin Heidelberg. <https://doi.org/10.1007/978-3-642-34132-8>.
- Bonté, D., J. D. Van Wees, and J. M. Verweij. 2012. "Subsurface Temperature of the Onshore Netherlands: New Temperature Dataset and Modelling." *Geologie En Mijnbouw/Netherlands Journal of Geosciences* 91 (4): 491–515. <https://doi.org/10.1017/S0016774600000354>.
- Bucher, Kurt, and Ingrid Stober. 2021. *Geothermal Energy From Theoretical Models to Exploration and Development Second Edition*. <https://www.springer.com/gp/book/9783662501931>.
- Calvin, Wendy M., and Elizabeth L. Pace. 2016. "Mapping Alteration in Geothermal Drill Core Using a Field Portable Spectroradiometer." *Geothermics* 61: 12–23.
<https://doi.org/10.1016/j.geothermics.2016.01.005>.
- Campbell, John. 2011. "Porosity." *Complete Casting Handbook V* (xiii): 391–464.
<https://doi.org/10.1016/b978-1-85617-809-9.10007-6>.

- Chang, Chandong, Mark D. Zoback, and Abbas Khaksar. 2006. "Empirical Relations between Rock Strength and Physical Properties in Sedimentary Rocks." *Journal of Petroleum Science and Engineering* 51 (3–4): 223–37. <https://doi.org/10.1016/j.petrol.2006.01.003>.
- Chuhan, Fawad A., Arild Kjeldstad, Knut Bjørlykke, and Kaare Høeg. 2003. "Experimental Compression of Loose Sands: Relevance to Porosity Reduction during Burial in Sedimentary Basins." *Canadian Geotechnical Journal* 40 (5): 995–1011. <https://doi.org/10.1139/t03-050>.
- Chukanov, Nikita V., and Alexandr D. Chervonnyi. 2016. *Infrared Spectroscopy of Minerals and Related Compounds*. <https://books.google.com/books?id=GOW9CwAAQBAJ&pgis=1>.
- Clark. 1999. "Chapter 1: Spectroscopy of Rocks and Minerals, and Principles of Spectroscopy." *Manual of Remote Sensing, Volume 3* 3: 3–58.
- Clark, R. N., and T. L. Roush. 1984. "Reflectance Spectroscopy: Quantitative Analysis Techniques for Remote Sensing Applications." *Journal of Geophysical Research* 89 (B7): 6329–40. <https://doi.org/10.1029/JB089iB07p06329>.
- Clauser, Christoph, and Ernst Huenges. 2013. "Rock Physics & Phase Relations: A Handbook of Physical Constants. Thermal Conductivity of Rocks and Minerals." *American Geophysical Union* 3 (Thermal Conductivity of Rocks and Minerals): 105–26.
- Cloutis, Edward A., Frank C. Hawthorne, Stanley A. Mertzman, Katherine Krenn, Michael A. Craig, Dionne Marcino, Michelle Methot, et al. 2006. "Detection and Discrimination of Sulfate Minerals Using Reflectance Spectroscopy." *Icarus* 184 (1): 121–57. <https://doi.org/10.1016/j.icarus.2006.04.003>.
- Deckers, Jef, and Eva van der Voet. 2018. "A Review on the Structural Styles of Deformation during Late Cretaceous and Paleocene Tectonic Phases in the Southern North Sea Area." *Journal of Geodynamics* 115 (September 2017): 1–9. <https://doi.org/10.1016/j.jog.2018.01.005>.
- Delbeke, Jos, Artur Runge-Metzger, Yvon Slingenberg, and Jake Werksman. 2019. "The Paris Agreement." *Towards a Climate-Neutral Europe: Curbing the Trend*, 24–45. <https://doi.org/10.4324/9789276082569-2>.
- Doublier, M P, A Roache, and S Potel. 2010. *Application of SWIR Spectroscopy in Very Low-Grade Metamorphic Environments: A Comparison with XRD Methods*. Vol. 2010.
- Duin, E. J.T., J. C. Doornenbal, Richard H.B. Rijkers, J. W. Verbeek, and Th E. Wong. 2006. "Subsurface Structure of the Netherlands - Results of Recent Onshore and Offshore Mapping." *Geologie En Mijnbouw/Netherlands Journal of Geosciences* 85 (4): 245–76. <https://doi.org/10.1017/s0016774600023064>.
- Edmund Optics. n.d. "Spectrum." Accessed February 12, 2022. <https://www.edmundoptics.fr/knowledge-center/application-notes/imaging/what-is-swir/>.
- Einhardt, J Jürgen R, Michael M. Raith, Peter Raase, and Jürgen Reinhard. 2012. *GUIDE TO THIN SECTION MICROSCOPY, Second Edition*. Book. [http://www.dmg-home.de/pdf/Guide-print quality.pdf](http://www.dmg-home.de/pdf/Guide-print%20quality.pdf).
- Fajrin. 2020. "3D Geomechanical Model," no. 4623118: 1–74.
- Felder, M, and S Fernandez. 2018. "Core Hot Shot NLW-GT-01," no. February.
- Garcia, Luz Adriana Guatame. 2013. "Crystallinity Variations of Smectite-Illite and Kaolin Hydrothermal Alteration Minerals by Using SWIR Spectroscopy. A Study of the Rodalquilar Au-Deposit, SE Spain." 60: 84.

- Geluk, M.C. 2005. *Trias Netherlands and Surrounding Areas*.
<https://dspace.library.uu.nl/handle/1874/1699>.
- “Geological Report TW OK II PanTerra Project G1363b.” 2021 15.
- Harris Corporation. 2018. “ENVI Analytics - Answers You Can Trust.” *Harris Geospatial Solutions, Inc.*, 1–8. <https://www.harrisgeospatial.com/SoftwareTechnology/ENVI.aspx>.
- Hoo, W. De. 2021. “A Geomechanical Assessment of the Influence of Intergranular Pressure Solution on Porosity Reduction in Triassic Sandstones in Naaldwijk, the Netherlands,” 1–59.
- Jaboyedoff, M., F. Bussy, B. Kübler, and Ph Thelin. 2001. “Illite ‘Crystallinity’ Revisited.” *Clays and Clay Minerals* 49 (2): 156–67. <https://doi.org/10.1346/CCMN.2001.0490205>.
- Joseph, FAGBOHUN BABATUNDE. 2015. “COMBINING DOMINANT SPECTRAL FEATURES IN AIRBORNE SWIR AND TIR IMAGERY FOR MINERALOGICAL MAPPING.”
- Koenen, M., Heege, J.H., Peeters, R. 2014. “CATO-2 Deliverable WP3.03-D23 Transport Properties of Intact Caprocks and Effects of CO₂-Water-Rock Interaction.”
- Koenen, Mariëlle, Laura J. Wasch, Marit E. Van Zalinge, and Susanne Nelskamp. 2013. “Werkendam, the Dutch Natural Analogue for CO₂ Storage Long-Term Mineral Reactions.” *Energy Procedia* 37: 3452–60. <https://doi.org/10.1016/j.egypro.2013.06.235>.
- Kokaly, Raymond F., Roger N. Clark, Gregg A. Swayze, K. Eric Livo, Todd M. Hoefen, Neil C. Pearson, Richard A. Wise, et al. 2017. “USGS Spectral Library Version 7.” *U.S. Geological Survey Data Series 1035*, 61.
<https://doi.org/10.3133/ds1035%0Ahttps://pubs.er.usgs.gov/publication/ds1035>.
- Kraal, K. O., and B. Ayling. 2019. “Hyperspectral Characterization of Fallon FORGE Well 21-31: New Data and Technology Applications.” *Proceedings, 44th Workshop on Geothermal Reservoir Engineering*, no. 2016: 1–15.
<https://pangea.stanford.edu/ERE/pdf/IGAstandard/SGW/2019/Kraal.pdf>.
- Kraal, Kurt O., Bridget F. Ayling, Kelly Blake, Logan Hackett, Tito Satria Putra Perdana, and Robert Stacey. 2021. “Linkages between Hydrothermal Alteration, Natural Fractures, and Permeability: Integration of Borehole Data for Reservoir Characterization at the Fallon FORGE EGS Site, Nevada, USA.” *Geothermics* 89: 101946. <https://doi.org/10.1016/j.geothermics.2020.101946>.
- Kramers, L., J. D. Van Wees, M. P.D. Pluymaekers, A. Kronimus, and T. Boxem. 2012. “Direct Heat Resource Assessment and Subsurface Information Systems for Geothermal Aquifers; The Dutch Perspective.” *Geologie En Mijnbouw/Netherlands Journal of Geosciences* 91 (4): 637–49.
<https://doi.org/10.1017/S0016774600000421>.
- Laukamp, Carsten. 2011. “Short Wave Infrared Functional Groups of Rock-Forming Minerals.” *CSIRO Report Number EP115222*, no. August: 20.
<https://publications.csiro.au/rpr/download?pid=csiro:EP115222&dsid=DS5>.
- Logger, Hyperspectral Core. n.d. “Hyperspectral Core Logger.”
- Maniar, Zeenat. 2019. “Reservoir Quality Analysis of the Triassic Sandstones in the Nederweert and Naaldwijk Areas. A Post-Mortem Study.”
- Martynenko, Semyon, Pekka Tuisku, and Kim A A Hein. 2017. “High-Resolution Infrared Hyperspectral Characterization of Alteration at the Sadiola Hill Gold Deposit , Mali , Western Africa,” no. June. <https://research.utwente.nl/en/publications/high-resolution-short-wave-infrared-hyperspectral-characterizatio>.

- Matev, P.S. 2011. "Comprehensive Reservoir Quality Assessment of Buntsandstein Sandstone Reservoirs in the West Netherlands Basin for Geothermal Applications in Zuid Holland Province Area," 296.
- Mathieu, Magali, Régis Roy, Patrick Launeau, Michel Cathelineau, and David Quirt. 2017. "Alteration Mapping on Drill Cores Using a HySpex SWIR-320m Hyperspectral Camera: Application to the Exploration of an Unconformity-Related Uranium Deposit (Saskatchewan, Canada)." *Journal of Geochemical Exploration* 172: 71–88. <https://doi.org/10.1016/j.gexplo.2016.09.008>.
- Meunier, Alain, and Bruce Velde. 2004. "The Geology of Illite." *Illite*, 63–143. https://doi.org/10.1007/978-3-662-07850-1_3.
- Mijnlieff, Harmen F. 2020. "Introduction to the Geothermal Play and Reservoir Geology of the Netherlands." *Geologie En Mijnbouw/Netherlands Journal of Geosciences* 99. <https://doi.org/10.1017/njg.2020.2>.
- Ministry of Economic Affairs and Climate Policy. 2020. "Pre-Publication Chapter 8 Natural Resources and Geothermal Energy in the Netherlands."
- Moeck, Inga S. 2014. "Catalog of Geothermal Play Types Based on Geologic Controls." *Renewable and Sustainable Energy Reviews* 37: 867–82. <https://doi.org/10.1016/j.rser.2014.05.032>.
- NAM BV. 2000. "CHEMISTRY LABORATORY REPORT BRTZ-01."
- Nicolaas, Bart, and Adrianus Ursem. 2018. "Relating Main Buntsandstein Paleo-Environments to Present-Day Porosities in the West Netherlands Basin An Integrated Study of Core , Wireline , and Seismic Data."
- "Nlog." 2021. 2021. <https://www.nlog.nl/en/boreholes>.
- Pontual, Sasha, Nick Merry, and Paul Gamson. 1997. "Spectral Analysis Guides for Mineral Exploration: Vol 1 - Spectral Interpretation Field Manual." *AusSpec International Pty*.
- Rodger, Andrew, Carsten Laukamp, Maarten Haest, and Thomas Cudahy. 2012. "A Simple Quadratic Method of Absorption Feature Wavelength Estimation in Continuum Removed Spectra." *Remote Sensing of Environment* 118 (July 2014): 273–83. <https://doi.org/10.1016/j.rse.2011.11.025>.
- Ruitenbeek, Frank J.A. Van, Wim H. Bakker, Harald M.A. Van Der Werff, Tanja E. Zegers, Jelmer H.P. Oosthoek, Zulfa A. Omer, Stuart H. Marsh, and Freek D. Van Der Meer. 2014. "Mapping the Wavelength Position of Deepest Absorption Features to Explore Mineral Diversity in Hyperspectral Images." *Planetary and Space Science* 101: 108–17. <https://doi.org/10.1016/j.pss.2014.06.009>.
- Ruitenbeek, Frank J.A. van, Pravesh Debba, Freek D. van der Meer, Thomas Cudahy, Mark van der Meijde, and Martin Hale. 2006. "Mapping White Micas and Their Absorption Wavelengths Using Hyperspectral Band Ratios." *Remote Sensing of Environment* 102 (3–4): 211–22. <https://doi.org/10.1016/j.rse.2006.02.012>.
- Ruitenbeek, Frank J.A. van, Jasper Goseling, Wim H. Bakker, and Kim A.A. Hein. 2020. "Shannon Entropy as an Indicator for Sorting Processes in Hydrothermal Systems." *Entropy* 22 (6): 1–13. <https://doi.org/10.3390/E22060656>.
- Savitri, Kartika P., Christoph Hecker, Freek D. van der Meer, and Ridwan P. Sidik. 2021. "VNIR-SWIR Infrared (Imaging) Spectroscopy for Geothermal Exploration: Current Status and Future Directions." *Geothermics* 96 (January): 102178. <https://doi.org/10.1016/j.geothermics.2021.102178>.

- Simpson, M P, and A B Christie. 2016. *Exploration of New Zealand Mineral Deposits and Geothermal Systems Using X-Ray Diffraction (XRD) and Reflectance Spectrometry (SWIR): A Comparison of Techniques*. *GNS Science*. <https://doi.org/10.21420/G2NP4D>.
- Simpson, Mark P., and Andrew J. Rae. 2018. "Short-Wave Infrared (SWIR) Reflectance Spectrometric Characterisation of Clays from Geothermal Systems of the Taupō Volcanic Zone, New Zealand." *Geothermics* 73 (October 2017): 74–90. <https://doi.org/10.1016/j.geothermics.2018.01.006>.
- Simpson, Mark P. 2015. "Reflectance Spectrometry [SWIR] of Alteration Minerals Surrounding the Favona Epithermal Vein. Waihi Vein System, Hauraki Goldfield." *AusIMM New Zealand Branch Annual Conference 2015*, no. August 2015: 490–99.
- Specim. 2014. "Sisurock." http://www.specim.fi/files/pdf/sisu/datasheets/SisuROCK_Datasheet-ver1-13.pdf.
- . 2015. *Faster Drill Core Scanning with Specim's SisuROCK Hyperspectral Core Logger*. <https://www.youtube.com/watch?v=t6y1QZKhWZM>.
- SPECIM. 2015. "SisuCHEMA: Spectral Camera," no. 4: 2.
- Stichting Platform Geothermie. 2018. "Master Plan Geothermal Energy in the Netherlands," no. May.
- TANIKAWA, WATARU, and TOSHIHIKO SHIMAMOTO. 2006. "Klinkenberg Effect for Gas Permeability and Its Comparison to Water Permeability for Porous Sedimentary Rocks." *Hydrology and Earth System Sciences Discussions* 3: 1–24. <https://doi.org/10.5194/hessd-3-1315-2006>.
- Taylor, Kennedy, and Hall. 1967. "Aragonite in Fossils." *Proceedings of the Royal Society of London. Series B. Biological Sciences* 168 (1013): 377–412. <https://doi.org/10.1098/rspb.1967.0071>.
- TNO-GDN. 2019. "Stratigrafische Nomenclator." *Dinoloket*. 2019. <https://www.dinoloket.nl/stratigrafische-nomenclator/via-diagram/groep-naar-ouderdom>.
- Tun, Myo Min, I Wayan Warmada, Agung Harijoko, Reza Al-Furqan, and Koichiro Watanabe. 2015. "Characteristics Of Hydrothermal Alteration In Cijulang Area, West Java, Indonesia." *Journal of Applied Geology* 7 (1). <https://doi.org/10.22146/jag.16917>.
- Willems, Cees J.L., Andrea Vondrak, Harmen F. Mijnlief, Marinus E. Donselaar, and Bart M.M. Van Kempen. 2020. "Geology of the Upper Jurassic to Lower Cretaceous Geothermal Aquifers in the West Netherlands Basin - An Overview." *Geologie En Mijnbouw/Netherlands Journal of Geosciences* 99: 1–13. <https://doi.org/10.1017/njg.2020.1>.
- Wong, T E, D A J Batjes, and J De Jager. 2007. *Geology of the Netherlands*.
- Yang, K., J. F. Huntington, J. B. Gemmill, and K. M. Scott. 2011. "Variations in Composition and Abundance of White Mica in the Hydrothermal Alteration System at Hellyer, Tasmania, as Revealed by Infrared Reflectance Spectroscopy." *Journal of Geochemical Exploration* 108 (2): 143–56. <https://doi.org/10.1016/j.gexplo.2011.01.001>.
- Yang, Kai, Jonathan F. Huntington, Patrick R.L. Browne, and Chi Ma. 2000. "An Infrared Spectral Reflectance Study of Hydrothermal Alteration Minerals from the Te Mihi Sector of the Wairakei Geothermal System, New Zealand." *Geothermics* 29 (3): 377–92. [https://doi.org/10.1016/S0375-6505\(00\)00004-3](https://doi.org/10.1016/S0375-6505(00)00004-3).
- Ziegler, P. A., M. E. Schumacher, P. Dèzes, J. D. van Wees, and S. Cloetingh. 2004. "Post-Variscan Evolution of the Lithosphere in the Rhine Graben Area: Constraints from Subsidence Modelling." *Geological Society Special Publication* 223 (May 2014): 289–317. <https://doi.org/10.1144/GSL.SP.2004.223.01.13>.

Appendix:

1 BRTZ-01 SAMPLE LIST:

Slab: BRTZ-01

Nr#	Box	Top (cm)	Bottom (cm)	Length (cm)	Special notes	Nr#	Box	Top (cm)	Bottom (cm)	Length (cm)	Special notes
1	50	274666	274756	90		25	74	276813	276903	90	
2	51	274756	274846	90		26	75	276903	276965	62	
3	52	274846	274936	90		27	76	276965	277025	60	
4	53	274936	275027	91		28	77	277200	277287	87	
5	54	275027	275118	91		29	78	277287	277377	90	
6	55	275118	275204	86		30	79	277377	277467	90	
7	56	275204	275283	79		32	81	277467	277558	91	initial numbering out of order
8	57	275283	275324	41		31	80	277558	277652	94	switched 80 and 81 for correct depth
9	58	275400	275489	89		33	82	277652	277742	90	
10	59	275489	275580	91		34	83	277742	277834	92	
11	60	275580	275669	89		35	84	277834	277922	88	
12	61	275669	275758	89		36	85	277922	277986	64	
13	62	275758	275849	91		37	86	277986	278076	90	
14	63	275849	275939	90		38	87	278076	278166	90	
15	64	275939	276031	92		39	88	278166	278254	88	
16	65	276031	276095	64		40	89	278254	278342	88	
17	66	276095	276185	90		41	90	278342	278432	90	
18	67	276185	276274	89		42	91	278432	278522	90	
19	68	276274	276364	90		43	92	278522	278611	89	
20	69	276364	276454	90		44	93	278611	278702	91	
21	70	276454	276544	90		45	94	278702	278792	90	
22	71	276544	276634	90		46	95	278792	278851	59	
23	72	276634	276724	90		47	96	278851	278902	51	
24	73	276724	276813	89							

1 NLW-GT-01 SAMPLE LIST

Slab: NLW-GT-01

Nr#	Box	Top (cm)	Bottom (cm)	Length (cm)	Special notes
1	1	425000	425057	57	
2	2	425057	425157	100	HS1
3	3	425157	425256	99	
4	4	425256	425355	99	
5	5	425355	425455	100	HS2
6	6	425455	425554	99	
7	7	425554	425654	100	
8	8	425654	425754	100	
9	9	425754	425854	100	HS3
10	10	425854	425953	99	
11	11	425953	426049	96	
12	11b	426049	426061	12	
13	12	426061	426158	97	
14	13	426158	426257	99	HS4
15	14	426257	426357	100	
16	15	426357	426457	100	
17	16	426457	426557	100	HS5
18	17	426557	426657	100	
19	18	426657	426673	16	HS11
20	19	426673	426775	102	HS6
21	20	426775	426875	100	
22	21	426875	426975	100	
23	22	426975	427075	100	HS7
24	23	427075	427175	100	
25	24	427175	427253	78	
26	24b	427253	427287	34	
27	25	427287	427387	100	
28	26	427387	427487	100	HS8
29	27	427487	427587	100	
30	28	427587	427687	100	HS9
31	29	427687	427787	100	
32	30	427787	427887	100	HS10
33	31	427887	427967	80	

Hotshots	Depth (cm)	Horizontal plugs	Depth (cm)2	Vertical plugs	Depth (cm)3
HS1	425126	HO_PLUG_1	425003	VE_PLUG_9	425809
HS2	425425	HO_PLUG_2	425101	VE_PLUG_10	425907
HS3	425825	HO_PLUG_3	425200	VE_PLUG_15	426408
HS4	426226	HO_PLUG_5	425401	VE_PLUG_16	426506
HS5	426525	HO_PLUG_6	425499	VE_PLUG_17	426606
HS6	426724	HO_PLUG_7	425599	VE_PLUG_19	426710
HS7	427023	HO_PLUG_8	425700	VE_PLUG_20	426806
HS8	427401	HO_PLUG_9	425800	VE_PLUG_21	426905
HS9	427625	HO_PLUG_10	425900	VE_PLUG_22	427008
HS10	427825	HO_PLUG_11	425999	VE_PLUG_23	427108
HS11	426662	HO_PLUG_12	426095	VE_PLUG_24	427207
		HO_PLUG_13	426199	VE_PLUG_25	427380
		HO_PLUG_16	426500	VE_PLUG_26	427462
		HO_PLUG_17	426600	VE_PLUG_27	427582
		HO_PLUG_19	426704	VE_PLUG_28	427682
		HO_PLUG_20	426800	VE_PLUG_29	427764
		HO_PLUG_21	426899	VE_PLUG_30	427844
		HO_PLUG_22	427000		
		HO_PLUG_23	427100		
		HO_PLUG_24	427200		
		HO_PLUG_25	427375		
		HO_PLUG_26	427479		
		HO_PLUG_27	427575		
		HO_PLUG_28	427675		
		HO_PLUG_29	427776		
		HO_PLUG_30	427835		

2 Subset Script

When provided with samples the script subsets the files by desired length. This is executed with the HypPy3 subset.py by translating pixel sizes to actual depth.

```
#!/bin/bash
#use following command when \r error --> for test.sh = run.file
#sed -i 's/\r//g' clip_shell.sh

#set path
PATH=$HOME/mnt/c/spectral/hyppy3:$PATH

#FILES SLAB ## ADDD ALL FROM EXCEL LIST
FILELIST_SLAB=()

#insert values for amount of pixels (row_size) how much this is
#in mm (row_size_mm) and the amount of rows you want (small 11/small 33)
row_size=125
row_size_mm=32
rows=33

#row_size=375
#row_size_mm=96
#rows=11

#create folders to place new subsets

OUTPUTA=/mnt/d/"SLAB"_"size"
mkdir "$OUTPUTA"

#define subset and samples
for file_slab in "${FILELIST_SLAB[@]}"
do
    #for original image --> subset by inserted values, and place in
    #folder by name of SLAB_ID,KIND,PARTION OF SLAB
    variable=/mnt/d/location/"$file_slab"_variable

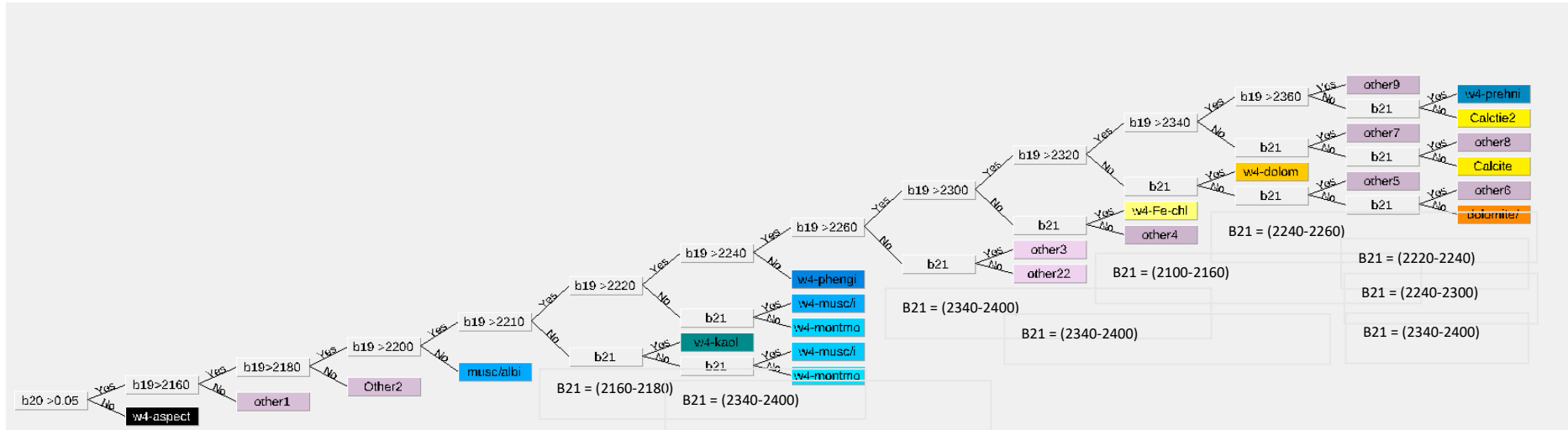
    for A_SUB in "$variable"
    do
        i=0
        while [ $i -le $rows ]
        do
            begin_y=$(( $i * $row_size ))
            partion="${file_slab:0:6}"
            partion_s=$(echo "$partion+($i*$row_size_mm)/10" | bc)
            i=$(( $i + 1 ))
            end_y=$(( $i * $row_size ))
            partion_e=$(echo "$partion+($i*$row_size_mm)/10" | bc)

            /mnt/c/spectral/hyppy3/subset.py -i "$A_SUB" -o "$OUTPUTA"/"$file_slab"_"
            "$partion_s"_"$partion_e"_"size"_"variable"_"clip" -y $begin_y -Y $end_y

        done
    done
done
echo "*****Complete*****"
```

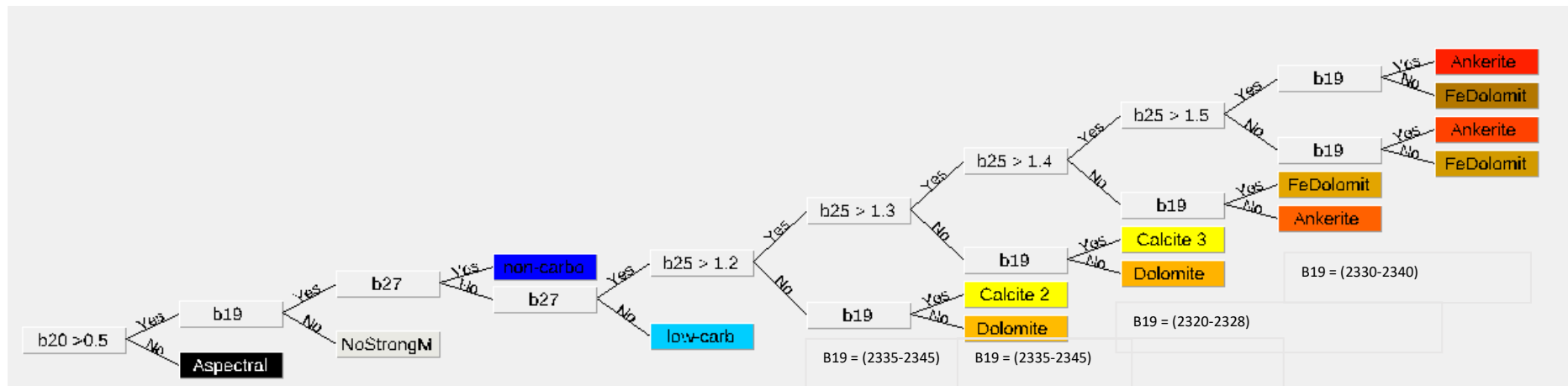
3 Decision trees

First Feature Tree



- B19: WL position deepest feature**
- B20: Depth deepest feature**
- B21: WL position 2nd deepest feature**

Carbonates Tree



B19: WL position deepest feature

B20: Depth deepest feature

B25: Ferrous drop

B27: Mixture ratio

4 Data overview

Porosity, permeability and output of the parameters as a function of depth for the two cores, NLW-GT-01 (top) and BRTZ-01 (bottom). Stratigraphy (St.) colours indicate; yellow = Solling Claystone, orange = Solling Sandstone, blue = Detfurth Sandstone, red = Volpriehausen Sandstone.

